

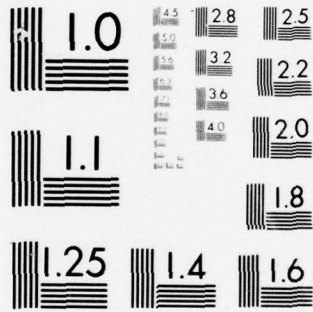
AD-A056 346

ILLINOIS UNIV AT URBANA-CHAMPAIGN COORDINATED SCIENCE LAB F/G 7/4  
DESORPTION AND SURFACE DIFFUSION: NITROGEN ON TUNGSTEN (110). (U)  
OCT 77 A J POLAK DAAB07-72-C-0259  
R-789 NL

UNCLASSIFIED

1 OF 2  
AD  
A056346





MICROCOPY RESOLUTION TEST CHART  
NATIONAL BUREAU OF STANDARDS-1963-A

**CSL COORDINATED SCIENCE LABORATORY**

**LEVEL II**

12  
SC

**DESORPTION AND  
SURFACE DIFFUSION:  
NITROGEN ON TUNGSTEN (110)**

ANTHONY JAMES POLAK

AD No. ....  
DDC FILE COPY

AD A 056346

DDC  
JUL 18 1978  
E

DISTRIBUTION STATEMENT A  
Approved for public release  
Distribution Unlimited

UNIVERSITY OF ILLINOIS - URBANA, ILLINOIS  
8 07 12 071

UNCLASSIFIED

SECURITY CLASSIFICATION OF THIS PAGE (When Data Entered)

REPORT DOCUMENTATION PAGE		READ INSTRUCTIONS BEFORE COMPLETING FORM
1. REPORT NUMBER	2. GOVT ACCESSION NO.	3. RECIPIENT'S CATALOG NUMBER
4. TITLE (and Subtitle) 6 DESORPTION AND SURFACE DIFFUSION: NITROGEN ON TUNGSTEN (110).		5. TYPE OF REPORT & PERIOD COVERED 7 Technical Report.
7. AUTHOR(s) 14 Anthony James/Polak		6. PERFORMING ORG. REPORT NUMBER 14 R-789, UILU-ENG-77-2236
9. PERFORMING ORGANIZATION NAME AND ADDRESS Coordinated Science Laboratory University of Illinois at Urbana-Champaign Urbana, Illinois 61801		8. CONTRACT OR GRANT NUMBER(s) 15 DMR-76-82088; DAAB-07-72-C-0259; NSF-DMR76-122
11. CONTROLLING OFFICE NAME AND ADDRESS Joint Services Electronics Program		10. PROGRAM ELEMENT, PROJECT, TASK AREA & WORK UNIT NUMBERS
14. MONITORING AGENCY NAME & ADDRESS (if different from Controlling Office)		12. REPORT DATE 11 Oct 1977
		13. NUMBER OF PAGES 161
		15. SECURITY CLASS. (of this report) UNCLASSIFIED 16 17/11
		15a. DECLASSIFICATION/DOWNGRADING SCHEDULE
16. DISTRIBUTION STATEMENT (of this Report) Approved for public release; distribution unlimited		
17. DISTRIBUTION STATEMENT (of the abstract entered in Block 20, if different from Report)		
18. SUPPLEMENTARY NOTES		
19. KEY WORDS (Continue on reverse side if necessary and identify by block number) Diffusion Tungsten Auger LEED Nitrogen		
20. ABSTRACT (Continue on reverse side if necessary and identify by block number) Scanning Auger spectroscopy has been used to monitor the migration of nitrogen atoms down a concentration gradient, on the (110) plane of tungsten. This concentration gradient is formed by the electron stimulated dissociation of molecular nitrogen, initially adsorbed at 95°K. These deposits are found to be thermally stable to several hundred K and unaffected by further electron irradiation. The adsorbed atoms form two different surface structures, depending upon the surface concentration. The desorption kinetics of both molecular and atomically bound nitrogen		

28 07 UNCLASSIFIED 097708 12 071

20. ABSTRACT (continued)

have been studied by a combination of Auger spectroscopy and flash desorption. The desorption of atomically bound nitrogen occurs as a second order process with an activation energy more than 7 times the activation energy of diffusion. Despite the large binding energy of the atomic nitrogen to the (110) surface, 153 kcal/mole, there is virtually no change in the work function upon adsorption. In addition the saturation coverage of the irradiated atomic nitrogen is found to be more than twice that of the nitrogen adsorbed at room temperature. Both are found to be in identical binding states.

ACCESSION for		
NBS	White Section	<input checked="" type="checkbox"/>
DOB	Buff Section	<input type="checkbox"/>
UNANNOUNCED		<input type="checkbox"/>
JUSTIFICATION.....		
BY.....		
DISTRIBUTION/AVAILABILITY CODES		
Dist.	AVAIL.	and/or SPECIAL
A		

UILU-ENG 77-2236

DESORPTION AND SURFACE DIFFUSION:  
NITROGEN ON TUNGSTEN (110)\*

by

Anthony J. Polak<sup>†</sup>

\*Carried out under NSF Grant DMR-76-82088 from the National Science Foundation.

<sup>†</sup>Supported in part by the Joint Services Electronics Program (U.S. Army, U.S. Navy and U.S. Air Force) under Contract DAAB-07-72-C-0259.

Reproduction in whole or in part is permitted for any purpose of the United States Government.

Approved for public release. Distribution unlimited.

DESORPTION AND SURFACE DIFFUSION : NITROGEN ON TUNGSTEN (110)

BY

ANTHONY JAMES POLAK

B.S., Stevens Institute of Technology, 1970  
M.S., University of Illinois, 1971

THESIS

Submitted in partial fulfillment of the requirements  
for the degree of Doctor of Philosophy in Metallurgical Engineering  
in the Graduate College of the  
University of Illinois at Urbana-Champaign, 1977

Thesis Adviser: Professor Gert Ehrlich

Urbana, Illinois

## ACKNOWLEDGMENT

I would like to express my appreciation to my advisor, Professor Gert Ehrlich, without whose guidance this investigation could not have been completed. I would also like to thank the technical staff of the Coordinated Science Laboratory for their help in the design and construction of the experimental system. Finally, I would like to thank Professor R. J. Maurer for the use of the facilities of the Materials Research Laboratory.

## TABLE OF CONTENTS

Chapter	Page
I. INTRODUCTION AND HISTORICAL REVIEW.....	1
II. EXPERIMENTAL EQUIPMENT.....	6
II.1. Apparatus.....	6
II.2. Sample Preparation.....	11
II.3. Dosing.....	19
III. FUNDAMENTALS AND TECHNIQUE.....	24
III.1. Auger Spectroscopy.....	24
III.2. Surface Characterization.....	37
III.2.A. Surface Structure.....	37
III.2.B. Surface Defects.....	41
III.2.C. Measurements of Work Function Change.....	48
IV. RESULTS.....	55
IV.1. Specimen Characteristics.....	55
IV.1.A. Contamination.....	55
IV.1.B. Surface Arrangement.....	55
IV.2. Ordinary Nitrogen Layers on W(110).....	57
IV.2.A. Adsorption and Desorption of $\gamma$ Nitrogen from the W(110).....	57
IV.2.B. Structure of the Gas Layer.....	68
IV.2.C. Desorption Kinetics of Nitrogen Adsorbed at Room Temperature.....	75
IV.3. Nitrogen Layers Produced by Electron Bombardment.....	80
IV.3.A. Electron Stimulated Dissociation.....	80
IV.3.B. Electron Stimulated Dissociation Cross Section.....	89
IV.3.C. Electron Stimulated Desorption.....	90
IV.3.D. Work Function Measurements of Electron Dissociated Nitrogen.....	92
IV.3.E. Thermal Desorption of Electron Dissociated Nitrogen.....	103

Chapter	Page
IV.4. Surface Diffusion Studies.....	104
IV.4.A. Measurement of Diffusion Profiles.....	109
IV.4.B. Diffusion.....	114
IV.4.C. Simultaneous Diffusion and Desorption.....	120
IV.5. Discussion.....	126
V. SUMMARY.....	128
APPENDIX A, Electron Bombardment Formation of Surface Devices.....	137
APPENDIX B, Computer Programs.....	142
APPENDIX C, Error Analysis.....	154
REFERENCES.....	158
VITA.....	162

DESORPTION AND SURFACE DIFFUSION:

NITROGEN ON TUNGSTEN (110)

Anthony J. Polak

Coordinated Science Laboratory and  
Department of Metallurgy and Mining Engineering  
University of Illinois at Urbana-Champaign, 1977

ABSTRACT

Scanning Auger spectroscopy has been used to monitor the migration of nitrogen atoms down a concentration gradient, on the (110) plane of tungsten. This concentration gradient is formed by the electron stimulated dissociation of molecular nitrogen, initially adsorbed at 95°K. These deposits are found to be thermally stable to several hundred K and unaffected by further electron irradiation. The adsorbed atoms form two different surface structures, depending upon the surface concentration.

The desorption kinetics of both molecular and atomically bound nitrogen have been studied by a combination of Auger spectroscopy and flash desorption. The desorption of atomically bound nitrogen occurs as a second order process with an activation energy more than 7 times the activation energy of diffusion. Despite the large binding energy of the atomic nitrogen to the (110) surface, 153 kcal/mole, there is virtually no change in the work function upon adsorption. In addition the saturation coverage of the irradiated atomic nitrogen is found to be more than twice that of the nitrogen adsorbed at room temperature. Both are found to be in identical binding states.

## I. INTRODUCTION AND HISTORICAL REVIEW

The stability of chemisorbed layers is of interest in understanding the chemical processes that occur on surfaces. Such technologically important reactions as catalysis, sintering, grain boundary segregation, and thin film formation depend critically on desorption and diffusion, the two mechanisms governing the stability of chemisorbed species. Not only is diffusion important in surface reactions, but it is also of considerable theoretical interest; the magnitude of the barrier to atomic motion provides important insights into the nature of the gas-metal bond. With this in mind, we have studied the diffusion and desorption of a gas chemisorbed onto a single crystal plane, specifically nitrogen on the (110) plane of tungsten.

Although the diffusion of metal atoms on single crystal planes has recently been opened up in investigations using the field ion microscope [1], relatively little is known about the diffusion of gases chemisorbed on metals. Gomer and coworkers [2,3], using field emission microscopy, studied the diffusion of a number of gases on the high index planes of a tungsten field emitter. They deposited the gas on one side of the field emitter and upon warming observed the spreading of the gas layer over the surface. From the rate at which the gas covered the surface an estimate of the diffusion coefficient was made. For oxygen on a tungsten field emitter the barrier to surface migration was found to be  $30 \pm 1.5$  kcal/mole; for hydrogen on tungsten this barrier was estimated at  $9.6 - 16 \pm 3$  kcal/mole. The activation energy of diffusion for hydrogen on tungsten amounts to approximately 20% of the binding energy, depending on the nature of the sites involved. Using the same technique, Ehrlich and Hudda [4] followed the migration of

nitrogen over the high index planes of a tungsten tip. From the spreading out of the nitrogen layer they estimated that the barrier to diffusion was  $\approx 20$  kcal/mole around the [111], and  $\approx 35$  kcal/mole for the sharply stepped region surrounding the [100].

Very little work has been done on single crystal planes, and only recently have quantitative studies become available. After our research was underway, Butz and Wagner [5] reported the observation of oxygen diffusing on a macroscopic surface. They used a masking technique to create a deposit of oxygen on the (110) plane of tungsten, and contact potential measurements to follow the migration of the gas on the surface. With this technique they found a concentration dependent diffusion coefficient which can be described by a constant activation energy of  $27 \pm 2$  kcal/mole in the coverage range 0.4 to 0.9 monolayer. Wells and King [6], on the other hand, using a molecular beam nozzle source to deposit oxygen on the (100) plane of tungsten and secondary electron emission to detect the oxygen on the surface, were unable to observe any diffusion of oxygen along the surface. These are the only studies that have dealt with the diffusion of gas atoms on macroscopic surfaces.

The overriding obstacles in the study of gas diffusion on macroscopic surfaces are 1) the development of a technique with sufficient spatial resolution and sensitivity to detect the variation in surface concentration that occurs as a gas diffuses along the surface, and 2) the actual creation of a surface concentration gradient.

These two problems can be overcome by the use of Auger spectroscopy, as was done by Jannsen [7]. Using electron stimulated desorption to create the localized deposits and Auger spectroscopy, he studied the diffusion of sodium on MgO, for which the barrier to surface diffusion was found to be  $< 1.2$  kcal/mole. We chose scanning Auger spectroscopy as the technique by which to study the variation in surface concentration of an adsorbed gas layer. Auger spectroscopy provides us with an extremely sensitive surface tool, with potentially excellent spatial resolution. The Auger electron gun can also be used to create the localized surface gas deposits.

It is well known that the characteristics of the gas adlayer will depend critically upon the exact gas and crystal orientation being studied. Therefore the use of a single crystal cut to expose only one plane is imperative. The choice of the crystal substrate is restricted to elements which have minimal surface impurities and surface defects, can be cleaned in an ultra high vacuum and are able to withstand the repeated bakeouts necessary to achieve an ultra high vacuum environment. The only materials that meet these requirements are the transition elements, which in general are easy to prepare, clean and observe in single crystal form.

Tungsten was chosen as the substrate material because of the extensive research which has been performed on it with a number of adsorbed gases [8-12]. Nitrogen was selected as adsorbate since it is the simplest diatomic gas that can be detected by Auger spectroscopy and because of its unusual behavior on the (110) plane of tungsten [13,14].

The behavior of nitrogen on the (110) of tungsten is quite different from that on the other planes. The most striking differences are in the rate of adsorption and the work function change that occur after nitrogen is adsorbed on the surface. Typically, the initial sticking coefficient for nitrogen on planes other than the (110) amounts to  $\approx .33$  at  $298^{\circ}\text{K}$ , rising to  $\approx .51$  at  $115^{\circ}\text{K}$  [8]. On the (110) plane, however, the sticking coefficient is only  $.004$  [13].

The variation in the work function of single crystal planes with different surface coverages has been studied by numerous techniques, on both microscopic and macroscopic samples. On the (110) plane of tungsten, Delchar and Ehrlich [14], employing the Kelvin contact potential method, were unable to detect any change in the work function after room temperature exposure to nitrogen. Only by increasing the pressure to  $10^{-2}$  Torr or lowering the temperature to  $190^{\circ}\text{K}$  did they observe a change, which amounted to  $-.13$  eV. From the pressure dependence of the work function at room temperature they deduced that the nitrogen was bound with  $< 9$  kcal/mole. Using field ion microscopy, Ehrlich and Hudda [4] were also unable to directly observe adsorption of nitrogen on the (110) plane. Even at high exposures, when changes were noticed on all the surrounding planes, adsorption of nitrogen on the (110) plane was not noted. Only after the emitter temperature was lowered below  $190^{\circ}\text{K}$  was nitrogen adsorbed on the (110) plane. This result, however, should be viewed with caution. The inability to observe nitrogen may have resulted from the desorption of nitrogen adatoms from the emitter by electron tunneling from the imaging gas.

In LEED studies by Stern [15] and by Dooley and Haas [16] no change of the clean tungsten (110) pattern was found after exposure to nitrogen. These results were interpreted to mean that nitrogen did not adsorb on the (110) plane of tungsten at room temperature.

The desorption behavior of nitrogen from the (110) plane of tungsten has been found to be similar to that from the other planes of tungsten. At temperatures less than  $120^{\circ}\text{K}$ , nitrogen is adsorbed as a molecule in the  $\gamma$  state. Nitrogen bound in this state desorbs with first order desorption kinetics at temperatures greater than  $150^{\circ}\text{K}$ . At higher adsorption temperatures, nitrogen is bound in an atomic state, referred to as the  $\beta$  state. From the (110) plane, the  $\beta$  state desorbs following second order desorption kinetics with an activation energy of  $\approx 79$  kcal/mole [13]. A complete review of the nitrogen-tungsten system is given by R. Liu [17].

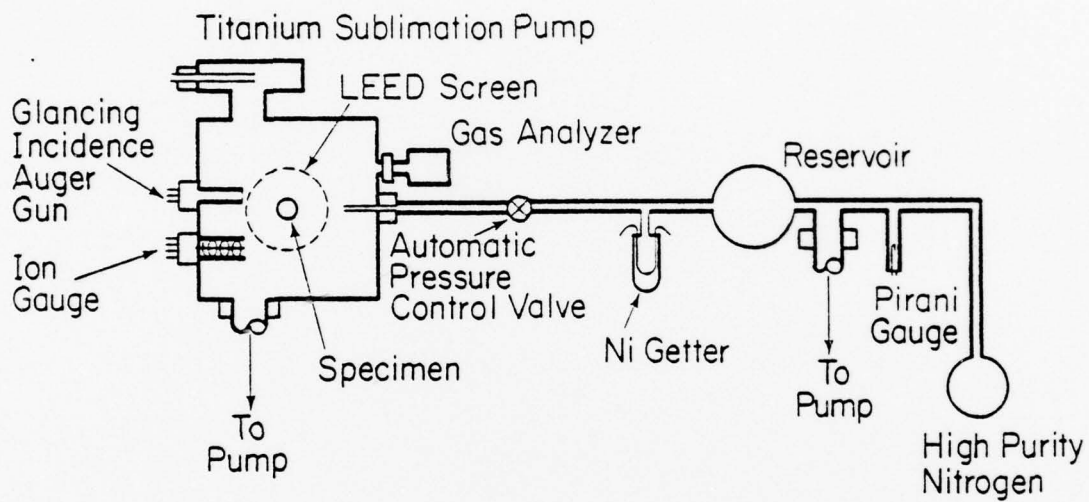
The desorption of nitrogen from the (110) is not very different from that on other planes. It is clear, however, that the adsorption behavior of nitrogen on the (110) differs significantly from that on the other planes of tungsten, occurring at a much slower rate. As will appear in subsequent chapters, our diffusion studies depend critically upon this fact.

## II. EXPERIMENTAL EQUIPMENT

### II.1. Apparatus

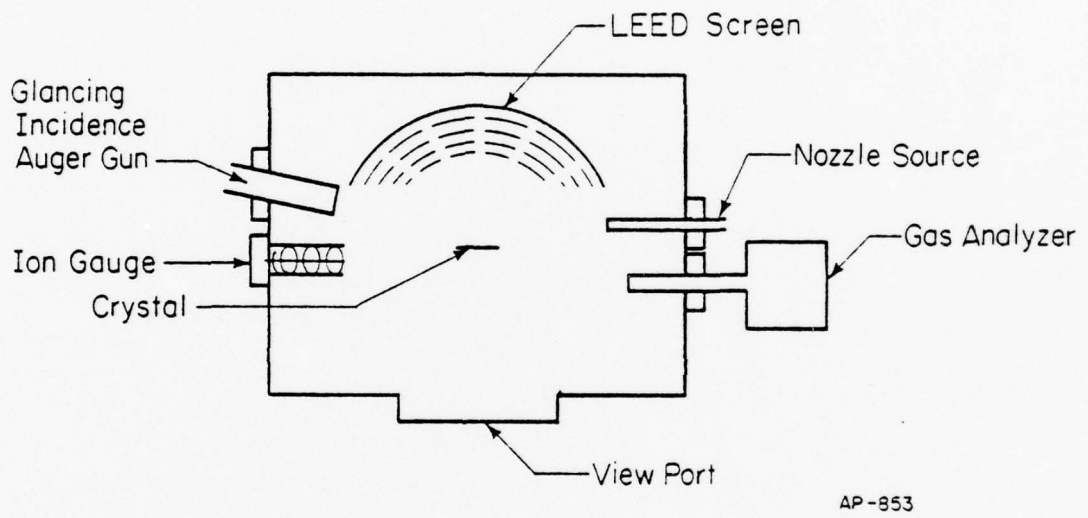
Prior to detailed studies of diffusion and desorption of nitrogen on the tungsten (110), it is necessary to characterize more closely the interaction of nitrogen with the (110) plane of tungsten. This characterization is accomplished by low energy electron diffraction (LEED), flash desorption, and measurements of work function changes.

The experimental apparatus, a block diagram of which is shown in Fig. 1, is basically an old fashioned Varian LEED vacuum system, model #981-0000. The vacuum system can be divided into two sections: the main chamber, shown in Fig. 2, in which all of the experiments are performed, and a separate gas handling system. A slight modification of the LEED electronics converts the standard LEED system into a retarding potential analyzer capable of performing Auger analysis. We also added a glancing incidence Auger electron gun, Varian model #981-2454. This gun has two sets of electrostatic deflection plates which make it possible to move the electron beam in both the x and y directions. Figure 3 shows a block diagram of the electronics associated with the glancing incidence Auger electron gun. The Varian Electron Gun Power module #981-2145 provides the proper potentials and current to the glancing incidence Auger electron gun. The Varian Scanning Sample Positioner, model #981-2157 supplies two sawtooth waveforms, which when applied to the x and y deflection plates, raster the electron beam across the crystal surface.



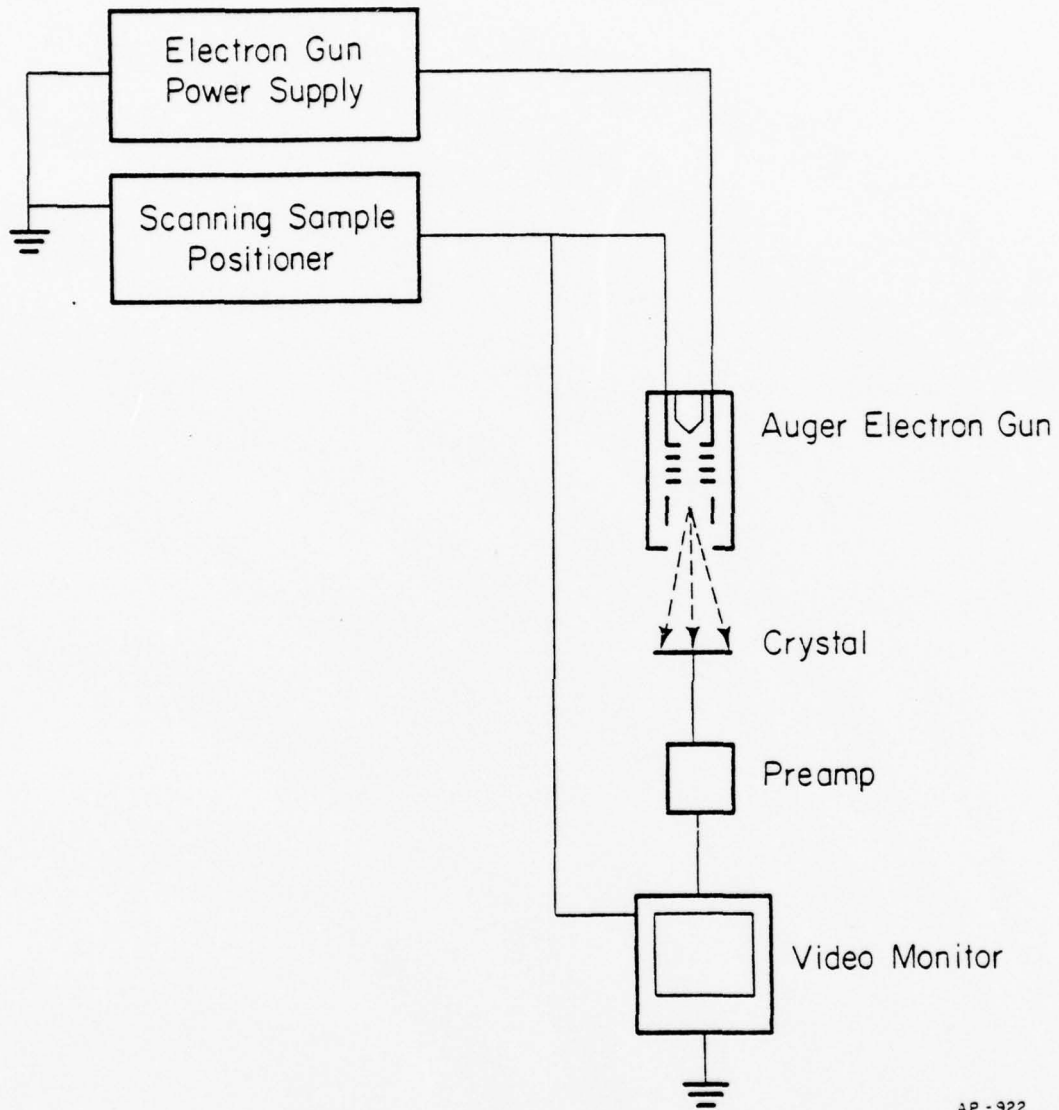
AP-317

Figure 1. Block diagram (side view) of the experimental apparatus for diffusion studies.



AP-853

Figure 2. Top view of the main chamber.



AP - 922

Figure 3. Electronics associated with the glancing incidence Auger gun. For a complete description, refer to the text.

The Scanning Sample Positioner also supplies a signal synchronized to the raster waveform, which controls the raster of the video monitor. This system is converted into a crude scanning electron microscope by using the current, which flows through the crystal to ground, to modulate the intensity of the video monitor.

The LEED measurements are performed with a standard Varian 4 grid LEED system, model #981-0024. Measurements of the work function change after nitrogen is deposited on the surface are also made using a modified form of the same LEED system. The desorption kinetics of nitrogen from the (110) plane are followed using an Electronics Associates Inc. residual gas analyzer, model Quad 250A.

Connected to the gas handling system are a gas bottle, oxygen leak, Pirani gauge, three nickel getters used to remove impurities from the gas supply, and two ion pumps. The manufacturer's (Air Reduction Co.) mass spectral analysis of the reagent grade nitrogen lists the major contaminants as:  $\text{CO} + \text{CO}_2 < .5$  ppm,  $\text{H} < 1.$  ppm, total hydrocarbons  $< .5$  ppm,  $\text{O}_2 < .3$  ppm, and argon 2.3 ppm. The threshold for other impurities is  $< 2$  ppm, the balance of the gas being nitrogen. Further purification of the nitrogen is achieved by selective gettering [4,18]. The getter tubes, shown in Fig. 1, are cooled to liquid nitrogen temperature after the nickel filaments and support loops have been thoroughly outgassed. A current of 2.3 to 2.5 amperes ac is passed through the .010" diameter nickel filaments; at this current the nickel loops glow with a red-orange color and a nickel film

slowly evaporates onto the getter wall. After a mirror-like nickel coat develops on the getter walls (approximately 1 hour), the current is turned off. The getters are then warmed to room temperature and all valves to the ion pumps and the automatic pressure control valve (APC) are closed.

Nitrogen gas is slowly admitted into the main section of the gas handling system until the pressure rises to  $5 \times 10^{-2}$  Torr, as measured by the Pirani gauge. The nitrogen is gettered in the gas handling system for a minimum of 45 minutes before being admitted into the main chamber.

The ultra high vacuum conditions necessary for reasonable surface studies are obtained using a 140 liter/sec ion pump, model #912-6006, on the main chamber. The main chamber is also equipped with a titanium sublimation pump (TSP). The background pressure in both the gas handling system and the main chamber before bakeout is typically in the mid  $10^{-8}$  Torr range. After a 1 to 2 day bakeout at  $300^{\circ}\text{C}$ , the pressure in both the main chamber and the gas handling system is generally in the  $10^{-10}$  to  $10^{-11}$  Torr range. A typical bakeout consists of heating the system to  $300^{\circ}\text{C}$  for 12 to 18 hours, cooling, outgassing of all filaments and getters, followed by 12 to 18 hours of additional bakeout.

## II.2. Sample Preparation

The sample is prepared from a zone refined single crystal rod, quarter inch in diameter, obtained from Material Research Corp. with the [100] along the axis. The crystal is orientated to within  $\pm \frac{1}{2}^{\circ}$  of the (110) plane using Laue back-reflection and then cut into a wafer .040" thick by electron

discharge machining. The sample is then mounted onto the central shaft of the polishing jig shown in Fig. 4, and once again aligned to  $\pm \frac{1}{2}^\circ$  of the (110) plane, by Laue back-reflection. Bee's wax is melted around the rim and back face of the crystal and the crystal mount is electrically connected to the positive terminal of a low voltage dc power supply. The crystal is electropolished in a 10% solution, by weight, of sodium hydroxide, using a dialysis membrane to separate the crystal from the steel cathode, as shown in Fig. 5. Not shown in Fig. 5 is the tray that the dialysis membrane and the steel plate are submerged in. The membrane is approximately one-quarter inch below the surface of the sodium hydroxide solution. A potential difference of 10 volts between the steel cathode and the crystal is provided by a Hyperion Hy-Si-20-6 power supply. To polish the crystal, the polishing jig is placed on the dialysis membrane, with the crystal lightly touching the membrane, and moved in a circular motion. The alignment of the crystal in the jig is periodically checked by Laue back-reflection and adjusted so that the (110) face is coplanar with the face of the polishing jig. After about .005" is removed from the face, the crystal is reversed and the back face is polished. The face being electropolished is continually cleaned with acetone to remove bits of wax which become embedded onto the surface. Both faces are repeatedly polished until the crystal is .015" thick. After the polishing is completed, the central portion of the crystal appears flat; however, it is very difficult to prevent preferential etching of the crystal edges and all the edges show some rounding.

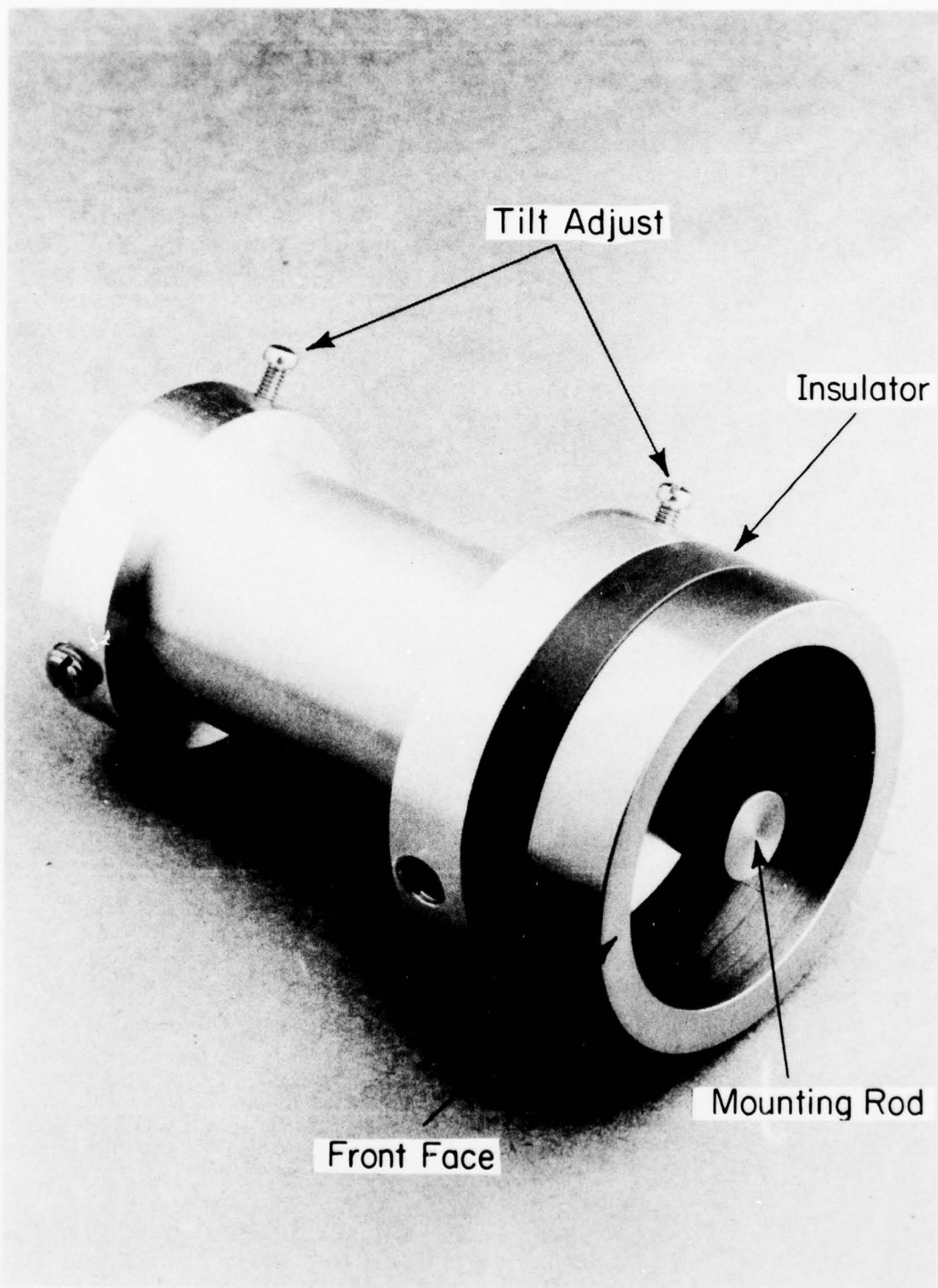
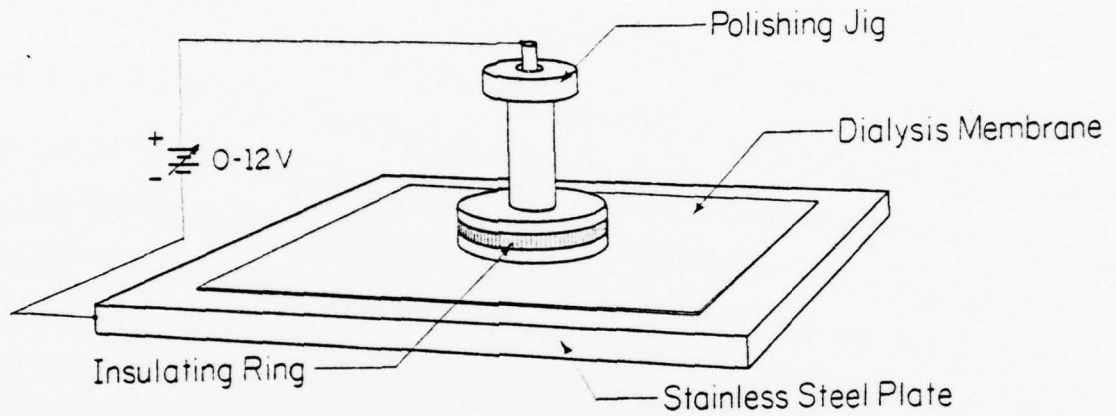


Figure 4. Overall view of the crystal polishing jig. The tilt screws are used to align the crystal once it is on the mounting rod. The electrical connection to the low voltage power supply is on the back of a mounting rod, not shown in this picture. The purpose of the insulating ring is to electrically isolate the front face from the mounting rod and prevent it from being electropolished while submerged in the NaOH solution.

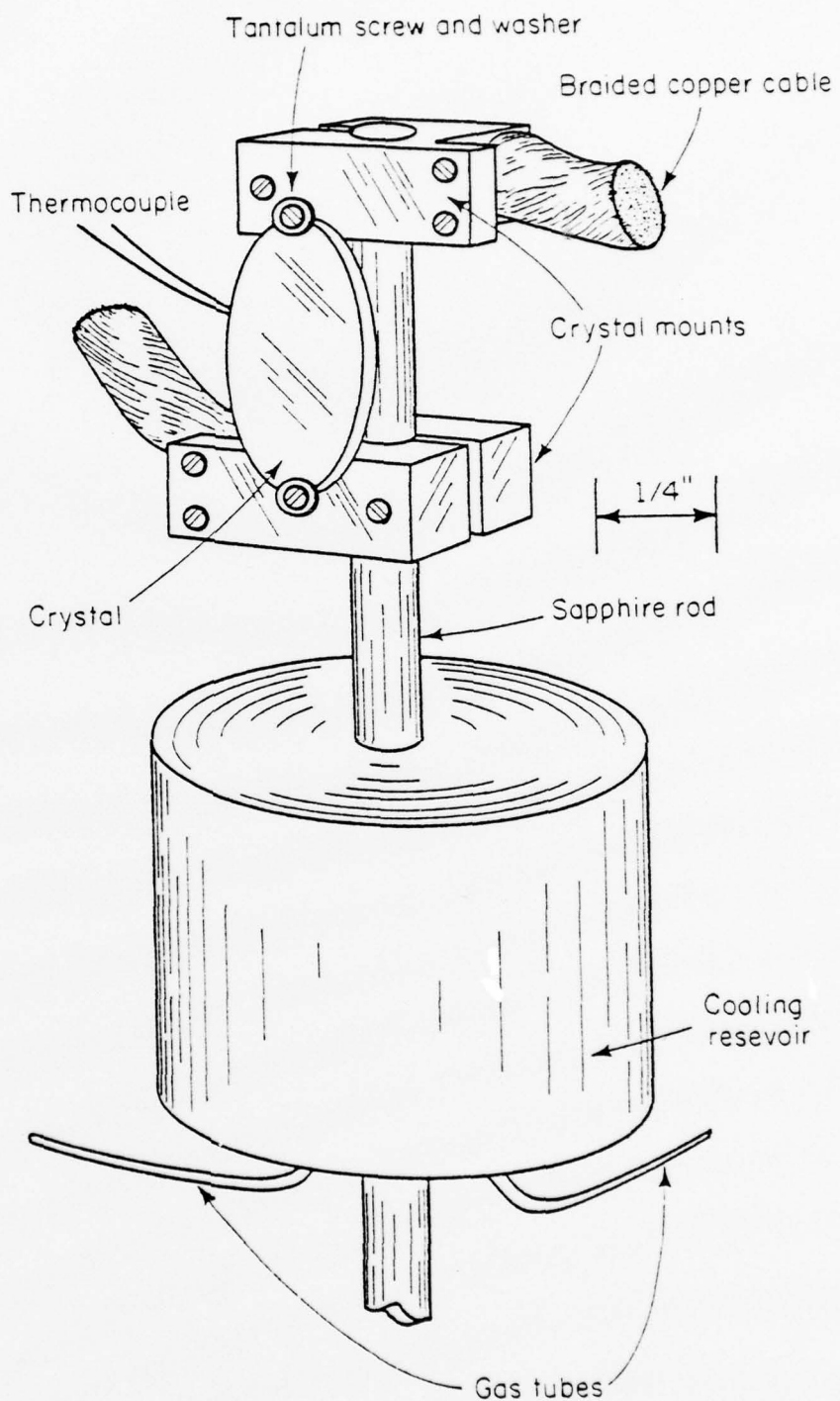


AP-852

Figure 5. Experimental arrangement for polishing the tungsten crystal.

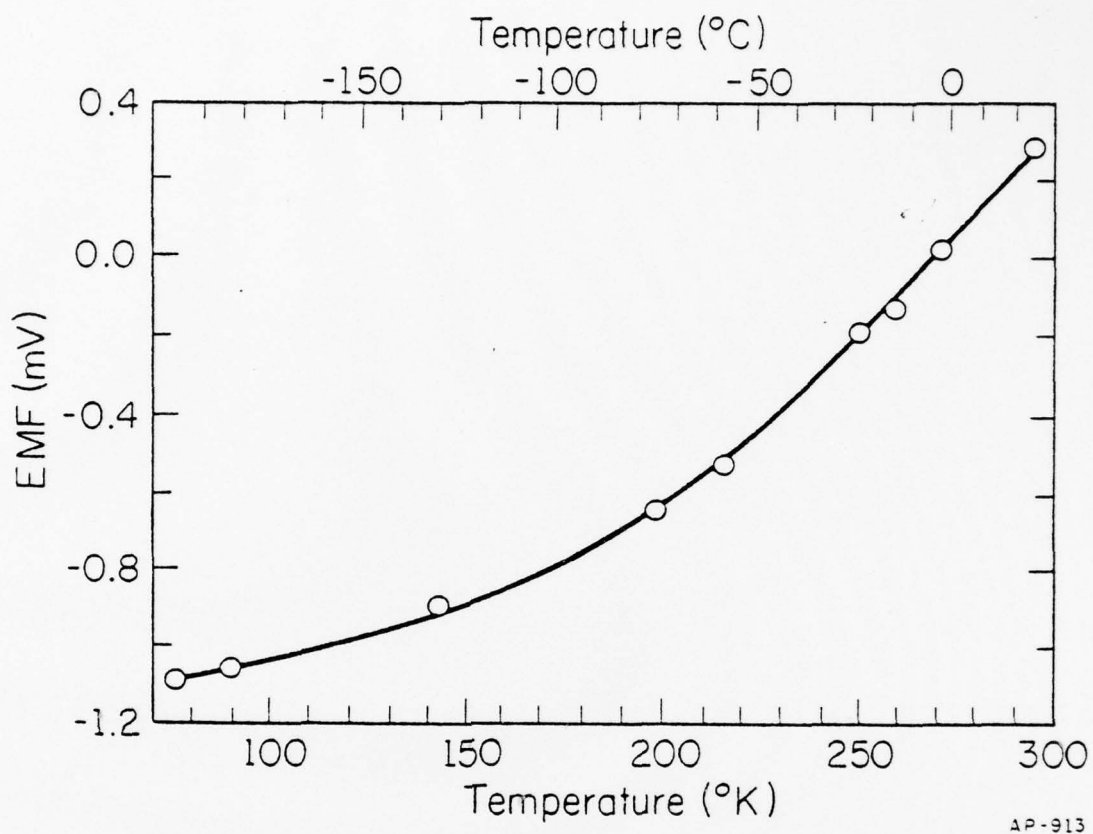
After the crystal is removed from the polishing jig it is thoroughly degreased in acetone and subsequently in ethanol, and then mounted on the holder shown in Fig. 6. This holder consists of a reservoir attached to a sapphire rod which serves as a thermal conduction medium to the crystal. By passing cooled nitrogen gas, under pressure, through the reservoir the temperature of the reservoir is reduced to  $82^{\circ}\text{K}$  and the crystal temperature to  $95^{\circ}\text{K}$ . Connected to the sapphire rod are two crystal mounts, made of tungsten. The crystal is held to these mounts by two sets of tantalum screws and washers. A tungsten 3% rhenium/tungsten 25% rhenium thermocouple, .005" in diameter, obtained from Omega Engineering Inc., is spotwelded to the edge of the crystal. This thermocouple has been calibrated against a copper-constantan thermocouple by Sandstrom and Withrow [19], so it may also be used as a low temperature measuring device. The low temperature calibration curve for the tungsten-rhenium thermocouple is shown in Fig. 7.

During the diffusion and desorption experiments it is necessary to maintain a high crystal temperature for extended periods of time. To accomplish this the thermocouple is used as the temperature sensor while the sample is resistively heated. By automatically controlling the power to the crystal we are able to maintain a crystal temperature constant to  $\pm 3 \text{ K}$ . A schematic of the temperature regulating circuit is shown in Fig. 8. Initially 300 amperes ac at 6 volts are needed to resistively heat the crystal to  $900^{\circ}\text{K}$ . Thereafter, only 60-80 amperes are necessary to maintain this temperature.



AP-859

Figure 6. Diagram of tungsten crystal mounted in the specimen holder.



AP-913

Figure 7. Low temperature calibration curve of the tungsten 3% rhenium/tungsten 25% rhenium thermocouple.

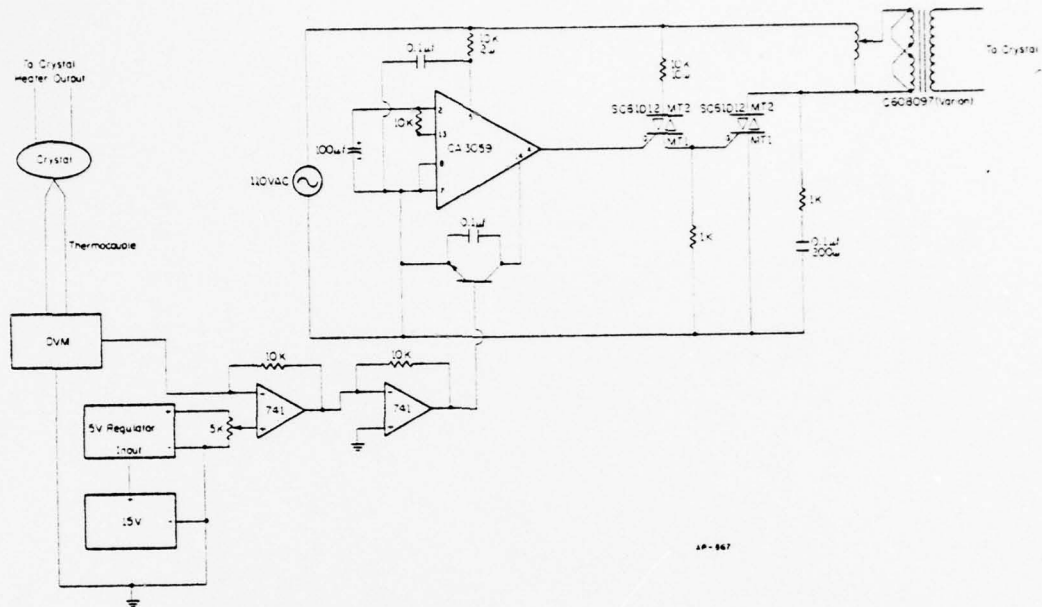


Figure 8. Schematic diagram of the crystal temperature control unit.

Initially the major contaminant on the surface, as shown by Auger spectroscopy, is carbon. After resistively heating the sample to  $2000^{\circ}\text{K}$  in  $10^{-6}$  Torr of oxygen, the carbon contamination is reduced. Figure 9 shows part of an Auger spectrum after 6 hours of this heat treatment. After 20 hours of cleaning, the only detectable contaminant is oxygen. The surface oxygen is easily removed by heating the sample to  $2800^{\circ}\text{K}$  for several minutes once the ambient gas is pumped out. An Auger spectrum of the clean (110) surface is shown in Fig. 10. No peaks other than those due to tungsten are detectable.

### II.3. Dosing

In order to study the interaction between gas and metal, a method of depositing a fixed amount of gas on the surface must be developed. We found that the best method of creating reproducible surface coverages is to expose the tungsten crystal to a fixed gas dose from a capillary, approximately 6 inches long and with a 3 mm inner diameter. Dosing is accomplished by maintaining a constant pressure of  $5 \times 10^{-2}$  Torr in the gas handling system and programming the APC valve to open to a predetermined position for a fixed period of time (33 seconds). This is accomplished by use of the timing circuit shown in Fig. 11. The crystal is exposed to doses of two different sizes, which we designate as either large or small. The time that the APC remains open is the same for both, but for a small dose the valve is not opened completely. An estimate of the number of gas molecules striking the surface for both a large and small dose is given in Section IV. Although the absolute value of the exposure is uncertain because of the possibility of direct collisions from the beam, we are able to expose the crystal to a reproducible amount of nitrogen and obtain reproducible surface coverages.

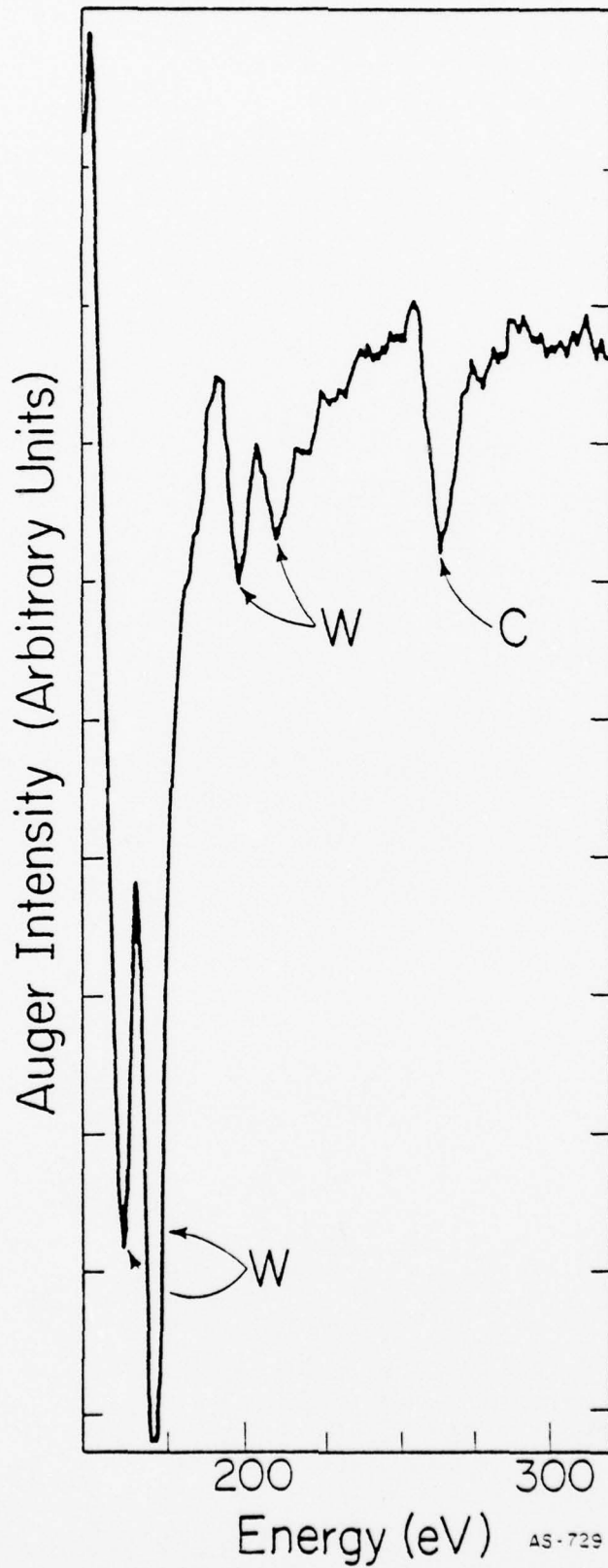


Figure 9. Auger spectrum of tungsten (110) crystal after 6 hours at  $2000^{\circ}\text{K}$  in  $10^{-6}$  Torr of oxygen.

AS-729

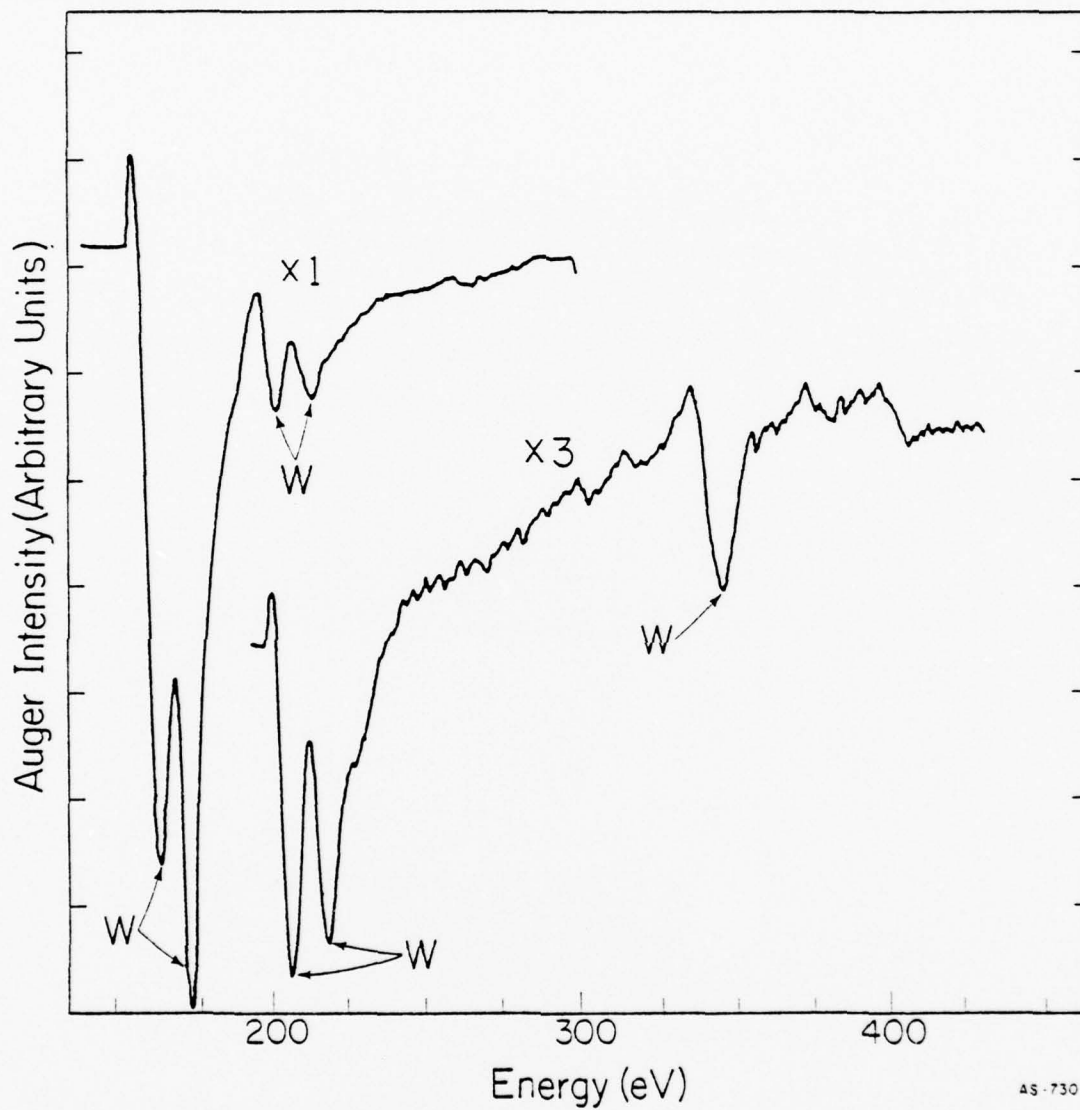
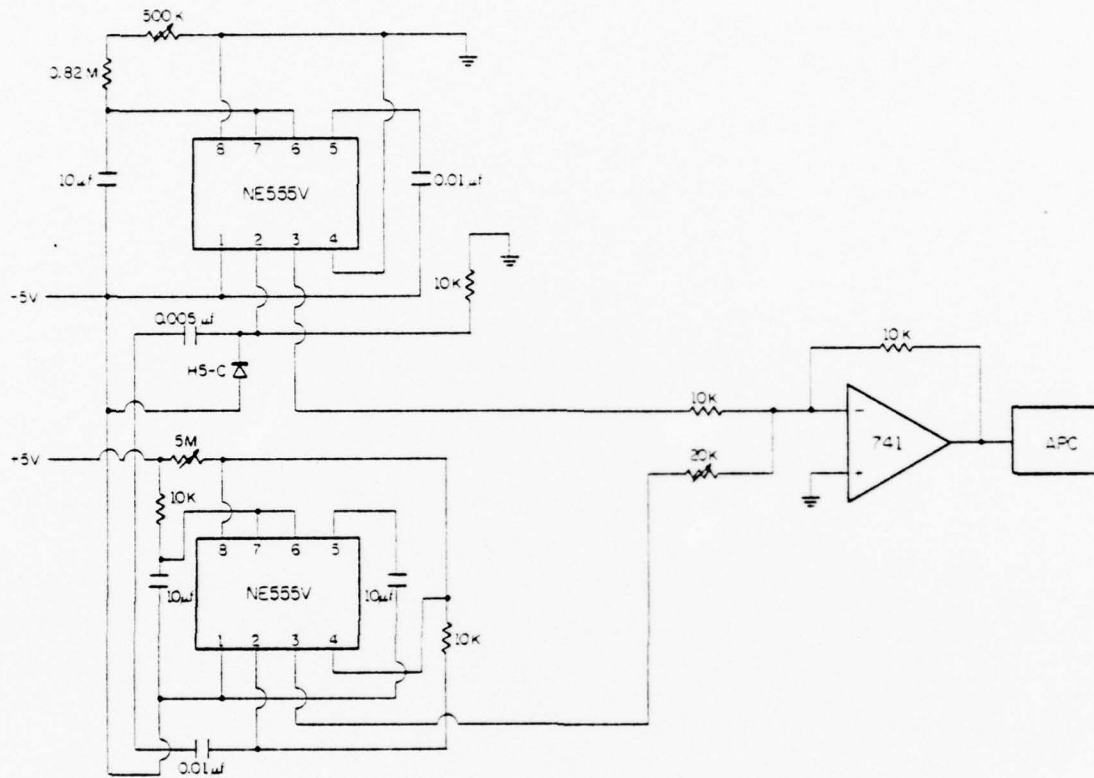


Figure 10. Auger spectrum of the tungsten (110) plane after 20 hours of cleaning in  $10^{-6}$  Torr of oxygen at  $2000^{\circ}\text{K}$ .



AP-965

Figure 11. Schematic diagram of the electronic circuit which is used to operate the automatic pressure control valve.

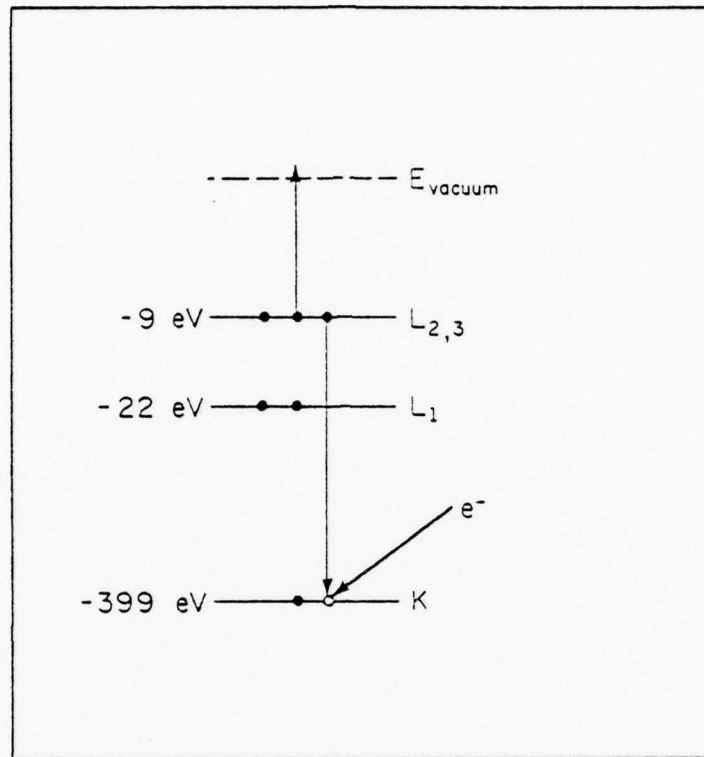
A typical exposure sequence is initiated with the cooling of the sample to a predetermined temperature. A clean film from the titanium-molybdenum filament source of the TSP is evaporated (the film is deposited for 30 seconds with a filament current of 45 amperes ac), followed immediately by heating the crystal to about  $2800^{\circ}\text{K}$  to remove any surface contamination. Once the sample is thoroughly cleaned, as described earlier, simple flashing is all that is necessary to remove the surface contamination that builds up overnight. The crystal is then cooled quickly, in less than 1 minute, to a predetermined temperature and rotated to face the nozzle source, which is shown in Fig. 2. The crystal is then exposed to a dose of nitrogen. During the exposure, all filaments are turned off so that dissociation of the molecular gas by a hot filament is not possible. After the exposure is complete, the TSP is once again turned on for 30 seconds to hasten the removal of the background gas. Taking an Auger spectrum of the crystal before and after the TSP is turned on, we are unable to detect any new Auger transitions. From this measurement we conclude that the TSP does not introduce any contaminants onto the crystal surface. During the exposure period the pressure in the main chamber increased by about a factor of 5, as determined with the ion gauge during a calibration run, and not during an actual experiment.

### III. FUNDAMENTALS AND TECHNIQUE

#### III.1. Auger Spectroscopy

To study the surface migration of nitrogen we use scanning Auger spectroscopy. This technique is ideally suited for the study of surfaces, as it is extremely sensitive, with the ability to detect less than .001 of a monolayer [20]. We define a monolayer as the number of atoms on the top layer of the tungsten (110) plane, which is  $1.4 \times 10^{15}$  atoms/cm<sup>2</sup>. Auger spectroscopy is sensitive to a region extending only a few atom layers into the crystal [21]. The limitation to the detected volume is not the penetration depth of the primary beam, but the escape depth of the Auger electrons, which in general is 10-20 Å [22]. This technique is therefore sensitive to changes occurring at the outer surface.

An Auger spectrum is most commonly obtained by the irradiation of a material with a beam of electrons having an energy of several thousand volts. The Auger process involves a series of electronic transitions whereby an atom, which has been excited by an incident electron, relaxes into its equilibrium state in such a way that it ejects an electron. The transitions involved in such a process are shown schematically in Fig. 12. The incident electron creates a hole in the K level; an electron from the L<sub>2,3</sub> level fills the vacancy. The amount of energy released in this process is  $E_K - E_{L_{2,3}}$ . This energy can appear either as a photon (X-ray) or be transferred to another electron. The latter is the Auger process and in the example shown in Fig. 12 another L<sub>2,3</sub> electron is ejected from the solid. For any Auger



AP-860

Figure 12. Schematic energy level diagram of the nitrogen Auger transition.

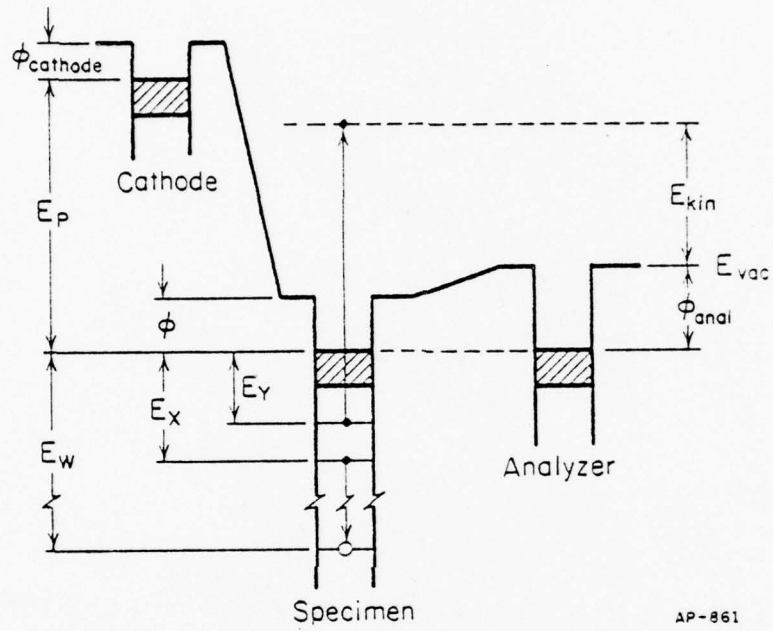
transition involving the energy levels WXY, a peak should appear at

$$E_{kin} = E_W - E_X - E_Y(z + \Delta) - \phi_{anal} \quad , \quad (1)$$

where  $E_{kin}$  is measured from the vacuum level of the analyzer,  $z$  is the atomic number,  $\Delta$  is a correction term which takes into account the change in the atomic charge after the initial hole is created, and  $\phi_{anal}$  is the work function of the analyzer [20], and not the work function of the crystal. This can readily be seen from Fig. 13. Since each element possesses its own "fingerprint" of Auger transitions, one should, in principle, be able to uniquely identify a surface atom. Of course, since hydrogen and helium each have less than three electrons they would not normally be expected to display Auger transitions.

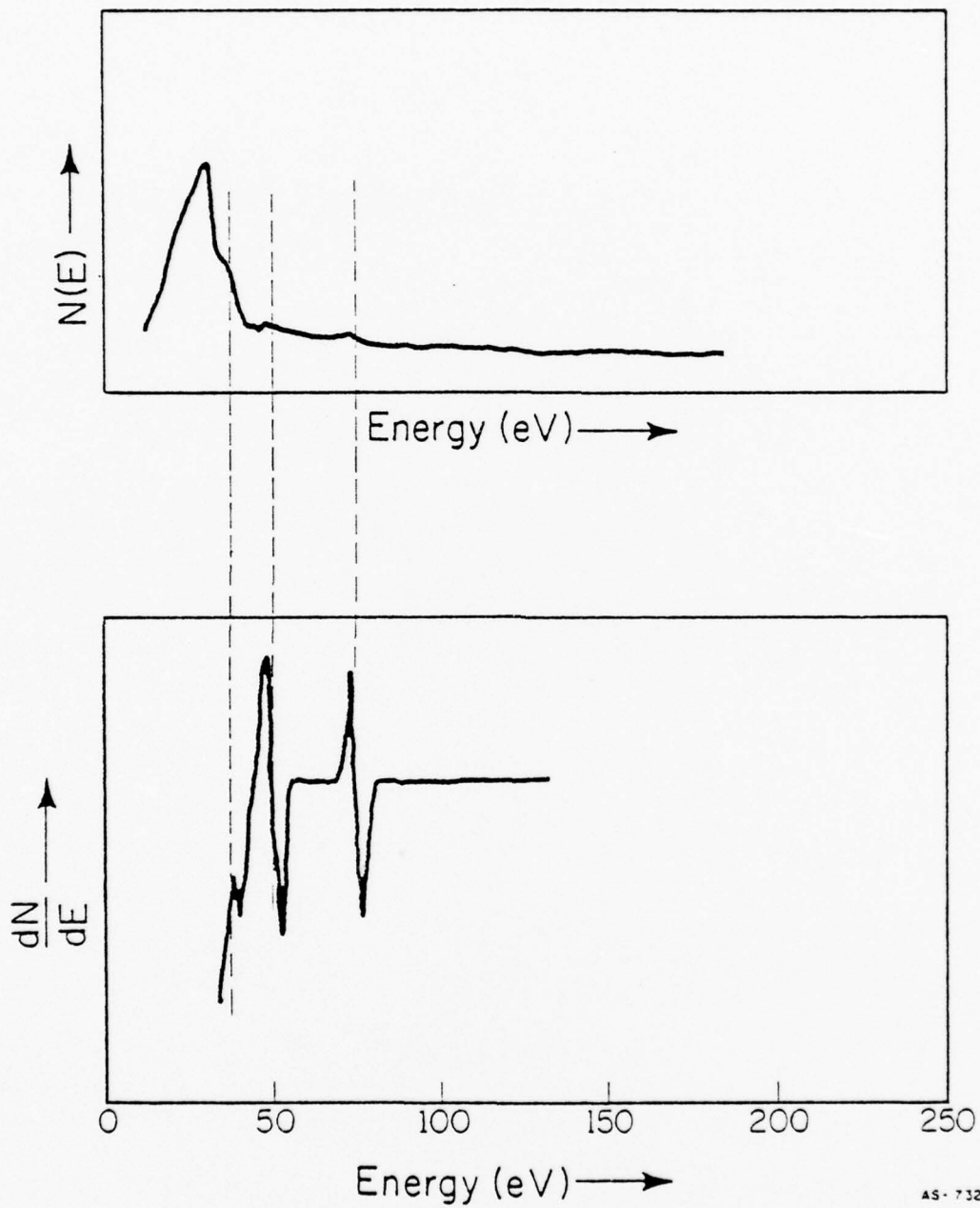
Figure 14a shows the secondary electron energy distribution as a function of emitted electron energy. Near 0 volts are the "true secondaries". Buried among the true secondaries and among secondaries at higher energies are the Auger electrons. The actual number of these is small, typically  $10^{-11}$  amperes for a primary current of 10  $\mu$ A. However, since these transitions occur at specific energies, there is a small but sudden change in the energy distribution curve.

In 1968 Harris [21,23] devised a method of electronically differentiating  $N(E)$ , the energy distribution of the secondary electrons emitted from the surface, and the practicality and sensitivity of Auger spectroscopy for surface analysis became obvious. When the energy distribution curve is differentiated, the smoothly varying background remains smooth but the differentiated Auger transitions suddenly predominate as illustrated in Fig. 14b. The point at which the first derivative of the energy distribution



AP-861

Figure 13. Energy level diagram of the complete Auger system.



AS-732

Figure 14. Energy distribution of secondary electrons emitted from a surface after electron irradiation, b) the first derivative of the secondary electron distribution in a).

curve has its minimum is by custom referred to as the Auger energy. The actual detection scheme is quite simple, and is shown in Fig. 15. Our energy analyzer is a standard LEED system which consists of a series of four concentric hemispherical grids with a collector. The first grid is grounded to provide a field free region between the sample, which is located at the center of curvature of the grids, and the retarding grids. The fourth grid is also grounded and forms a field free region between the collector and the inner two grids.

The retarding potential analyzer functions by repelling electrons with energy less than  $E$ , where  $-E/e$  is the voltage applied to the two inner grids. The grids act as a high pass filter and the collector current  $I(E)$  is therefore

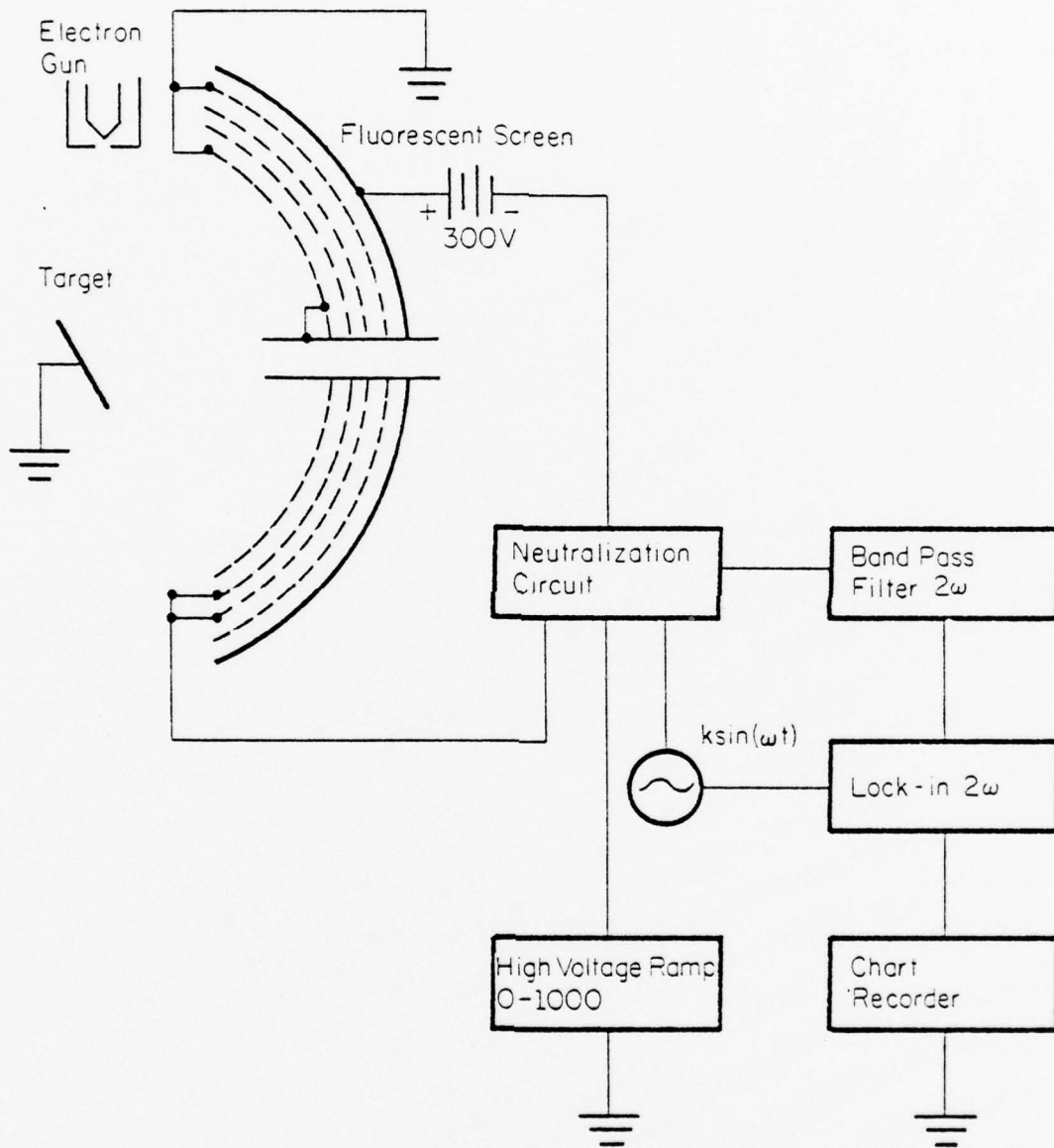
$$I(E) \propto \int_E^{\infty} N(E') dE' \quad , \quad (2)$$

with  $E'$  being a variable of integration. From Eq. (2) we see that

$$I'(E) \propto N(E) \quad , \quad (3)$$

where the ' denotes differentiation with respect to  $E$ . To obtain the derivative of the energy distribution curve,  $N'(E)$ , a small perturbing voltage  $\Delta E = k \sin(\omega t)$  is applied to the two inner grids. The collector current  $I(E)$  is thus energy modulated. Expanding  $I(E + \Delta E)$  in a Taylor series, we find

$$I(E + \Delta E) = I(E) + I'(E)\Delta E + \frac{I''(E)\Delta E^2}{2!} + \frac{I'''(E)\Delta E^3}{3!} + \dots \quad (4)$$



AS-727

Figure 15. Block diagram of the retarding potential analyzer.

upon substitution and rearrangement this becomes

$$I = I_0 + [I'k + \frac{I'''k^3}{8} + \dots] \sin(\omega t) - [\frac{I''k^2}{4} + \frac{I''''k^4}{48} + \dots] \cos(\omega t), \quad (5)$$

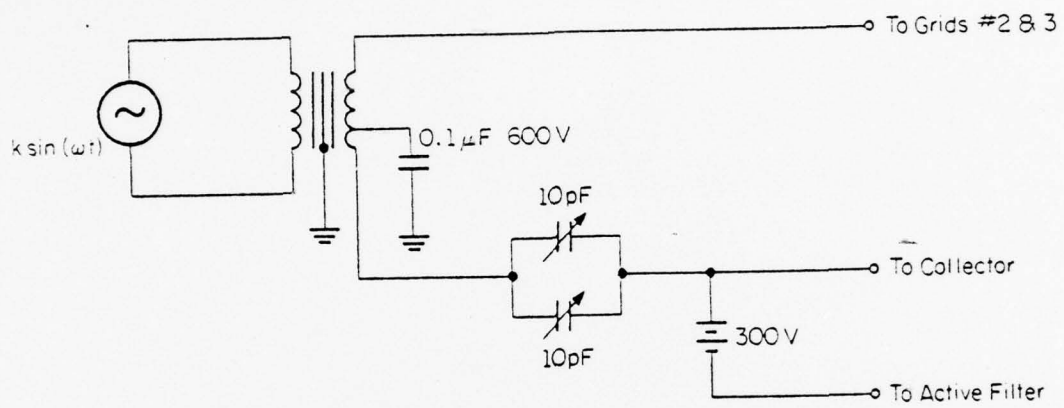
or

$$I = I(E_0) + I'k \sin(\omega t) - \frac{I''k^2}{4} \cos(2\omega t), \quad (6)$$

provided  $k^3$  and higher terms can be neglected.

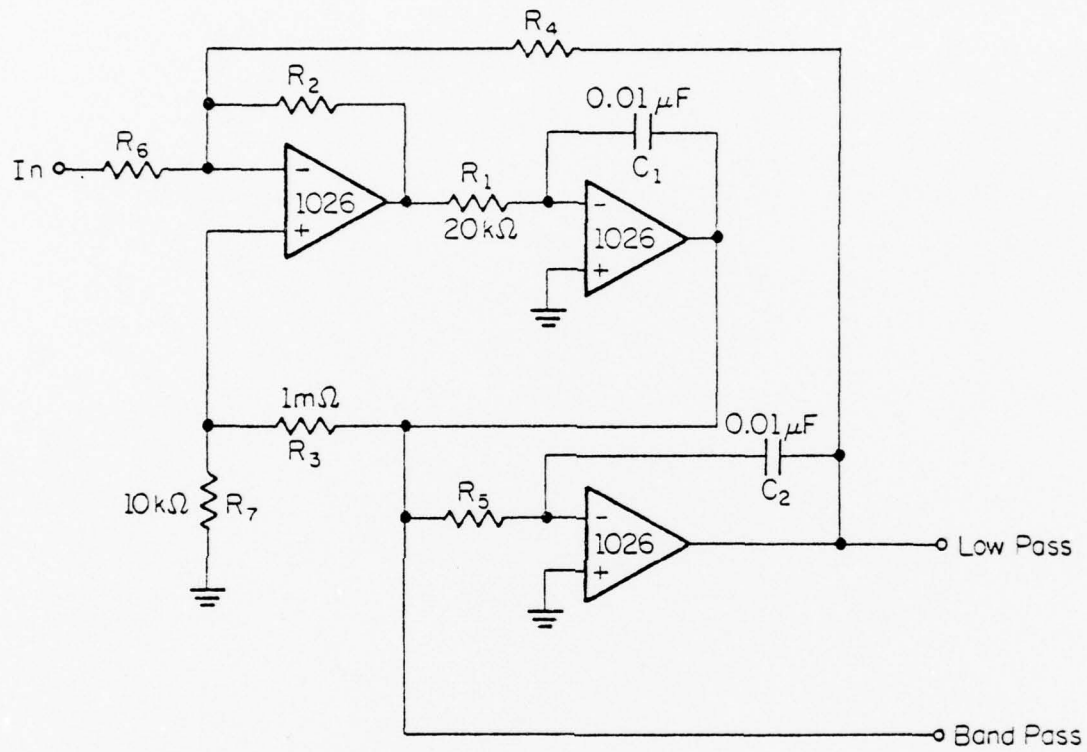
By using phase sensitive detection,  $N(E)$  can be obtained on tuning to the modulating frequency; detection at  $2\omega$  gives  $N'(E)$ , which is commonly referred to as the Auger spectrum. A complete review of Auger spectroscopy is given by C. C. Chang [20].

To electronically differentiate the energy distribution we modified a standard 4 grid LEED system, as shown in Fig. 15, for use as an energy analyzer. The purpose of the capacitance neutralization circuit (CNC) and the active filter, shown in Figs. 16 and 17, are to attenuate that part of the collector current whose frequency component is the same as the modulation frequency  $\omega$  and to permit only the second harmonic of the modulation frequency ( $2\omega = 4100$  Hz) to enter the lock-in. The CNC forms a capacitance bridge between the inner two grids and the collector on one hand, and the collector and ground on the other. By properly matching the capacitance of the CNC to the LEED system, the coupling to the collector is reduced, minimizing the collector current induced at the modulating frequency  $\omega$ . This prevents the Ithaco 391 A lock-in, used in our experiments, from overloading on the fundamental of the perturbation frequency and permits us to examine that part of the collector current that goes as  $2\omega$ . The active filter not only attenuates the fundamental but also reduces the bandwidth and increases the gain of the system to give an order of magnitude improvement in the signal-to-noise ratio.



AP-831

Figure 16. Schematic of the capacitance neutralization circuit.



$$f_0 = \frac{1}{2\pi\sqrt{R_1 C_1 R_5 C_2}}$$

$$Q = \frac{1}{3} \left[ 1 + \frac{R_3}{R_7} \right]$$

$$R_2 = R_4 = R_5 = R_6$$

AP-932

Figure 17. Schematic of the active filter.

Of the three major sources of noise [24], flicker noise, thermal noise, and shot noise, shot noise is the largest that cannot be reduced. The shot noise,  $I_n$ , in thermionic circuits is given by [25]

$$I_n^2 = 2eI_0B \quad , \quad (7)$$

where  $e$  is the electronic charge,  $I_0$  the total collector current and  $B$  the bandwidth. Under typical operating conditions, with  $I_0 = 100 \mu\text{A}$ ,  $B = .04$  (for a time constant of 3 sec and a 12 dB/octave rolloff), the rms noise voltage is  $\approx 1 \mu\text{V}$ . From a clean surface the signal voltage  $S$  can be larger than  $1000 \mu\text{V}$  [22-24] so that the signal-to-noise ratio is  $S/N = 1000$ . The Auger signal can originate several atom layers beneath the surface, this means that the signal is caused by  $\approx 5 \times 10^{15}$  atoms/cm<sup>2</sup>. If the limit of detection is defined as  $S/N = 1$ , then as little as  $5 \times 10^{12}$  atoms/cm<sup>2</sup> can be detected. The only way to increase the sensitivity is to increase  $I_0$  or to decrease  $B$ . Since the signal is proportional to  $I_0$  and the noise is proportional to  $\sqrt{I_0}$ , by increasing  $I_0$  the  $S/N$  ratio increases. The  $S/N$  ratio can also be increased by increasing the collection efficiency. Decreasing  $B$  will also improve the  $S/N$  by decreasing the noise current  $I_n$ ; however, this is unattractive since it will require an increase in the already long time constant.

In some cases Auger spectroscopy can be used to obtain quantitative information as to the surface concentration of a particular element, relative to a standard concentration. That this is the case can be seen by examining the energy distribution,  $N(E)$ , for an Auger transition. The energy distribution of most Auger transitions can be described by a

Gaussian or Lorentzian curve. If, for example, we take the energy distribution to be a Gaussian, as in Fig. 18a, then  $I'(E)$  is of the form

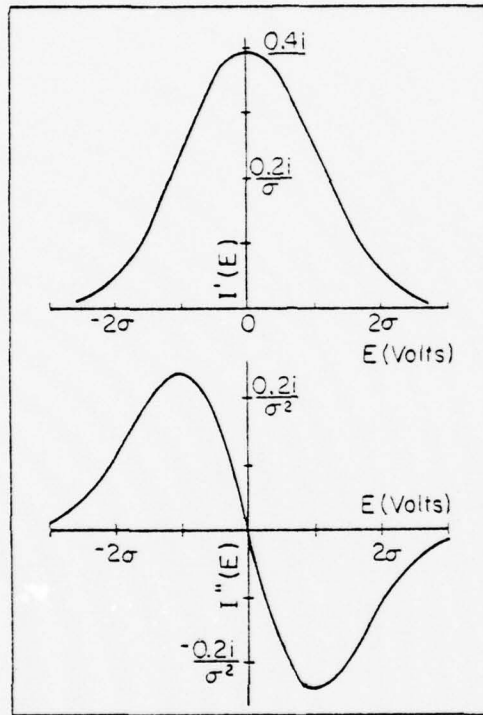
$$I'(E) = i \left( \frac{1}{\sigma\sqrt{2\pi}} \right) \exp \left[ - \frac{E^2}{2\sigma^2} \right], \quad (8)$$

where  $2\sigma$  is the full width at half height of the curve in Fig. 18a. The peak amplitude  $A_2$  of the Auger spectrum is given by [24]

$$A_2 = \pm .06 \left( \frac{k}{\sigma} \right)^2 i, \quad (9)$$

where  $k$  is the amplitude of the perturbation,  $i$  is the total Auger current of a single transition and  $\sigma$  corresponds to the inflection point of the  $N(E)$  curve. In this case the Auger peak-to-peak height is proportional to the Auger current  $i$ . Two points must be kept in mind before the differentiated peak-to-peak height can be used as a measure of the surface concentration:

- 1.) The differentiated peak must be symmetric, as it is for a Gaussian, Lorentzian or other reasonable Auger electron energy distribution; this can be seen in Fig. 18b.
- 2.) The Auger peak width must remain constant, independent of the surface coverage. An increase in the surface concentration will increase  $i$  and not  $\sigma$ . Using Eq. (8) we see that the peaks on the Auger spectrum will always appear at  $\pm \sigma$ , independent of the value of  $i$ . If these two conditions are not met then the peak-to-peak height of an Auger transition will not be indicative of the relative surface coverage. Fortunately these conditions are approximately satisfied by most elements.



AP-362

Figure 18. a) Gaussian representation of the electrons emitted in an Auger transition  $I'(E)$  (Auger current vs. (volts), b) the first derivative of (a).

## III.2. Surface Characterization

### III.2.A. Surface Structure

There is no technique available for accurately determining the perfection of a surface. Gross atomic misarrangements can be detected by electron microscopy; however, surface defects smaller than  $\approx 500 \text{ \AA}$  cannot easily be detected. LEED, on the other hand, can provide information only about surface structures which are periodic within a region over which the primary wave is coherent. The coherence length is limited by: (a) spatial coherence, which is dictated by the angular divergence of the primary beam, and (b) temporal incoherence which results from the energy spread of the primary beam. The coherence length  $L_s$  is related to the angular divergence  $\beta_s$  and the energy spread  $\Delta E$  of the primary beam by [26]

$$L_s = \frac{\lambda}{2(1 + \frac{\Delta E}{E})\beta_s}, \quad (10)$$

where  $\lambda$  is the electron wavelength and  $E$  is the normal electron energy. This gives a coherence length,  $L_s$ , of about  $10^2$  to  $10^3 \text{ \AA}$ , for a primary beam energy of 100 volts.

In order to understand the nature of a surface layer it is necessary to characterize the degree of perfection of the surface as well as the structure of the adsorbed layer. The periodicity of an adsorbed layer can be characterized by the use of low energy electron diffraction, LEED.

To derive the interference function we describe the scattered amplitude for a 2-dimensional array of scatters by

$$\psi = \psi_0 \sum_{n,m} f_{n,m} \exp(i\Delta\vec{K} \cdot \vec{r}_{n,m}), \quad (11)$$

where  $\Delta\vec{K} = \vec{K}_f - \vec{K}_i$ ,  $\vec{K}_f$  being the scattered wave vector,  $\vec{K}_i$  the incident wave vector,  $f_{n,m}$  the atomic scattering factor, and  $\vec{r}_{n,m}$  the position vector of the atom located at  $na\hat{x} + mb\hat{y}$  ( $n$  and  $m$  being integers), with  $a$  and  $b$  the lattice constants as shown in Fig. 19. The scattered wave vector  $\vec{K}_f$  can be written as [27]

$$\vec{K}_f = \frac{2\pi}{\lambda} (\cos \alpha)\hat{x} + \frac{2\pi}{\lambda} (\cos \beta)\hat{y} + \frac{2\pi}{\lambda} (\cos \gamma)\hat{z}, \quad (12)$$

where  $\alpha$ ,  $\beta$  and  $\gamma$  are the angles formed by  $\vec{K}_f$  and the  $x$ ,  $y$  and  $z$  axis respectively. For normal incidence,

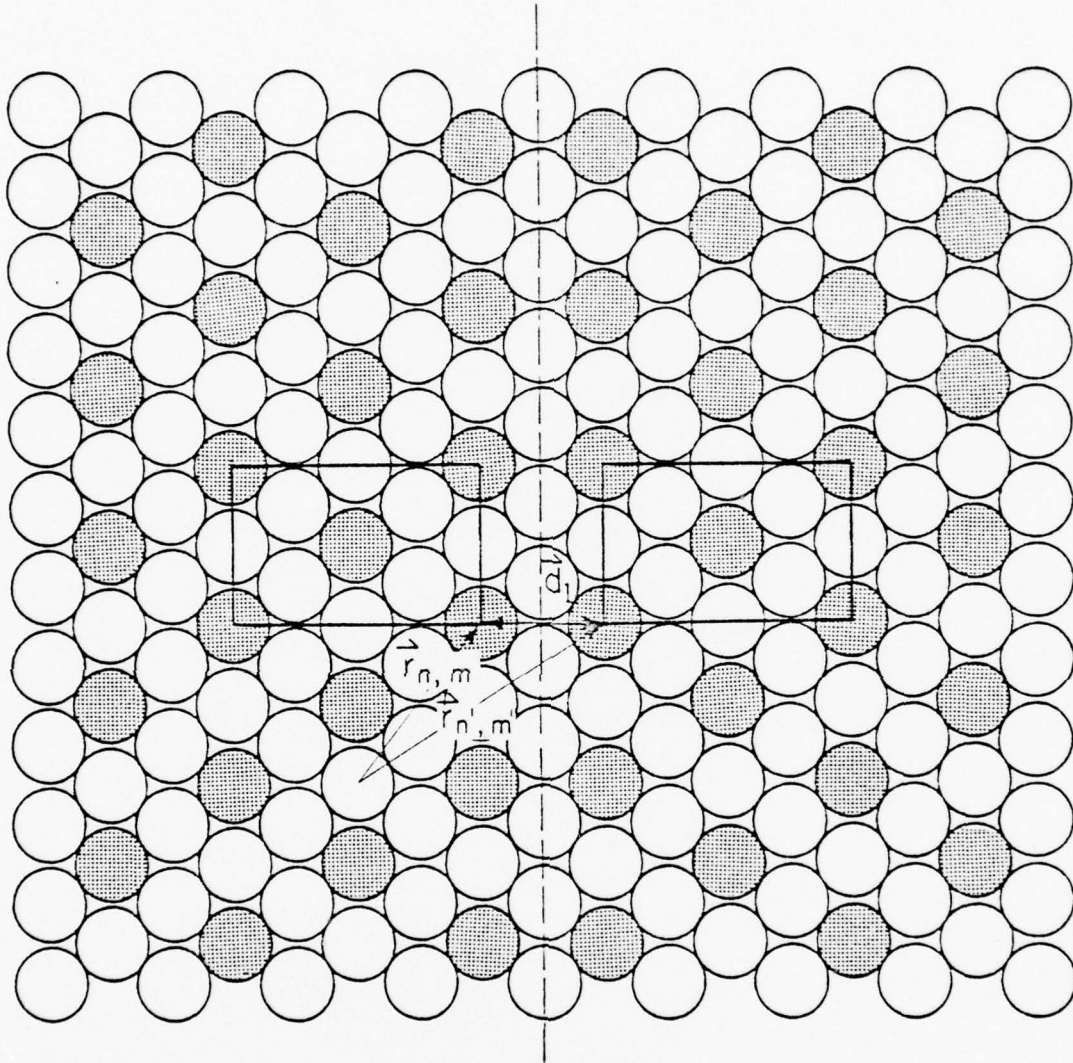
$$\Delta\vec{K} = \vec{K}_f \cdot \vec{r}_{n,m}. \quad (13)$$

Equation (11) then becomes

$$\psi = \psi_0 \sum_{n,m} f_{n,m} \exp\left[-\frac{i2\pi}{\lambda} (nac\cos\alpha + mbc\cos\beta)\right]. \quad (14)$$

The interference function,  $F$ , is the square of  $\psi$  or

$$F = \left\{ \sum_{n,m} f_{n,m} \cos\left[\frac{2\pi}{\lambda} (nac\cos\alpha + mbc\cos\beta)\right] \right\}^2 + \left\{ \sum_{n,m} f_{n,m} \sin\left[\frac{2\pi}{\lambda} (nac\cos\alpha + mbc\cos\beta)\right] \right\}^2, \quad (15)$$



AP-863

Figure 19.  $p(2 \times 2)$  domains on the (110) plane of tungsten;  $\vec{d}_1$  is the translation vector between the two domains.

where  $\cos\alpha = (\frac{\lambda}{a})h$ ,  $\cos\beta = (\frac{\lambda}{b})k$ ,  $\lambda$  the electron wavelength and  $h, k$  the indices of the diffracted beam. By calculating the value of  $F$  for a particular surface structure we obtain the symmetry, spacing and beam profiles of the diffraction pattern, but not their intensities.

Under certain circumstances, however, additional information about the atomic arrangement can be obtained. An adsorbed gas sometimes forms domains. When the domains are out of phase with one another, splitting of some of the beams may occur. This can be seen by examining the scattering from two domains, separated by a distance ( $\vec{d}_1$ ), as shown in Fig. 19. Using Eqs. (11) and (13), the scattered amplitude for the first domain is given by

$$\psi_1 = \sum_{n,m} f_{n,m} \exp[i\vec{K}_f \cdot \vec{r}_{n,m}] , \quad (16a)$$

and for the second domain denoted by 2,

$$\psi_2 = \sum_{n',m'} f_{n',m'} \exp[i\vec{K}_f \cdot \vec{r}_{n',m'}] . \quad (16b)$$

The interference function for both domains ( $F_{12}$ ) is given by  $[\psi_1 + \psi_2]^2$ , that is by

$$F_{12} = \left[ \sum_{n,m} f_{n,m} \exp(i\vec{K}_f \cdot \vec{r}_{n,m}) + \sum_{n',m'} f_{n',m'} \exp(i\vec{K}_f \cdot \vec{r}_{n',m'}) \right]^2 , \quad (17a)$$

$$F_{12} = F_1 + F_2 + \sum_{n,m} \sum_{n',m'} f_{n,m} f_{n',m'} [\exp(i\vec{K}_f \cdot \vec{r}_{n,m}) \exp(-i\vec{K}_f \cdot \vec{r}_{n',m'}) + \exp(-i\vec{K}_f \cdot \vec{r}_{n,m}) \exp(i\vec{K}_f \cdot \vec{r}_{n',m'})] , \quad (17b)$$

where  $F_1 = [\psi_1 \psi_1^*]$  and  $F_2 = [\psi_2 \psi_2^*]$ . If the domains are of equal size, then

$$F_{12} = 2F_1 + \sum_{n,m} 2 \cos(\vec{K}_f \cdot \vec{d}_1), \quad (17c)$$

where  $\vec{d}_1$  is the translation vector between the two domains. Equation (17c) can be simplified to [28]

$$F_{12} = 2F_1 [1 + \cos(\vec{K}_f \cdot \vec{d}_1)]. \quad (17d)$$

The maxima of  $F_1$  occur when  $\frac{\vec{K}_f}{2\pi} = h\vec{a}^* + k\vec{b}^*$ , where  $k$  and  $h$  are the indices of the diffracted beam and  $\vec{a}^*$  and  $\vec{b}^*$  are the reciprocal lattice vectors. When one of these maxima coincides with a minimum of the  $(1 + \cos(\vec{K}_f \cdot \vec{d}_1))$  term, beam splitting occurs. This happens when

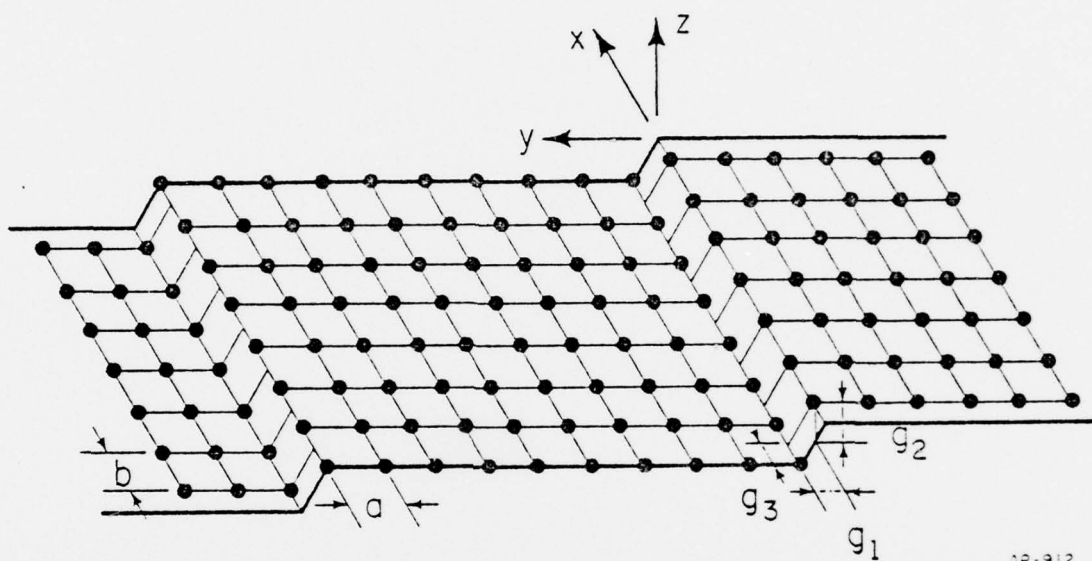
$$hn + km = \frac{1}{2} (2i + 1), \quad i = \text{integer}, \quad (18)$$

where  $\vec{d}_1 = n\vec{a} + m\vec{b}$ .

By application of Eq. (15) to a proposed surface structure, the symmetry spacing and beam profile of the resulting LEED pattern can be calculated. Beam splitting may be used to obtain insight into the growth mechanism of the adlayer, its size, the direction of the boundary and how well formed the domains are.

### III.2.B. Surface Defects

Perhaps the most common surface defects are steps or terraces. Ellis and Schwoebel [29] and Henzler [30] have shown theoretically and experimentally that a regular array of surface steps causes a characteristic splitting of many of the LEED beams into doublets or even multiplets. The terrace width can be determined from the separation of the spots which make up the doublet.



AP-912

Figure 20. Diagram of the surface used in Sec. III.2.B to calculate the effect of surface steps on LEED beam intensity.

A diagram of a surface with step edges running along the x axis is shown in Fig. 20; Fig. 21 shows the projection of this plane along the step direction. If we consider scattering from only the top most layer of Figs. 20 and 21 and use Eq. (11), the scattering factor for the first row of  $N+1$  lattice sites along the y direction is

$$\psi_y(x,z) = \psi_y(0,0) = f \sum_{q=0}^N \exp[iq\vec{K}_f \cdot \vec{a}] , \quad (19)$$

where  $f$  is the atomic scattering factor of each surface atom. For the second row the scattering factor is given by,

$$\psi_y(\vec{b},0) = f \sum_{q=0}^N \exp[i\vec{K}_f \cdot (q\vec{a} + \vec{b})] . \quad (20)$$

The scattering factor from the first terrace of  $M+1$  rows, where  $M$  is odd, is

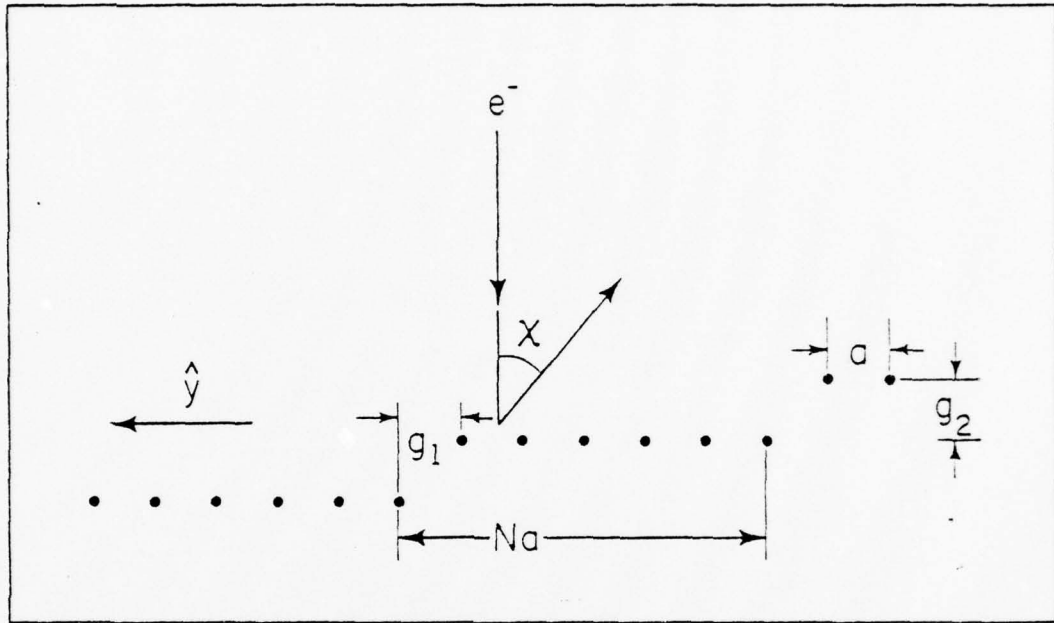
$$\begin{aligned} \psi^{(1)} &= f \left\{ \sum_{q=0}^N \exp(i\vec{K}_f \cdot q\vec{a}) + \sum_{q=0}^N \exp[i\vec{K}_f \cdot (q\vec{a} + \vec{b})] + \sum_{q=0}^N \exp[i\vec{K}_f \cdot (q\vec{a} + 2\vec{b})] + \dots \right\} \\ &= f [1 + \exp(i\vec{K}_f \cdot \vec{b})] \sum_{q=0}^N \exp[i\vec{K}_f \cdot q\vec{a}] \sum_{s=0}^{\frac{1}{2}(M-1)} \exp[i\vec{K}_f \cdot 2s\vec{b}] . \end{aligned} \quad (21)$$

The scattering factor from subsequent terraces is

$$\begin{aligned} \psi^{(2)} &= \psi^{(1)} \exp[i\vec{K}_f \cdot (N\vec{a} + \vec{s}_1 + \vec{s}_2 + \vec{s}_3)] \\ \psi^{(3)} &= \psi^{(1)} \exp[i\vec{K}_f \cdot (2N\vec{a} + 2\vec{s}_1 + 2\vec{s}_2)] . \end{aligned} \quad (22)$$

The total scattering factor  $\psi^{(T)}$  of  $n$  steps and  $n+1$  ( $n$  odd) terraces is

$$\psi^{(T)} = \sum_{p=1}^{n+1} \psi^{(p)}$$



AP-823

Figure 21. Projection of the stepped surface of Fig. 20 along the step direction.

$$= [1 + \exp(i\vec{k}_f \cdot (\vec{N}a + \vec{s}_1 + \vec{s}_2 + \vec{s}_3))] \times \exp[i\vec{k}_f \cdot (\vec{N}a + \vec{s}_1 + \vec{s}_2)2t] \quad (23)$$

Equation (23) can now be written as

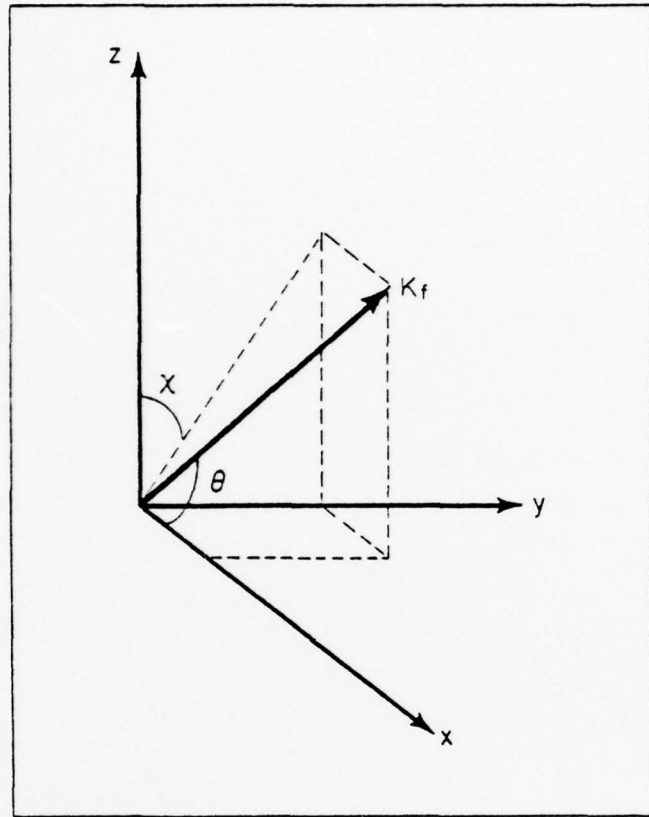
$$\begin{aligned} \psi^{(T)} = & f[1 + \exp(i\vec{k}_f \cdot \vec{a})] \sum_{q=0}^N \exp[i\vec{k}_f \cdot q\vec{a}] \sum_{s=0}^{\frac{1}{2}(M-1)} \exp[i\vec{k}_f \cdot 2s\vec{b}] \\ & \times [1 + \exp(i\vec{k}_f \cdot (\vec{N}a + \vec{g}_1 + \vec{g}_2 + \vec{g}_3))] \sum_{t=0}^{\frac{1}{2}(M-1)} \exp[i\vec{k}_f \cdot (\vec{N}a + \vec{g}_1 + \vec{g}_2)2t] \quad (24) \end{aligned}$$

The intensity distribution is given by the square of the absolute value of the scattering factor,

$$\begin{aligned} I = & 4f^2 \cos^2(\vec{k}_f \cdot \vec{a}) \left\{ 4 \cos^2 \left[ \left( \frac{\vec{k}_f}{2} \right) \cdot (\vec{N}a + \vec{g}_1 + \vec{g}_2 + \vec{g}_3) \right] \right\} \frac{\sin^2 \left[ \left( \frac{N+1}{2} \right) \vec{k}_f \cdot \vec{a} \right]}{\sin^2 \left[ \frac{\vec{k}_f \cdot \vec{a}}{2} \right]} \\ & \times \frac{\sin^2 \left[ \left( \frac{M+1}{2} \right) \vec{k}_f \cdot \vec{b} \right]}{\sin^2 [\vec{k}_f \cdot \vec{b}]} \frac{\sin^2 \left[ \left( \frac{n+1}{2} \right) \vec{k}_f \cdot (\vec{N}a + \vec{g}_1 + \vec{g}_2) \right]}{\sin^2 [\vec{k}_f \cdot (\vec{N}a + \vec{g}_1 + \vec{g}_2)]} \quad (25) \end{aligned}$$

Transforming this into the coordinate system illustrated in Fig. 22, where

$$\begin{aligned} \vec{k}_f \cdot \vec{a} &= \left( \frac{2\pi a}{\lambda} \right) \sin\theta \sin x \\ \vec{k}_f \cdot \vec{b} &= \left( \frac{2\pi b}{\lambda} \right) \cos\theta \\ \vec{k}_f \cdot \vec{g}_1 &= \left( \frac{2\pi g_1}{\lambda} \right) \sin\theta \cos x \\ \vec{k}_f \cdot \vec{g}_2 &= \left( \frac{2\pi g_2}{\lambda} \right) \sin\theta \cos x + \frac{2\pi g_2}{\lambda} \\ \vec{k}_f \cdot \vec{g}_3 &= \left( \frac{2\pi g_3}{\lambda} \right) \cos\theta \quad ; \quad (26) \end{aligned}$$



AP-911

Figure 22. Geometry appropriate to scattering from stepped surface. Terraces are parallel to the  $xy$  plane and steps are parallel to the  $x$  axis.

Therefore, the intensity at an angle  $\chi$ , when  $\theta = 90^\circ$  is given by

$$I(\chi) = \text{const.} \frac{\sin^2 \left[ \left( \frac{N+1}{2} \right) K a \sin \chi \right]}{\sin^2 \left[ \frac{K a}{2} \sin \chi \right]} \frac{\sin^2 \left[ (n+1) \frac{K}{2} (N a \sin \chi + g_1 \sin \chi + g_2 (1 + \cos \chi)) \right]}{\sin^2 [K(N a \sin \chi + g_1 \sin \chi + g_2 (1 + \cos \chi))]} \quad (27)$$

where  $K = \frac{2\pi}{\lambda}$ . The first term corresponds to diffraction from the terrace. The main maxima occur at angles  $\chi$ , where  $\frac{1}{2} K a [\sin(\chi)] = n\pi$ . In the limit of an infinite number of steps, and using the relationship

$$\lim_{n \rightarrow \infty} \frac{\sin^2 [(n+1) x]}{\sin^2 x} = \sum_{i=-\infty}^{\infty} \delta(x - i\pi) \quad (28)$$

the second term can be replaced by

$$\sum_{i=-\infty}^{\infty} \delta \left[ \frac{1}{2} K (N a) \sin \chi + \frac{1}{2} K g_1 \sin \chi + \frac{1}{2} K g_2 (1 + \cos \chi) \right] \quad (29)$$

This term depends only on the step width  $N a$ , the step height  $g_2$ , and horizontal displacement  $g_1$ . The separation of two adjacent delta functions is now given by

$$\Delta \chi = \frac{\lambda}{[(N a) \cos \chi - g_1 \sin \chi + g_2 \cos \chi]} \quad (30)$$

and for  $\chi \approx 0$ ,

$$\Delta \chi = \frac{\lambda}{N a + g_2} \quad (31)$$

From this expression the terrace width can easily be determined by measuring the angular separation of the (0,0) doublet at near normal incidence. From a practical point of view, this technique can only be used if the step

width is less than about 150 Å. For steps wider than this the beam splitting is so small that our LEED system is incapable of resolving the doublet.

### III.2.C. Measurements of Work Function Changes

The difference in the electrostatic potential between the inside and outside of a metal is termed the surface potential. The related properties—the work function and the contact potential difference, measure the free energy change that occurs when electrons are moved from one conductor to a vacuum and from one conductor to another, respectively. The formation of an adlayer modifies the dipole structure of the metal surface and therefore changes the work function. The effect may be evaluated in terms of the dipole moment produced by the adlayer. It can be shown that the change in the value of the work function corresponding to the formation of a layer with a fractional coverage  $\theta$  is

$$\Delta\phi = 4\pi\sigma_m M\theta \quad (32)$$

where  $M$  is the dipole moment/atom and  $\sigma_m$  the total sites available per unit area of the adsorbate. A review of techniques used for measuring surface potentials is given by Culver and Tompkins [31] and by Knapp [32].

To study the change in work function after the adsorption of a gas, our LEED system is modified to be used as a retarding diode analyzer. The retarding diode technique is a variation of the contact potential method described by Langmuir and Kingdon [33] and later by Skelton [34]. The only equipment needed, in addition to the standard LEED system, is a microammeter and a small dc power supply. The experimental arrangement

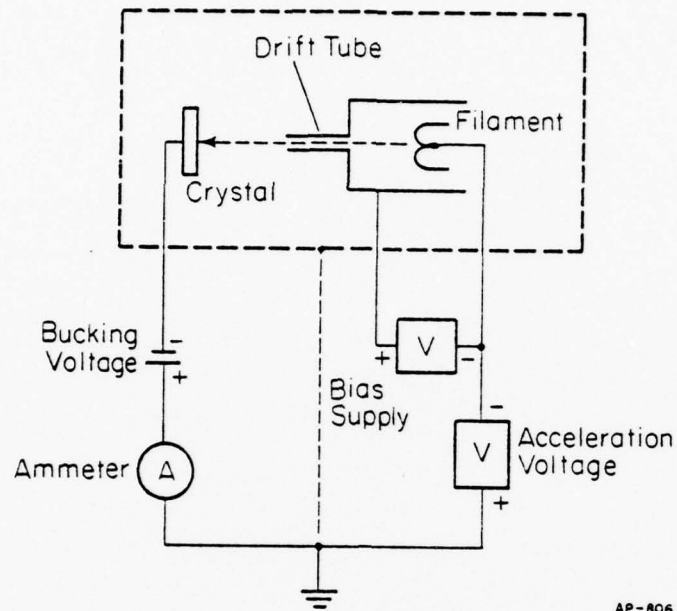
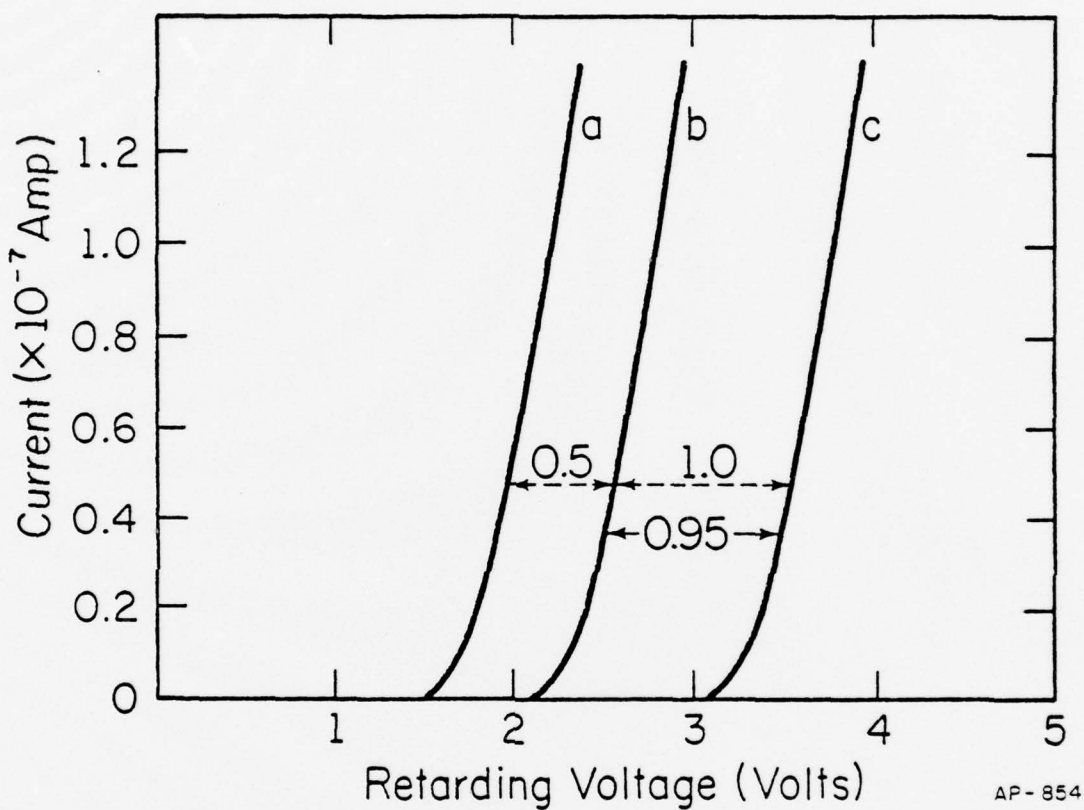


Figure 23. Block diagram of the retarding diode analyzer for measuring work function changes.



AP-854

Figure 24. Characteristic dc calibration curves obtained at different retarding voltages. In this case a 1 volt change in the bucking voltage produces a 0.95 volt shift in the I-V curve. a) bucking voltage = 20 volts, b) bucking voltage = 20.5 volts, c) bucking voltage = 21.5 volts; actual shift in I-V curve 0.95 volt.

is shown in Fig. 23. Retarding potential curves are derived by measuring the current,  $I_a$ , to the crystal as the accelerating voltage  $V$  is increased. In our system the primary beam voltage from the LEED gun is set at 21 volts and the current to the crystal is between  $10^{-7}$  to  $10^{-8}$  amperes. To check the accuracy of the retarding potential analyzer, a dc calibration is performed. Initially the primary emission current is  $\approx 50 \mu\text{A}$  and the accelerating voltage and the bucking voltage are identical. The accelerating voltage is then slowly increased. At some low voltage (relative to the bucking voltage) the electrons have barely enough energy to arrive at the crystal. As the acceleration voltage  $V$  is increased, the current to the crystal increases and eventually saturates (typically at about  $5 \times 10^{-7}$  amperes). This is then repeated for a number of different bucking voltages, and a dc calibration is obtained. A sample calibration is shown in Fig. 24. There, a 1 volt change in the bucking voltage produces a 0.95 volt shift in the I-V curve; the gain of the system is therefore 0.95. The shift of each I-V curve to the right with increasing bucking voltage is due to the change in potential of the crystal; if the surface potential itself changes, the I-V curve would also shift, and this shift would be proportional to the change in work function. In our experiment the accelerating voltage is held constant and instead the bucking voltage is varied; the accelerating voltage is always kept at 21 volts. The difference in voltage between the bucking voltage and the accelerating voltage is the retarding voltage in the I-V curve.

Consider, for example what happens when the work function increases after a gas is deposited on the surface. At any particular bucking voltage  $V$ , the current decreases and the I-V curve shifts to the right. If the slope

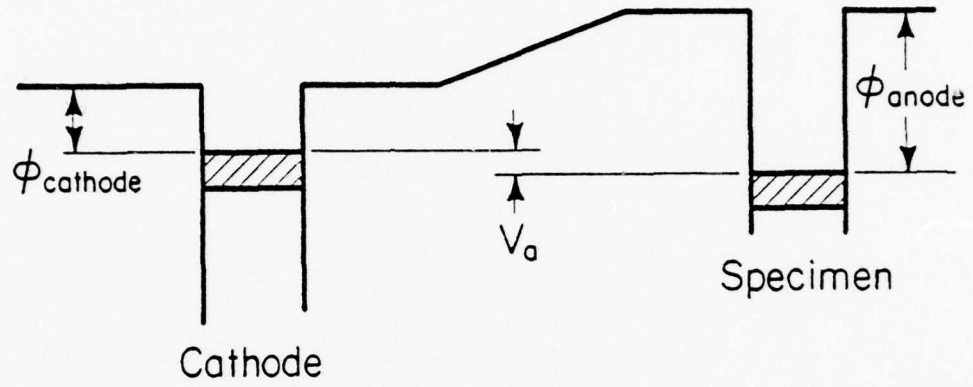
of the I-V curve (in the linear region) is constant, the change in I is proportional to the change in work function and the proportionality constant is the slope of the I-V curve.

When the LEED system is used in this manner to measure work function changes, there are three possible sources of error. The first is a change in the work function of the filament. Since the gun is not operated in the space charge limited mode, the adsorption of nitrogen on the cathode may affect the changes observed in the work function of the sample. Fortunately, the temperature of the filament is high enough that any adsorbed nitrogen will be desorbed at the operating emission current. In addition it can be shown that the emission current to the anode,  $I_a$ , is given by

$$I_a = A T_f^2 \exp[(V_a - \phi_{\text{anode}})/kT_f] , \quad (33)$$

where  $T_f$  is the filament temperature, A a constant,  $\phi_{\text{anode}}$  the work function of the anode and  $V_a$  is the difference in potentials between the cathode and the anode. From Fig. 25 we see that the anode current in the diode is not dependent on the value of the cathode work function, provided that  $\phi_{\text{cat}} < [\phi_{\text{anode}} - V_a]$ , where  $\phi_{\text{cat}}$  is the work function of the cathode.

The second possible source of error lies in a change in the reflection coefficient  $\bar{r}$  when gas is adsorbed on the surface. Equation (33) properly should include a factor  $(1-\bar{r})$ , where  $\bar{r}$  is the reflection coefficient of the electron at the anode and is taken to be independent of electron energy. A change in the reflection coefficient would manifest itself as a change in the slope of the I-V curve with surface coverages. Defocussing of the electron beam constitutes yet a third source of error. For small values of  $I_a$ , the electrons arriving at the crystal have almost zero energy.



AP-920

Figure 25. Energy level diagram of the retarding potential diode.

The electron beam is thus easily defocussed and more of the electrons miss the sample. Beam defocussing is reduced by using a large bucking voltage and by operating the gun in such a way that electrons leave the gun at high velocities and decelerate only when they arrive at the crystal. This is accomplished by biasing the drift tube of the LEED gun as shown in Fig. 23.

The usefulness of surface potential measurements, using the retarding diode technique, lies in its simplicity, minimal equipment requirement and sensitivity to changes that occur on the surface. The retarding diode technique can easily detect changes of less than 0.01 volt in the surface potential. Since the adsorption of a monolayer on the surface typically produces a change of several tenths to one volt in the surface potential, small changes in surface coverage should readily be detected.

## IV. RESULTS

IV.1. Specimen CharacterizationIV.1.A. Contamination

The major sources of surface contamination are impurity diffusion from the bulk and sample holder, from the background gas and possibly from the nitrogen gas supply. To insure the purity of the nitrogen prior to exposure to the crystal, the gas is passed over freshly evaporated nickel films before the start of an experiment.

Prior to an experiment the sample is flashed to  $2800^{\circ}\text{K}$  and an Auger spectrum of the tungsten surface is taken to insure its cleanliness. The crystal is then exposed to nitrogen and another Auger spectrum is taken. The only new peaks visible are the nitrogen triplet which occurs at about 380 volts; this is shown in Fig. 26. From this we conclude that any contamination from the gas supply is too small to be detected. The only contamination found results from the dissociation of the background gas on the surface. After 4 to 5 hours in a vacuum of  $10^{-10}$  to  $10^{-11}$  Torr, as measured by the nude ion gauge in the main chamber, a slight carbon peak is found, amounting to approximately one-half that of the carbon peak in Fig. 9. The surface carbon, presumably arising from the adsorption of  $\text{CO}$ , is easily removed by a flashing to several thousand  $^{\circ}\text{K}$  for a few seconds.

IV.1.B. Surface Arrangement

Perhaps the most common surface defects are steps. In Sec. III.2.B. we discussed a method by which LEED measurements are used to determine the step density. At several different locations along the crystal edge



we observed evidence of beam splitting due to surface steps. This is evident in the LEED picture of Fig. 27, which shows the (0,0) beam, slightly displaced from the center of the LEED screen, in order to be photographed. The primary beam energy is 35 volts and from the splitting we are able to estimate, using Eq. (31), that near the crystal edge the terrace widths are approximately 30 atoms wide. The step edges are found to be parallel to the [113] direction. When the LEED beam is moved to the center of the crystal no splitting is evident. This is not meant to imply that there are no steps in the center of the crystal. In the center the steps could be arranged in a random array, or the terraces may be wider than about 30-40 atoms spacings. For terrace widths exceeding 30-40 atom spacings the angular separation of the doublet is less than  $1^\circ$  and we would be unable to resolve such a doublet.

#### IV.2. Ordinary Nitrogen Layers on W(110)

##### IV.2.A. Adsorption and Desorption of $\gamma$ Nitrogen from the W(110)

Since we are using electron stimulated dissociation of  $\gamma$  nitrogen to create our localized surface deposits (as will be discussed in greater detail in Sec. IV.3.A), we need to better understand the interaction of  $\gamma$  nitrogen with the (110) plane of tungsten. To this end flash desorption is used to follow the desorption kinetics of  $\gamma$  nitrogen. After the crystal is used to follow the desorption kinetics of  $\gamma$  nitrogen. After the crystal is cooled to  $95^\circ\text{K}$  and exposed to predetermined amounts of nitrogen, the crystal is resistively heated to a temperature  $T \approx 300^\circ\text{K}$ . A residual gas analyzer monitors the amount of nitrogen liberated during the heating interval, as a function of  $T$ . Both mass 14 and 28 peaks are compared and



Figure 27. Splitting of the (0,0) beam, due to a regular array of surface steps, near the edge of the crystal. The primary beam voltage is 35 volts.

the desorption rate curves are identical in shape and peak desorption temperature. It is concluded from this, and the surface contamination measurements mentioned earlier, that the contamination from CO (also mass 28) is insignificant.

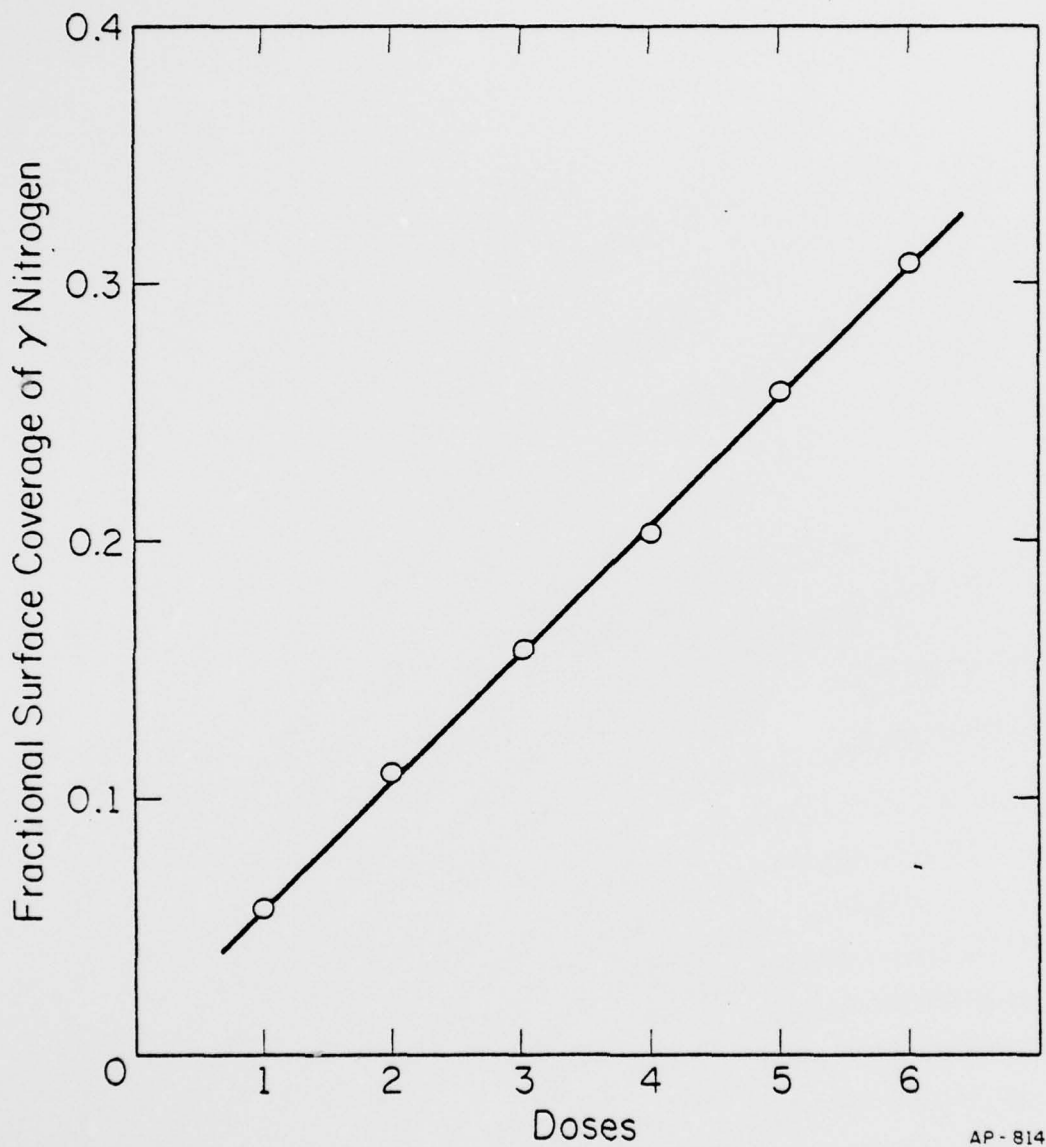
In general, the rate of thermal desorption of a gas from a unit surface area is given by [35,36]

$$N(t) = - \frac{dC(t)}{dt} = \nu_n C^n(t) \exp[-E_{des}/RT] , \quad (34)$$

where  $N$  is the number of atoms desorbed per unit area per unit time,  $n$  the desorption order,  $\nu_n$  the characteristic frequency,  $E_{des}$  the activation energy of desorption, and  $C(t)$  the surface concentration. In flash desorption measurements, a surface containing an adsorbate at an initial concentration  $C_0$  is rapidly heated, usually in such a way that

$$T = T_0 + \alpha t , \quad (35)$$

$T_0$  being the initial temperature and  $\alpha$  the heating rate. The pressure rise in the system is proportional to  $\frac{dC(t)}{dt}$  if the pumping speed is high. This pressure rise can be recorded as a function of temperature or time. By integrating the desorption rate, Eq. (34), the number of surface atoms desorbed can be calculated. This is accomplished by measuring the area under the flash desorption curve. By exposing the crystal to increasing doses of nitrogen, followed by the integration of the observed flash desorption curve, the surface coverage per dose can be calculated, relative to some standard exposure. For small doses the coverage is found to be proportional to the exposure. Figure 28 shows the amount of nitrogen desorbed for exposures ranging from one to six small doses. All areas under the



AP-814

Figure 28. Fractional surface coverage of  $\gamma$  nitrogen for 1 to 6 small doses. The crystal is initially at  $95^{\circ}\text{K}$ , the gas is throughout at  $300^{\circ}\text{K}$ .

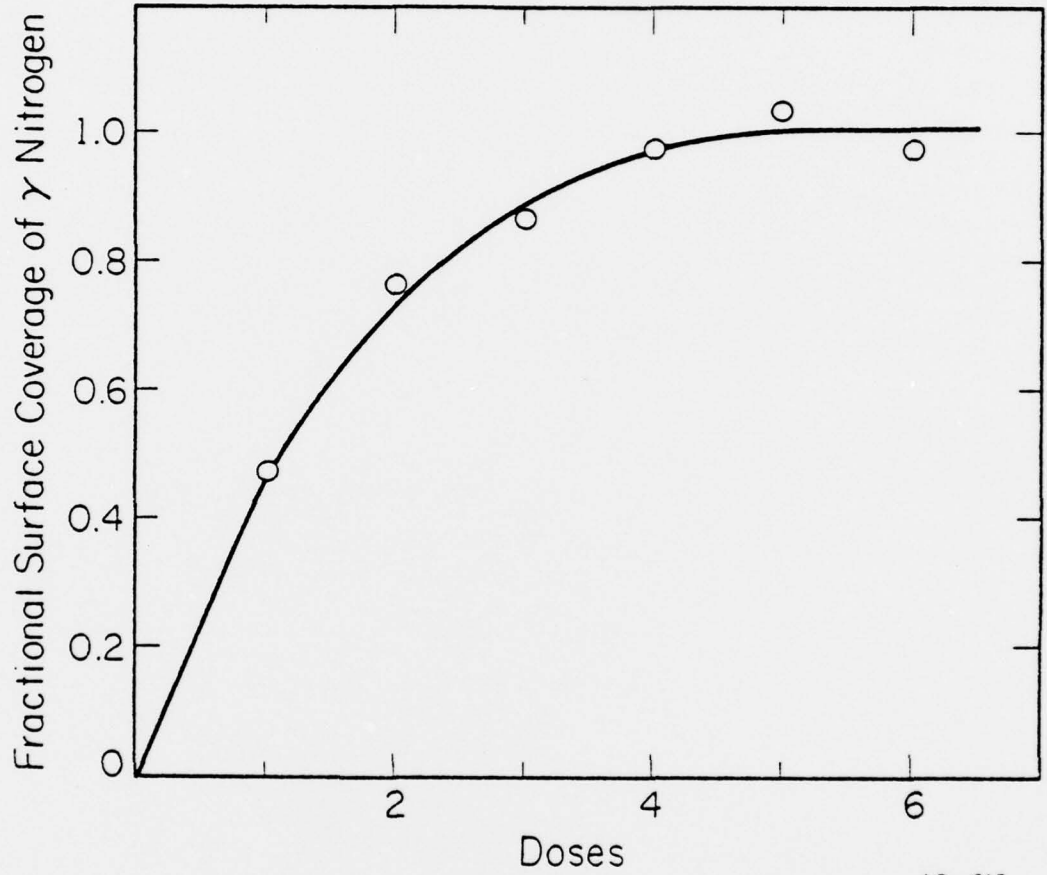
desorption curve are relative, with the area for a saturated surface taken as unity. For large doses, the amount of nitrogen desorbed became non-linear for coverages  $> 0.4$  of the saturated surface. Figure 29 shows the relative amount of nitrogen desorbed after exposures of 1 to 6 large doses. If we assume that the saturation coverage of  $\gamma$  nitrogen on the (110) plane is one monolayer or  $1.4 \times 10^{15}$  molecules/cm<sup>2</sup>, and the sticking coefficient for small coverages is  $\approx 1$  [37], then one small dose corresponds to an impingement of about  $7 \times 10^{13}$  molecules/cm<sup>2</sup>, and one large dose is equal to an impingement of  $5.88 \times 10^{14}$  molecules/cm<sup>2</sup>.

Figure 30 shows several thermal desorption curves plotted on the same scale. Within the large peak centered near 152°K, there appear to be at least 1, and probably more, discrete sub-peaks. The major peak is associated with  $\gamma$  nitrogen desorbing from the (110) plane, the smaller one (ones) at higher temperature are possibly due to desorption from the edges. The crystal is a disc  $\approx \frac{1}{4}$ " in diameter and 0.015" thick. This results in an edge area which is  $\approx 11\%$  of the total crystal area. Therefore, some of the desorbed nitrogen originated from planes other than the (110). At still higher temperatures (above 1400°K) we notice the desorption of  $\beta$  nitrogen.

For a first-order desorption process the temperature  $T_p$  at the peak in the desorption curve can be found from Eq. (34), to be

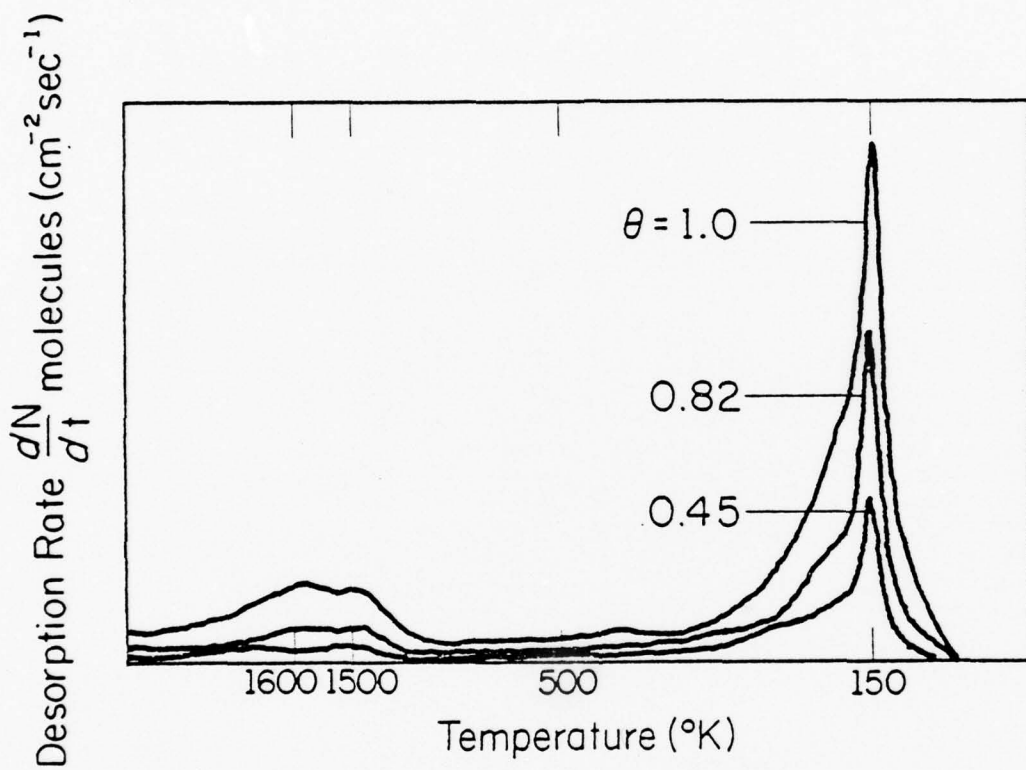
$$\frac{E_{des}}{RT_p} = \frac{\nu_1}{\alpha} \exp(-E_{des}/RT_p) . \quad (36)$$

The shape of the entire desorption curve can also be calculated using Eq. (34), assuming a high pumping speed. For a linear heating schedule and a first order desorption process, integration of Eq. (34) yields



AP-813

Figure 29. Surface coverage of  $\gamma$  nitrogen after 1 to 6 large doses. Adsorption temperature  $95^{\circ}\text{K}$ .



AP-830

Figure 30. Desorption rate of molecular nitrogen from the (110) plane of tungsten. The nitrogen is initially deposited at  $95^{\circ}\text{K}$ . The three initial coverages are 1.0, 0.82 and 0.45 monolayer.

$$\begin{aligned}
 - \int_{C_0}^{C'} \frac{dC}{C} &= \frac{\nu}{\alpha} \int_{T_0}^{T'} \exp(-E_{\text{des}}/RT) dT, & (37) \\
 &= \ln \left[ \frac{C_0}{C_p} \right] \quad \text{for } n=1,
 \end{aligned}$$

where  $C_0$  is the coverage at the start of the temperature sweep, and  $C_p$  is the coverage at  $T_p$ . Substituting  $u = -E_{\text{des}}/RT$ , integrating by parts and using the identity

$$\int_{-\infty}^u \frac{\exp(t) dt}{t} = \frac{\exp(u)}{u} \left[ 1 + \left( \frac{1!}{u} \right) + \left( \frac{2!}{u^2} \right) + \dots \right] \quad \text{for } u \gg 1, \quad (38)$$

we obtain the general shape of the flash desorption curve as

$$\frac{N}{N_p} = \left\{ \exp \left[ \frac{E_{\text{des}}}{R} \left( \frac{1}{T} - \frac{1}{T_p} \right) + \left( \frac{T}{T_p} \right)^2 \exp \left[ - \frac{E_{\text{des}}}{R} \left( \frac{1}{T} - \frac{1}{T_p} \right) \right] \right\}^{-1}. \quad (39a)$$

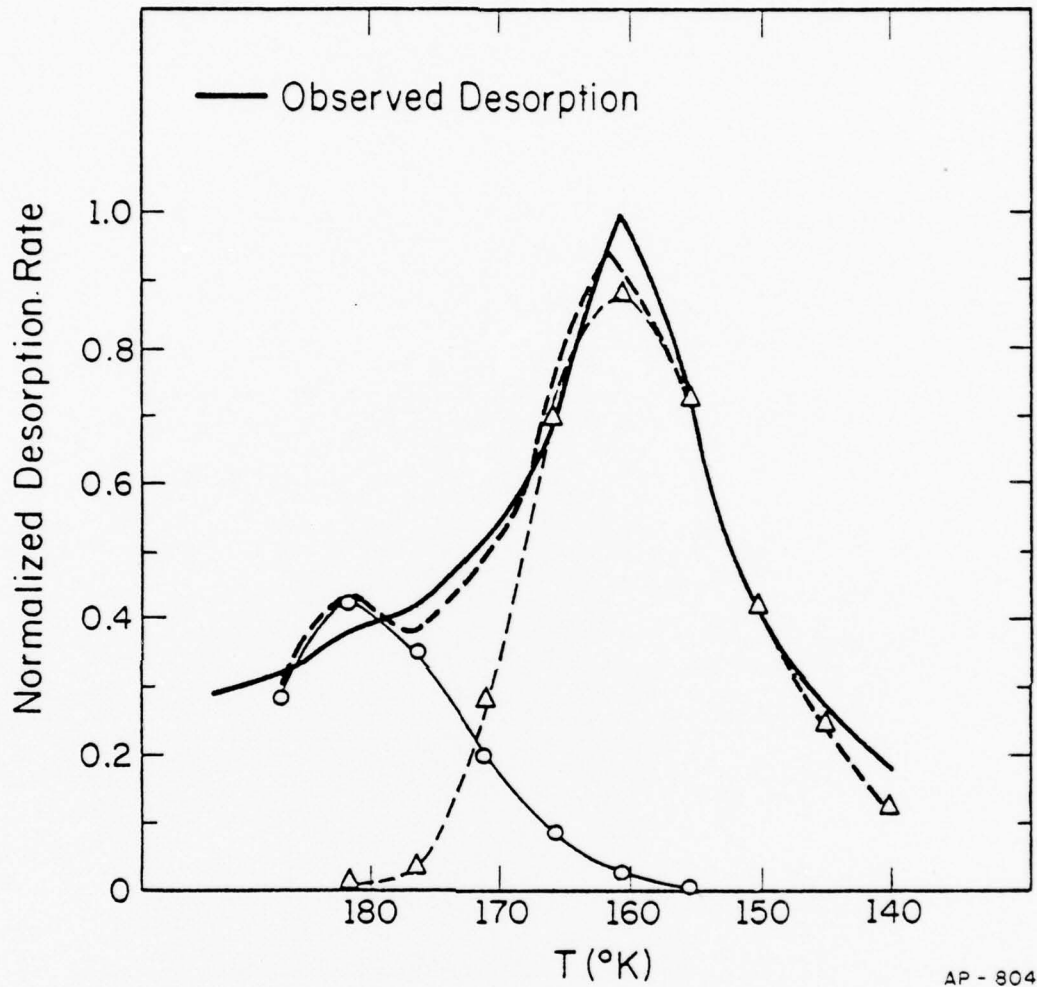
Here  $N$  is the number of desorbed species ( $\text{cm}^{-2} \text{sec}^{-1}$ ), and  $N_p$  the number desorbed ( $\text{cm}^{-2} \text{sec}^{-1}$ ) at  $T_p$ . For a surface species bound in  $j$  different states, the shape of the desorption curve for ( $n=1$ ) is given by

$$\frac{N_{\text{Total}}}{N_p} = \sum_{i=1}^j \left\{ \exp \left[ \frac{E_{\text{des}}^{(i)}}{R} \left( \frac{1}{T} - \frac{1}{T_p^{(i)}} \right) + \left( \frac{T}{T_p^{(i)}} \right)^2 \exp \left[ - \frac{E_{\text{des}}^{(i)}}{R} \left( \frac{1}{T} - \frac{1}{T_p^{(i)}} \right) \right] \right\}^{-1}. \quad (39b)$$

Even without a complete analysis, a number of important facts can be derived for the desorption kinetics of nitrogen from the (110) plane of tungsten [36,39]. The peak desorption temperature of the  $\gamma$  states,  $T_p^{\gamma}$ , is the same independent of initial coverage. This can only be true for a first-order desorption process with a constant desorption energy.

Looking at the high temperature side of the  $\gamma$  desorption curves we see that the curves have a shoulder. This is probably due to another molecular entity desorbing with a slightly different energy. If we assume that there is only one state on the high temperature side, and that it follows first-order desorption kinetics, then we can easily separate the two desorption processes. This is accomplished by assuming that the large desorption peak at approximately  $150^{\circ}\text{K}$  is composed of contributions from nitrogen bound in two states, with different values of  $E_{\text{des}}$  and  $\nu_1$ . We know the shape of the total desorption curve ( $N_{\text{Total}}/N_p$ ) and the peak desorption temperature  $T_p^{\text{Total}}$  ( $152^{\circ}\text{K}$ ) from Fig. 30. All that remains is to calculate the values of the desorption parameters of the low temperature state, designated  $E_{\text{des}}^{(1)}$ ,  $\nu_1^{(1)}$ , and of the state that desorbs at a slightly higher temperature  $E_{\text{des}}^{(2)}$ ,  $\nu_1^{(2)}$ . The values of the desorption parameters are obtained by varying  $E_{\text{des}}^{(1)}$ ,  $E_{\text{des}}^{(2)}$ ,  $\nu_1^{(1)}$ ,  $\nu_1^{(2)}$  in Eq. (39b) until the best fit to the observed desorption curve is obtained. A copy of the computer program which accomplishes this fitting is given in Appendix B.

The result of the separation of the two desorption curves is shown in Fig. 31. Along with the original flash desorption curve and the separated desorption curves is the sum of the latter two. This sum does not add up to the experimentally observed desorption rate. Since there are a multitude of different crystal planes located along the edge, we are probably dealing with a number of different states that vary slightly in their desorption energy and we would not expect this simple model to give the observed curve. This method does, however, give an estimate of the activation energy of desorption from the (110), which we find to be  $E_{\text{des}}^{(1)} = 5.4 \pm .76$  kcal/mole



AP - 804

Figure 31. Decomposition of the flash desorption curve for  $\gamma$  nitrogen into two first order processes, a)  $E_{\text{des}}^{(1)} = 5.4$  kcal/mole,  $\nu_1^{(1)} = 10^{10}$  sec $^{-1}$  ----, b)  $E_{\text{des}}^{(2)} = 8.7$  kcal/mole,  $\nu_{\text{des}}^{(2)} = 1.52 \times 10^{12}$  sec $^{-1}$  \_\_\_\_\_, c) the sum of a and b ....

with  $\nu_1^{(1)} = 10^{10} \text{ sec}^{-1}$ , for a surface coverage of 0.82 monolayer. The second state gives  $E_{\text{des}}^{(2)} = 8.7 \pm 1.9 \text{ kcal/mole}$  with  $\nu_1^{(2)} = 1.5 \times 10^{12} \text{ sec}^{-1}$ . We have analyzed the desorption rate of  $\gamma$  nitrogen from the (110) plane of tungsten for three different initial concentrations, 0.45, 0.82 and 1.0 monolayer. The results of this analysis are shown in Table 1.

Table 1

Flash Desorption Parameters of  $\gamma$  Nitrogen from the W(110) Coverage

Coverage (monolayer)	$E_{\text{des}}^{(1)}$ (kcal/mole)	$\nu_1^{(1)}$ ( $\text{sec}^{-1}$ )	$E_{\text{des}}^{(2)}$ (kcal/mole)	$\nu_1^{(2)}$ ( $\text{sec}^{-1}$ )
0.45	5.2	$8.8 \times 10^9$	7.95	$2.7 \times 10^{11}$
0.82	5.4	$1.0 \times 10^{10}$	8.7	$1.5 \times 10^{12}$
1.0	5.1	$6.0 \times 10^9$	8.05	$6.0 \times 10^{11}$

The values for  $E_{\text{des}}^{(2)}$  and  $\nu_1^{(2)}$  characteristic of the higher temperature state are very similar to those obtained for the flash desorption of  $\gamma$  nitrogen from polycrystalline tungsten surfaces [8]. It may be that the shoulder we observed is due to the desorption of molecular nitrogen from the edges of the crystal. The major (110) peak has an unusually low prefactor, when compared to that of polycrystalline and other planes of tungsten [8,14]. The activation energy and prefactor, however are both very similar to the only work that has been done with  $\gamma$  nitrogen on the (110) plane, in which the activation energy for desorption was found to be  $E_{\text{des}} = 6.4 \text{ kcal/mole}$  for  $\nu_1 = 10^{10} \text{ sec}^{-1}$  [37].

From the flash desorption curve of Fig. 30 we also notice that there is some  $\beta$  nitrogen formed; the desorption temperature for this state is  $\approx 1500^\circ\text{K}$ . The  $\beta$  on the (110) plane amounts to about 7% of the total gas desorbed as determined by comparing the area under the  $\gamma$  and  $\beta$  parts of the desorption curve. Whether the formation of  $\beta$  occurs at  $95^\circ\text{K}$ , or whether it occurs while the crystal is being flashed, is not known. From the desorption curves little information can be obtained on the desorption kinetics of  $\beta$  nitrogen. However, we do notice that the peak desorption temperature of  $\beta$  nitrogen,  $T_p^\beta$ , depends upon concentration, decreasing with increasing coverage. This is indicative of a second-order reaction [35,36].

#### IV.2.B. Structure of the Gas Layer

When a clean tungsten (110) surface (at room temperature) is exposed to nitrogen, also at room temperature, a distinctive change in the LEED pattern is observed. Fig. 32 shows the LEED pattern as the crystal is exposed to progressively larger amounts of nitrogen. Prior to each photograph the crystal is heated for several seconds at  $800^\circ\text{K}$  to fully develop the LEED pattern. In this sequence of pictures the (0,0) and the  $(1, \bar{1})$  beam are obscured by the crystal holder and one of the heating wires. With increasing coverage, as determined by Auger spectroscopy, and heating to  $800^\circ\text{K}$  for several seconds, a  $p(2 \times 2)$  pattern becomes visible, indicating the existence of a new surface periodicity with a unit cell twice that of the old surface net, as shown in Fig. 19. The basic arrangement is one in which the nearest neighbor sites around a given nitrogen atom are left vacant. It should be noted that, as the pattern develops, all of the half order beams split, as shown in Fig. 32c, d, e, and f. This splitting affords some insight into the growth mechanism of a nitrogen gas layer.

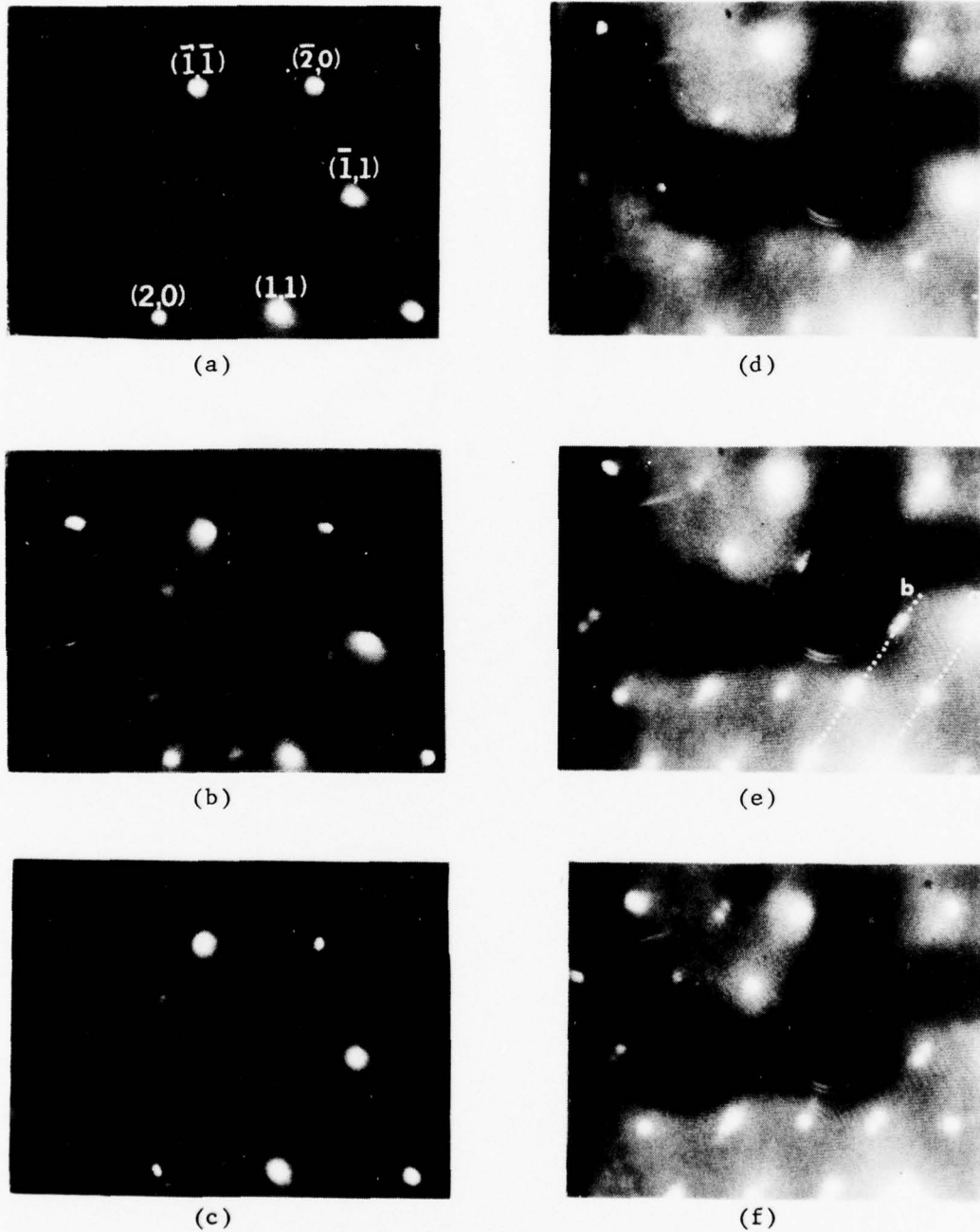


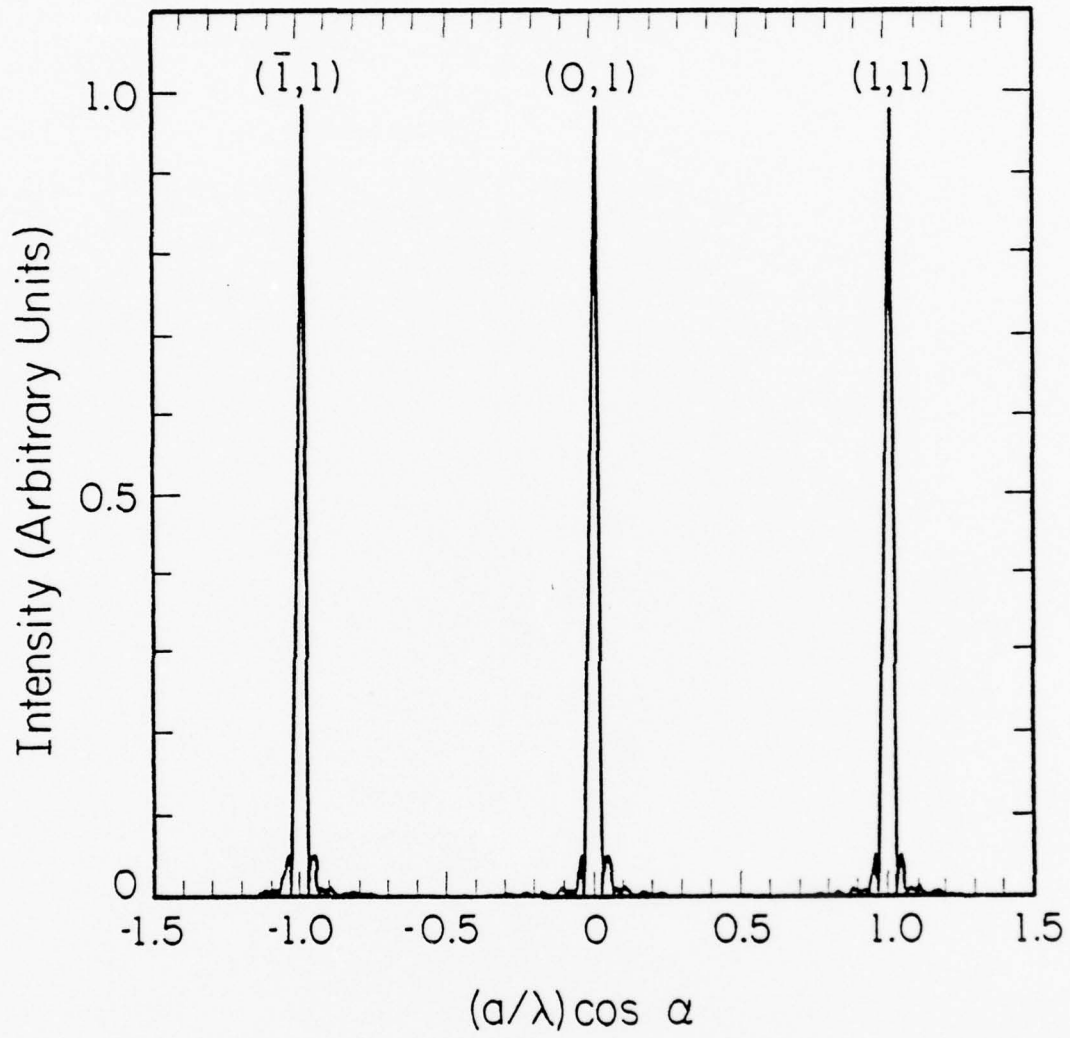
Figure 32. Changes in LEED pattern when initially clean W(110) is exposed to progressively greater amounts of nitrogen. In Fig. b, c, d, and f, the sample is briefly heated to  $800^{\circ}\text{K}$  for several seconds after exposure. The pattern in e is obtained after annealing at room temperature for 15 minutes. The surface concentrations are, a) clean, b)  $\approx 0.1$  monolayer, c)  $\approx 0.18$  monolayer, d)  $\approx 0.2$  monolayer, e)  $\approx 0.25$  monolayer, f)  $\approx 0.25$  monolayer.

Beam splitting is a well known phenomenon, and arises from the formation of surface domains which are out of phase with each other, as illustrated in Fig. 19. The domains of Fig. 19 each have the same surface structure, a  $p(2 \times 2)$ , with the vector  $\vec{d}_1$  connecting the domains. In this case  $\vec{d}_1$  is not a net vector of the superlattice and the domains are out of phase. From the discussion in Sec. III.2.A., the only beams that will be split are those which satisfy Eq. (18),

$$hn + km = \frac{1}{2} (2i + 1) \quad i = \text{integer}, \quad (18)$$

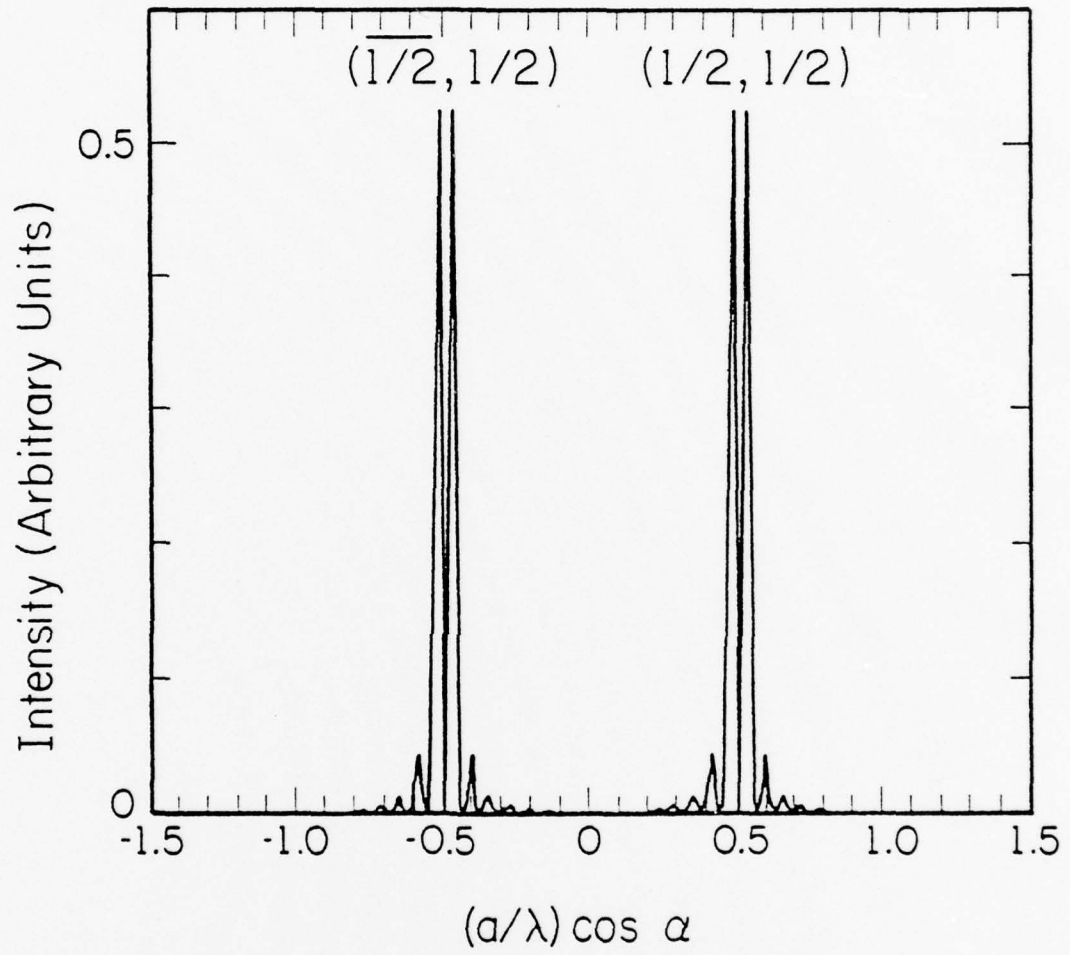
where  $\vec{d}_1 = n\vec{a} + m\vec{b}$ . In this case, the only LEED beams that are affected are those in which  $h$  and  $k$  are odd multiples of  $\frac{1}{2}$ . When the antiphase boundaries are parallel and regularly spaced, the beam splitting is in a direction perpendicular to the boundary. A surface structure which results in the observed  $p(2 \times 2)$  LEED pattern, with the proper beam splitting is illustrated in Fig. 19. That the surface structure of Fig. 19 does indeed result in the correct LEED pattern was verified by using Eq. (15) to calculate the beam intensity along several characteristic directions. These directions are shown in Fig. 32e. The surface lattice consisted of 2  $p(2 \times 2)$  domains separated by a translation vector  $\vec{d}_1 = a\hat{x}$ , as illustrated in Fig. 19, each domain being comprised of 128 adatoms. The result of this calculation is shown in Figs. 33 and 34, and agree with the LEED pattern of Fig. 32e. The location of the LEED beams in the  $p(2 \times 2)$  structure are listed in Table 2.

It is not necessary to heat the crystal, after nitrogen exposure, in order to obtain the  $p(2 \times 2)$ . Immediately after exposure no new structure is noticed in the LEED pattern; however after 10-20 minutes at room



AP-924

Figure 33. Calculated scattered intensity along line (a) of Fig. 32e.



AP-925

Figure 34. Calculated scattered intensity along line (b) of Fig. 32e.

Table 2

LEED Beam Location

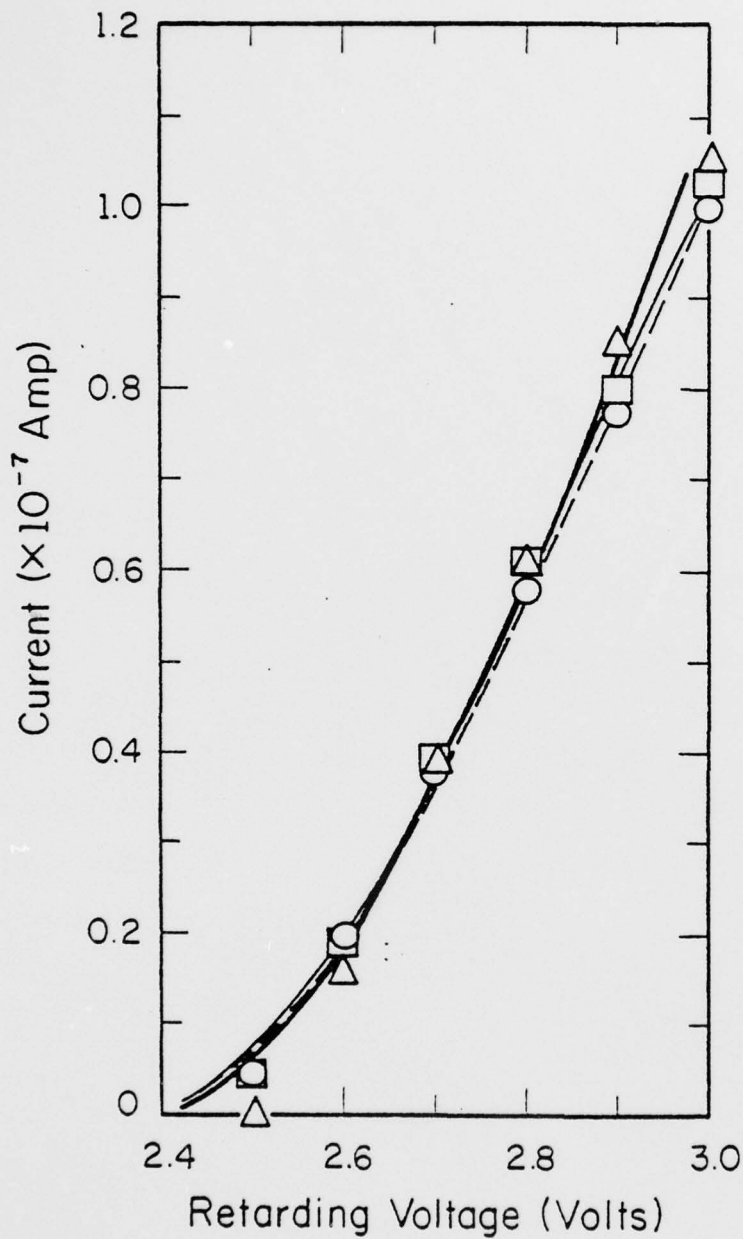
p(2 x 2)

$$(i, j) \quad \begin{array}{l} i = -1, 0, 1 \\ j = -1, 0, 1 \end{array}$$

$$\left( \begin{array}{c} \underline{n} \\ \underline{2} \end{array}, \begin{array}{c} \underline{m} \\ \underline{2} \end{array} \right) \quad \begin{array}{l} n = -1, 1 \\ m = -1, 1 \end{array} \} \Rightarrow \text{doublet}$$

temperature, a p(2 x 2) pattern is observed and is shown in Fig. 32e. This behavior is understandable if initially the atoms are not arranged in a periodic structure on the surface but become ordered on the surface by diffusion. An estimate of the root mean square displacement of the surface atom based on these LEED measurements will be given in Sec. IV.5.

A slight modification of the standard 4-grid LEED system (discussed in Sec. III.2.C.) permits us to measure the change in work function accompanying the changes in the LEED pattern. Fig. 35 shows the changes that occur in the characteristic I-V curve as the surface is saturated with  $\beta$  nitrogen at room temperature. After the  $\beta$  nitrogen is deposited, a slight change in the I-V curve is actually noticed. No further changes occur after the crystal is warmed and a p(2 x 2) LEED pattern becomes visible. The initial change is probably not due to a change in the work function, but instead arises from a slight change in the reflection coefficient  $\bar{r}$  as discussed in Sec. III.2.C. Notice that the various curves in Fig. 35 are not displaced with respect to one another, as they should be if the work function changed, but actually have a slightly different slope



AP-864

Figure 35. Changes in the I-V curve of a) a clean tungsten (110) surface  $\Delta$  —, b) the same surface saturated with nitrogen at room temperature  $\square$  —, c) the saturated surface heated to 800°K for several seconds to produce a p(2x2) LEED pattern  $\circ$  ---. Accelerating potential of the electron beam is 21 volts.

(in the linear region). This is just the effect expected if the reflection coefficient changed. At lower coverages there is no noticeable difference in any of the I-V curves. This agrees with earlier studies [14,15] in which no change in the work function was found after exposing the tungsten (110) plane to nitrogen at room temperature.

#### IV.2.C. Desorption Kinetics of Nitrogen Adsorbed at Room Temperature

Before we begin to study the surface diffusion of nitrogen on the (110) plane of tungsten, it is first necessary to characterize the surface gas layer. Not only is it important to know which state the gas is bound in, but it is also of considerable interest to compare the binding energy of the gas on the surface to the activation energy for diffusion. The most common method of obtaining the desorption parameters of a gas adsorbed on a surface is to heat the sample at a fixed rate and measure the accompanying pressure change, either with an ion gauge or mass spectrometer. This was just illustrated by the desorption measurements of  $\gamma$  nitrogen. Another technique that can be used to follow the desorption process involves the use of Auger spectroscopy. Basically the experimental procedure is simple. A gas layer is deposited on the surface and Auger spectroscopy is used to determine the amount of gas remaining on the surface after the crystal is heated to various temperatures. This has the advantage of determining the amount of gas on the area of interest only. This is the first time that Auger spectroscopy has been used to study the desorption kinetics of an adsorbed gas layer. To determine the characteristics of the gas layer on which the diffusion studies will be made, we compare the

desorption of  $\beta$  nitrogen, using Auger spectroscopy to those obtained by flash desorption [13]. It is known that nitrogen adsorbed at room temperature on the (110) plane of tungsten is bound in the  $\beta$  state. This state exhibits second-order desorption kinetics with a rate given by Eq. (34), so that the concentration  $C(t)$  after a heating interval of  $t$  seconds is given by

$$\frac{C(t)}{C_0} = \frac{1}{1 + C_0 v_2 t \exp\left(\frac{-E_{des}}{RT}\right)}, \quad (40a)$$

where  $C_0$  is the initial concentration of nitrogen adsorbed on the surface.

Auger spectroscopy does not measure the surface concentration of nitrogen, but actually gives a signal proportional to  $M(t)$ , the number of atoms in the beam area. For a uniform surface concentration (within the beam area) the Auger signal is proportional to  $C(t)$ . The resultant Auger signal (proportional to  $M(t)$ ) is given by

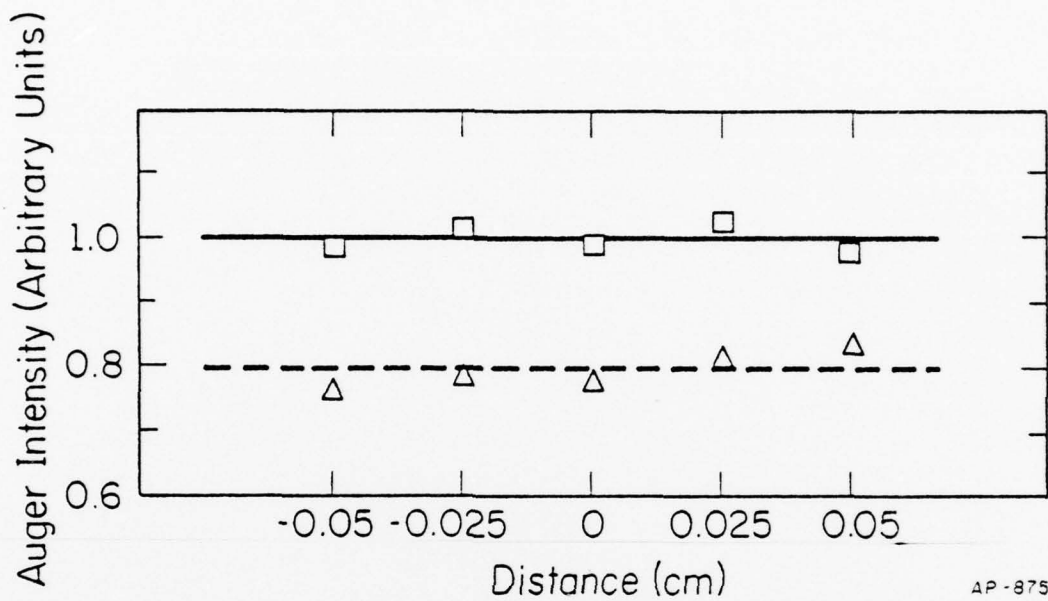
$$\frac{M(t)}{M_0} = \frac{1}{1 + C_0 v_2 t \exp\left(\frac{-E_{des}}{RT}\right)}, \quad (40b)$$

where  $M_0$  is the initial number of atoms sampled and  $M(t)$  the number of gas atoms within the beam after heating for  $t$  seconds. This becomes

$$\ln \left[ \frac{1}{t} \left( \frac{M_0}{M(t)} - 1 \right) \right] = \ln [C_0 v_2] - \frac{E_{des}}{RT}. \quad (40c)$$

The actual experimental procedure is as follows. After the surface is cleaned of impurities, the crystal is exposed to a saturation dose of nitrogen gas. Since the sticking coefficient of nitrogen on the (110)

plane at room temperature is  $< .004^{13}$ , we are forced to expose the crystal to  $10^{-6}$  Torr of nitrogen for 1000 seconds. This enables us to obtain a reasonable surface concentration that can be detected by Auger spectroscopy. After the background gas is removed, an Auger scan in the energy range of the nitrogen  $KL_{2,3}L_{2,3}$  transition is made. The peak to peak height of this Auger transition is then equal to  $\phi M_0$ ,  $\phi$  being a proportionality constant. A number of Auger scans are made at different locations on the crystal to obtain an average surface concentration. The sample is heated to a predetermined temperature for a fixed time and then cooled immediately; another Auger scan is made, to obtain  $M(t)$ . The results of these scans are shown in Fig. 36. This procedure is repeated a number of times at different temperatures. Using Eq. (40c) we see that a plot of  $\ln\left[\frac{1}{t}\left(\frac{M_0}{M(t)} - 1\right)\right]$  vs.  $1/T$  should yield a straight line with the slope proportional to the activation energy of desorption and the y-intercept equal to  $C_0 v_2$ . Such a plot is shown in Fig. 37. We find the activation energy of desorption ( $E_{des}$ ) to be  $76.9 \pm 2.9$  kcal/mole and  $C_0 v_2$  to be  $2.28 \times 10^{12}$  molecules ( $\text{cm}^{-2} \text{sec}^{-1}$ ) ( $5.6 \times 10^{11} < C_0 v_2 < 9.3 \times 10^{12}$  molecules ( $\text{cm}^{-2} \text{sec}^{-1}$ )). The method used to determine the errors in  $C_0 v_2$  and  $E_{des}$  is discussed in Appendix C. These values are in good agreement with the values obtained by Tamm and Schmidt [13] who, using flash desorption techniques, found  $E_{des} = 79$  kcal/mole. When the desorption results are plotted as  $\ln\left[\frac{1}{t} \ln(M_0/M)\right]$  vs.  $1/T$  (i.e.  $n=1$ ) the resultant curve has a greater standard deviation associated with it than for the  $n=2$  case. The concentration dependence of the peak desorption temperature  $T_p^{\text{S}}$  in Fig. 30 is also indicative of a second order process. Although our results are far from conclusive, it appears that



AP-875

Figure 36. a) Variation in concentration across nitrogen layer after an exposure of  $10^{-6}$  Torr for 1000 seconds at room temperature  $\square$ . b) Variation in nitrogen concentration after heating (a) to  $1048^{\circ}\text{K}$  for 1000 seconds,  $\Delta$ .

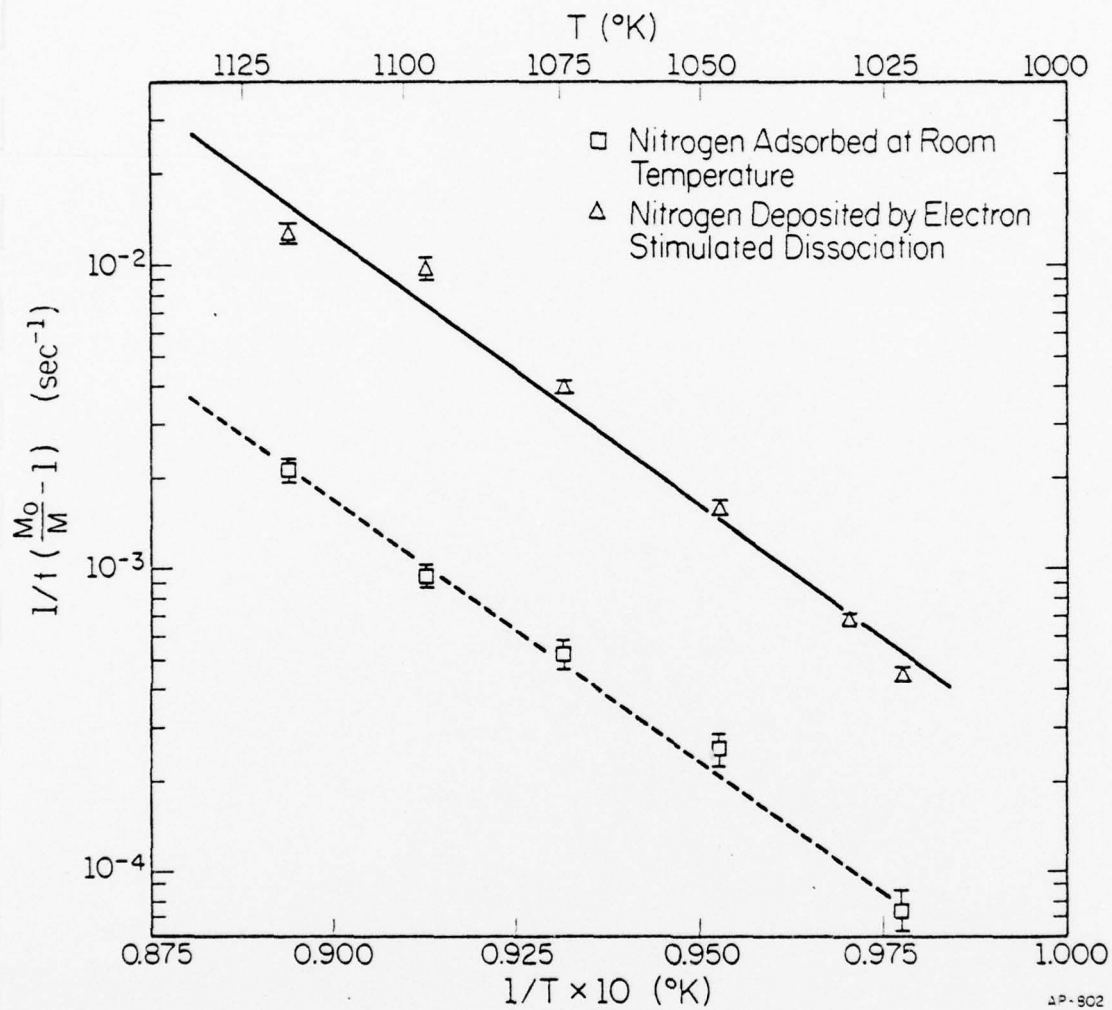


Figure 37. Plot of desorption results in accordance with Eq. 40c.

nitrogen on the (110) plane of tungsten displays second-order desorption kinetics.

### IV.3. Nitrogen Layers Produced by Electron Bombardment

#### IV.3.A. Electron Stimulated Dissociation

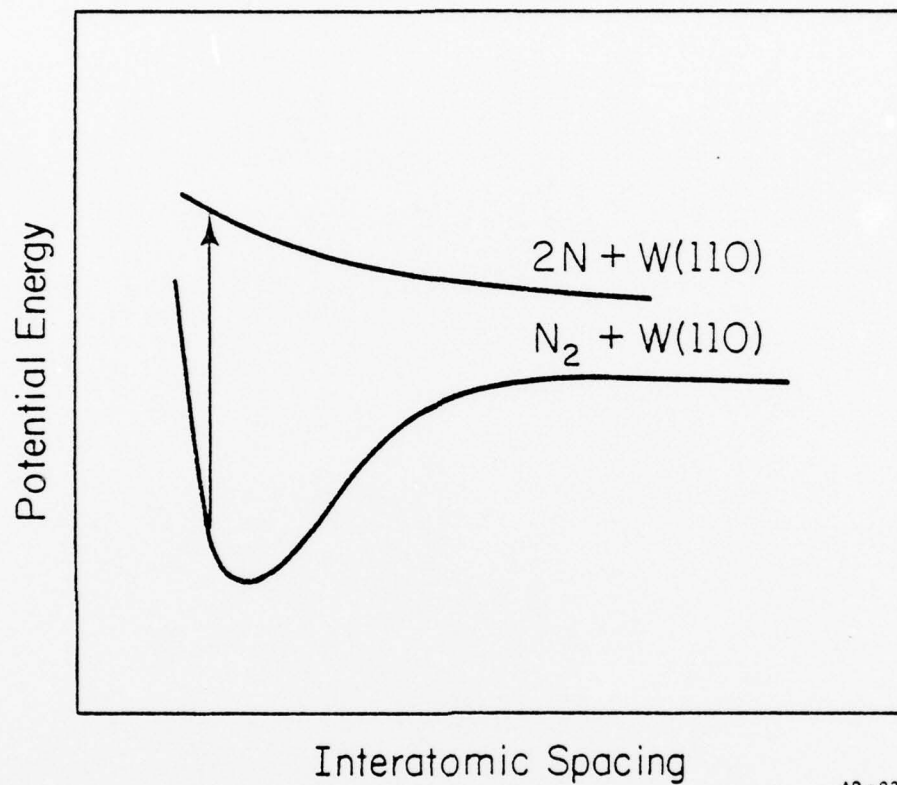
Whenever a surface is probed, be it with electrons, atoms or photons, there is always the possibility that the method of examination will disturb what is being sampled. This has been found to be the case when electrons interact with a number of surface gas layers [37-41]. We actually use the interaction of an electron beam with an adsorbate to overcome one of our basic problems, that of creating a localized deposit of nitrogen on the surface. The interaction of an electron beam with nitrogen bound in the  $\gamma$  state appears to cause dissociation of the molecular nitrogen. A possible mechanism for this dissociation is represented schematically in Fig. 38. Electron impact excites the nitrogen molecule into an anti-bonding state in which it dissociates on the surface. The component atoms then move away from one another and are bound as atoms on the surface. The technique used to create these localized deposits is illustrated in Fig. 39. Initially the sample is cooled to  $95^{\circ}\text{K}$  and exposed to molecular nitrogen. At this temperature the nitrogen is adsorbed in the  $\gamma$  state. The sample is then irradiated with an electron beam, from the glancing incidence Auger gun, at an energy of 2.5 KeV and a current of 100  $\mu\text{A}$  in a beam of 0.1 cm diameter. Dissociation of the molecular nitrogen occurs wherever the electron beam strikes the surface. The crystal is then warmed above  $\approx 120^{\circ}\text{K}$  and the weakly bound  $\gamma$  nitrogen desorbs, leaving only

nitrogen on the (110) plane of tungsten displays second-order desorption kinetics.

### IV.3. Nitrogen Layers Produced by Electron Bombardment

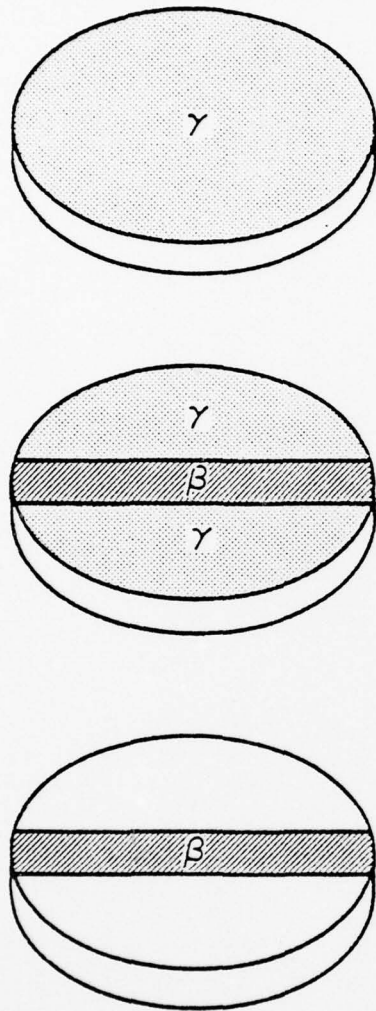
#### IV.3.A. Electron Stimulated Dissociation

Whenever a surface is probed, be it with electrons, atoms or photons, there is always the possibility that the method of examination will disturb what is being sampled. This has been found to be the case when electrons interact with a number of surface gas layers [37-41]. We actually use the interaction of an electron beam with an adsorbate to overcome one of our basic problems, that of creating a localized deposit of nitrogen on the surface. The interaction of an electron beam with nitrogen bound in the  $\gamma$  state appears to cause dissociation of the molecular nitrogen. A possible mechanism for this dissociation is represented schematically in Fig. 38. Electron impact excites the nitrogen molecule into an anti-bonding state in which it dissociates on the surface. The component atoms then move away from one another and are bound as atoms on the surface. The technique used to create these localized deposits is illustrated in Fig. 39. Initially the sample is cooled to  $95^{\circ}\text{K}$  and exposed to molecular nitrogen. At this temperature the nitrogen is adsorbed in the  $\gamma$  state. The sample is then irradiated with an electron beam, from the glancing incidence Auger gun, at an energy of 2.5 KeV and a current of 100  $\mu\text{A}$  in a beam of 0.1 cm diameter. Dissociation of the molecular nitrogen occurs wherever the electron beam strikes the surface. The crystal is then warmed above  $\approx 120^{\circ}\text{K}$  and the weakly bound  $\gamma$  nitrogen desorbs, leaving only



AP-921

Figure 38. Schematic for electron beam dissociation of a nitrogen molecule on the W(110), showing the potential due to N-N interactions vs. interatomic spacing.



AS-726

Figure 39. Operations to form localized deposits. a) Crystal, at 95°K is exposed to nitrogen, forming a layer primarily of  $\gamma$  nitrogen; b) electron irradiation along strip enhances concentration of nitrogen atoms, c) warming to  $T > 120^\circ\text{K}$  removes  $\gamma$  nitrogen, leaving the tightly bound atomic nitrogen.

the more tightly bound atomic nitrogen. A high energy primary beam is not necessary to form these deposits. Using the glancing incidence Auger gun we have formed deposits with beam energies lower than 1 KeV, and by using the LEED electron gun deposits have been formed at 100 volts with 1  $\mu$ A beam current.

It should be kept in mind that this method of creating surface deposits is only practical if two conditions are met. First, the molecular gas must not dissociate spontaneously on the surface (or at worst it must dissociate slowly), and secondly it must have a small cross section for electron stimulated desorption and a high cross section for electron stimulated dissociation.

Fig. 40 shows a secondary electron emission photograph of a line source of atomic nitrogen on the (110) plane, at 95°K. This deposit is created by following the procedure described earlier in this section. Adjacent to the line of atomic nitrogen is the undissociated molecularly bound  $\gamma$  nitrogen. If the crystal is warmed above 120°K, the  $\gamma$  desorbs and all contrast between the line of atomic nitrogen and the surrounding is lost. It should be kept in mind that while this picture is being taken the  $\gamma$  nitrogen is undergoing conversion to the atomically bound state, due to continual irradiation from the Auger gun. Since the emission current necessary to produce this picture is only 10  $\mu$ A and the beam is rastered over a large area, 3-4  $\text{cm}^2$ , the effective current density is sufficiently small that we were unable to detect any  $\gamma$  to  $\beta$  conversion occurring while viewing the sample. We are not restricted to line source as the starting geometry. Fig. 41 shows a point source, approximately 0.1 cm in diameter; also in this picture are the .005" thermocouple wires and the crystal holder. Larger deposits can

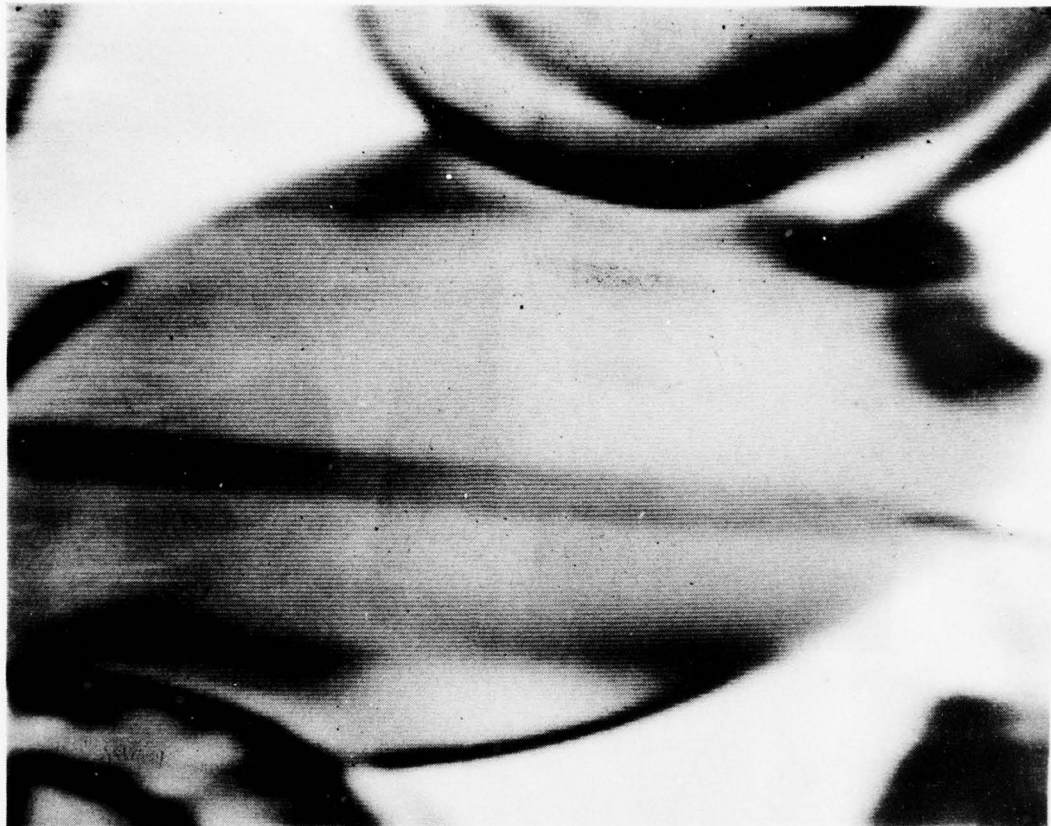


Figure 40. Secondary electron image of a line of atomic nitrogen deposited on the (110) plane of tungsten at  $95^{\circ}\text{K}$ . Primary electron beam current is  $10\ \mu\text{A}$  at 2500 volts. The crystal was not heated to remove the  $\gamma$  nitrogen and the line is surrounded by  $\gamma$  nitrogen.

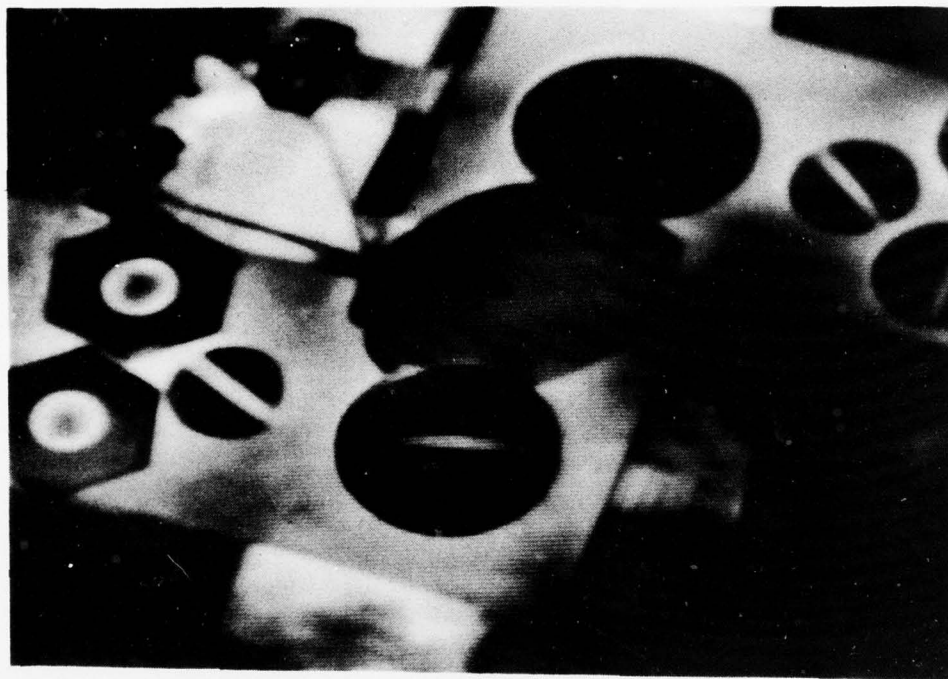


Figure 41. Secondary electron image of a point source ( $\sim .1$  cm in diameter) of atomic nitrogen on the (110) plane. The crystal is cut in an elliptical shape with a minor axis diameter of 0.25".

be created, as shown in Fig. 42, by changing the raster pattern of the Auger gun during the irradiation stage. In the actual experiment once a deposit, such as shown in Fig. 40 and Fig. 42, is created, the temperature is quickly raised to  $\approx 300^{\circ}\text{K}$ . Thermal equilibration takes approximately 2-3 minutes, and leaves a localized surface deposit of atomic nitrogen.

The amount of chemisorbed nitrogen deposited by electron stimulated dissociation can be controlled by one of two methods. The first is by depositing varying amounts of  $\gamma$  nitrogen on the surface (the concentration being less than one monolayer) which is then bombarded to give complete conversion to the atomically bound state. In Sec. IV.2.A. we found that when  $\gamma$  nitrogen is adsorbed on the surface there is some conversion into the atomic  $\beta$  state. At a saturation coverage of  $\gamma$  nitrogen this conversion amounts to  $\approx 0.17$  monolayer. Therefore, by using the method described above, there will always be some  $\beta$  nitrogen on the surface. The concentration of this  $\beta$  layer will be dependent upon the amount of  $\gamma$  nitrogen originally deposited. This method has the advantage that the ratio of atomic nitrogen outside the irradiated area to that within the irradiated region will be minimal,  $\approx 30\%$ .

The other and more reproducible method is to deposit a saturation amount of  $\gamma$  nitrogen and then control the current density to the  $\gamma$  layer; this then controls the total amount of nitrogen dissociated by controlling the number of electrons which strike the surface. The second method is the one we used in forming our localized deposits. Its major drawback is that the amount of atomic nitrogen outside the irradiated area will always be determined by the original amount of  $\gamma$  deposited, irrespective

AD-A056 346

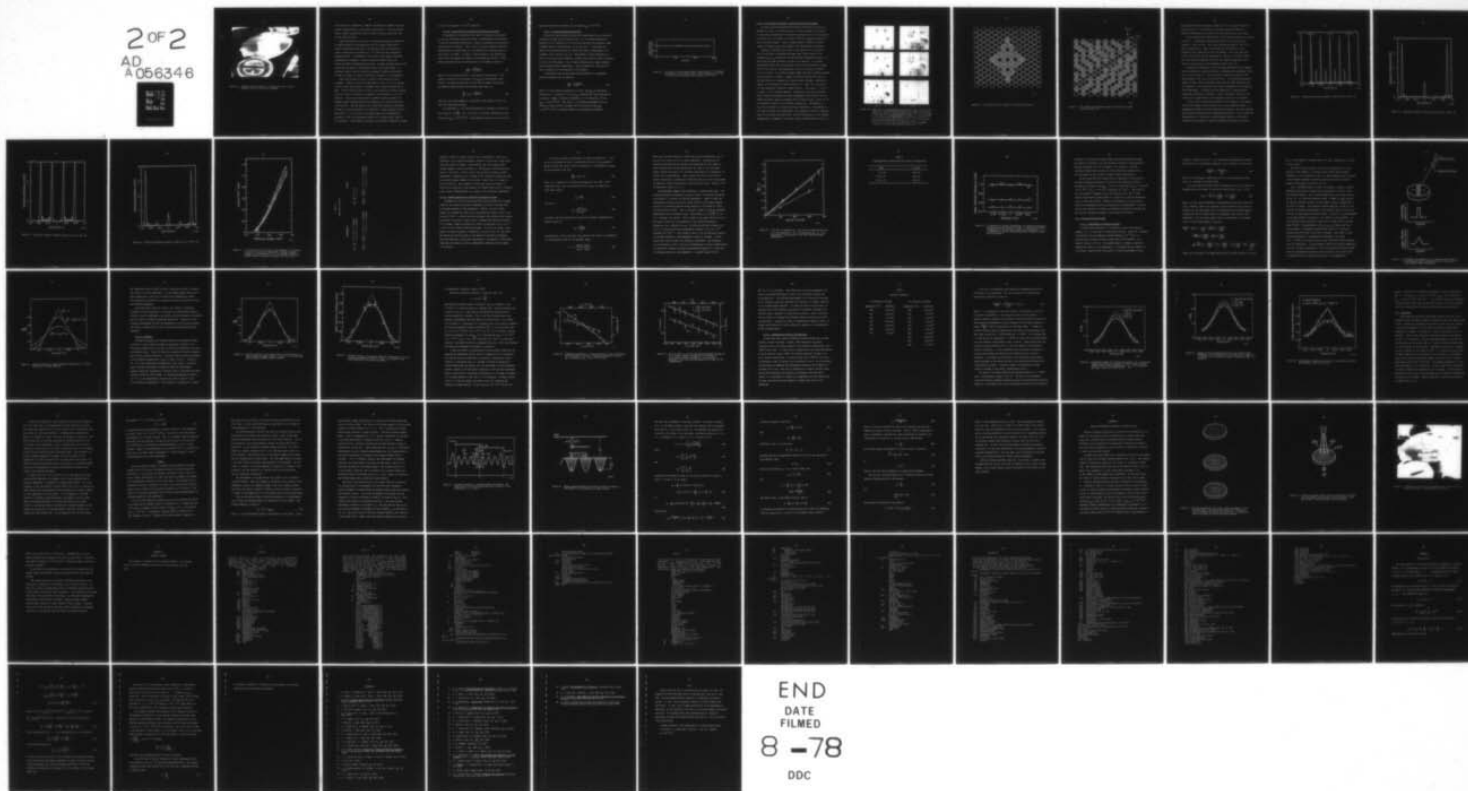
ILLINOIS UNIV AT URBANA-CHAMPAIGN COORDINATED SCIENCE LAB F/8 7/4  
DESORPTION AND SURFACE DIFFUSION: NITROGEN ON TUNGSTEN (110). (U)  
OCT 77 A J POLAK  
R-789

UNCLASSIFIED

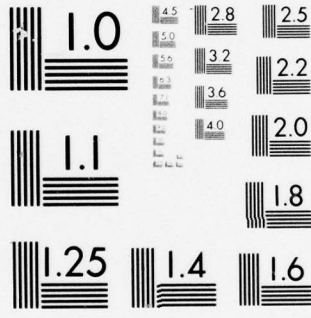
DAAB07-72-C-0259

NL

2 of 2  
AD  
A056346



END  
DATE  
FILMED  
8 -78  
DDC



MICROCOPY RESOLUTION TEST CHART  
NATIONAL BUREAU OF STANDARDS-1963-A



Figure 42. Secondary electron image of a rectangle of atomic nitrogen deposited on the (110) plane of tungsten.

of the amount of irradiation. However, this method is capable of giving greater reproducibility in the deposit concentration. The only drawback being a higher concentration ratio of atomic nitrogen outside the line to the inside the line.

Auger spectroscopy is also used to compare the surface coverage for nitrogen adsorbed at room temperature and for nitrogen deposited by electron stimulated dissociation. The maximum surface concentration of atomic nitrogen after irradiation is  $\approx 2.2$  times the room temperature saturation value. To determine if this truly is the maximum attainable concentration, we deposit a square of atomic nitrogen, redose the crystal and again irradiated the same area. An Auger spectrum taken of the irradiated area shows no noticeable increase in the Auger signal. It therefore appears that the saturation coverage of electron dissociated nitrogen is indeed 2.2 times the saturation coverage at room temperature.

Auger spectroscopy by itself is unable to give absolute surface coverages. However, by using the LEED results of Sec. IV.2.B. in conjunction with Auger spectroscopy, an estimate of the surface coverage can be made. From the structure shown in Fig. 19 we estimate the surface coverage after the crystal is exposed to nitrogen at room temperature to be 0.25 monolayer. Since we are dealing with a number of surface islands, the average surface coverage would then be expected to be slightly less than 0.25 monolayer. Tamm and Schmidt [13], using flash desorption techniques, estimated a surface coverage of 0.21 monolayer, in good agreement with our LEED results. We can now use the nitrogen Auger peak corresponding to saturation of the room temperature crystal as a reference mark, equal to 0.25 monolayer. The saturation coverage of the electron irradiated nitrogen

is thus 0.55 monolayer ( $7.7 \times 10^{14}$  atoms/cm<sup>2</sup>).

#### IV.3.B. Cross Section for Electron Stimulated Dissociation

A knowledge of the efficiency with which  $\gamma$  nitrogen is dissociated by electron irradiation should be helpful in understanding the mechanism of electron stimulated dissociation. However, estimating the dissociation cross section is difficult. This is due to the many secondary electrons emitted from the surface which can, and probably do, dissociate some of the surface  $\gamma$  nitrogen. To obtain a crude estimate of the dissociation cross section we neglect the effect of the secondaries entirely. Under these conditions the rate of dissociation of  $\gamma$  nitrogen is given by

$$-\frac{dM'}{dt} = \frac{j_e M' Q_{\text{diss}}}{e}, \quad (41)$$

where  $j_e$  is the current density,  $e$  the charge of the electron,  $M'$  the number of molecules on the surface, and  $Q_{\text{diss}}$  the dissociation cross section. Solving this equation, we find that the number of molecules  $M'_u$  remaining undissociated on the surface after time  $t$  is

$$\frac{M'_u}{M_0} = \exp\left[-\frac{j_e Q_{\text{diss}} t}{e}\right], \quad (42)$$

where  $M_0$  is the total number of  $\gamma$  molecules on the surface at time  $t = 0$  that can undergo dissociation.

On irradiating a  $.1 \text{ cm}^2$  area saturated with  $\gamma$  nitrogen at 100  $\mu\text{A}$  for 100 seconds we find  $\frac{M'_u}{M_0} = 0.25$ . Use of Eq. (42) gives a dissociation cross section of  $Q_{\text{diss}} \approx 3 \times 10^{-18} \text{ cm}^2$ . This compares quite well with the work of

Madey and Yates [38] and Emrich [41] who found  $Q_{des} \approx 10^{-19} \text{ cm}^2$ .

#### IV.3.C. Electron Stimulated Desorption

During both the diffusion and desorption measurements we are constantly probing the surface with an electron beam. It is therefore important to determine if the interaction of the electron beam with the atomically bound nitrogen results in the desorption of the gas layer. To determine the effect of an electron beam on the adlayer we create a large deposit of  $\beta$  nitrogen, such as shown in Fig. 42. This deposit is then irradiated, at a point in the center after warming to  $\approx 300^\circ\text{K}$ , with a 2500 eV beam of electrons at 150  $\mu\text{A}$  for 100 minutes. Fig. 43 shows the variation in Auger intensity after extended electron bombardment. After 100 minutes of irradiation we find no change in the concentration of the adlayer.

If adsorption from the gas phase during irradiation is negligible, then the desorption rate is given by

$$-\frac{dM'}{dt} = \frac{j_e Q_{des} M'}{e}, \quad (43)$$

where  $M'$  is the surface concentration at time  $t$  and  $Q_{des}$  the desorption cross section. Solving Eq. (43) for  $Q_{des}$  (assuming that Auger spectroscopy can detect a change in surface concentration of .01 monolayer) we find  $Q_{des} < 1.4 \times 10^{-23} \text{ cm}^2$ . This result is in reasonable agreement with the results of Emrich [35,41] and Madey and Yates [38] who found  $Q_{des} < 5 \times 10^{-24} \text{ cm}^2$  for  $\beta$  nitrogen adsorbed on polycrystalline tungsten.

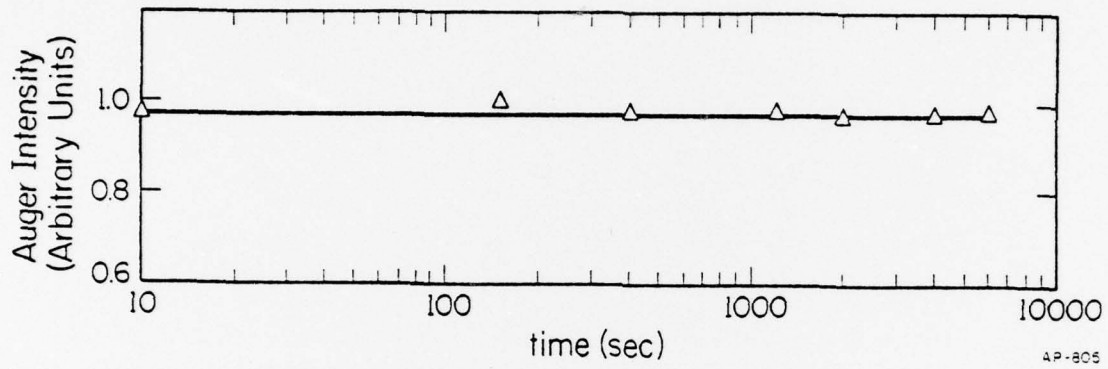


Figure 43. Variation in the nitrogen surface concentration of  $\beta$  nitrogen, as measured by Auger spectroscopy, after irradiation for time  $t$  at 150  $\mu$ A with a primary beam voltage of 2500 volts.

#### IV.3.D. Work Function and LEED of Electron Dissociated Nitrogen

By using electron stimulated dissociation we are able to follow the changes that occur in the LEED pattern of a clean tungsten (110) surface as the surface concentration of nitrogen increases from 0 to 0.55 monolayer. To achieve this, the crystal is cooled to 95°K and electron irradiated to form a localized deposit. After a thermal anneal to 800°K for several seconds, a change in the clean tungsten (110) LEED pattern is observed.

Heating to 800°K does not result in the desorption of  $\beta$  nitrogen. This is determined by comparing the Auger peak-to-peak height of the nitrogen  $KL_{2,3}L_{2,3}$  transition, before and after the sample is heated. In both cases the Auger intensity is found to be identical. For surface concentrations less than 0.25 monolayer, which is the saturation coverage of the (110) plane at room temperature, the  $p(2 \times 2)$  pattern of Section IV.2.B. is found. For surface coverages higher than this, another structure, called structure A, appears. Figure 44 shows the changes that occur in the LEED pattern for progressively higher surface coverages. Heating the crystal is not necessary to develop structure A. After 15 to 20 minutes at room temperature, structure A became visible. Very rarely,  $\approx 1$  out of 15 times, a  $(2 \times 4)$  pattern appeared. Although we do not have sufficient data to uniquely determine the atomic arrangement within the unit cell of either structure, possible repeating units are shown in Fig. 45 and Fig. 46 for structure A and the  $(2 \times 4)$  pattern, respectively. The domains in Fig. 46 are related by a rotation and not a translation. Such domains do not cause splitting of any LEED beams. Only domains of the same rotational type will interfere with each other. We have verified this by the computer program given in Appendix B, using the surface structure shown in Fig. 46.

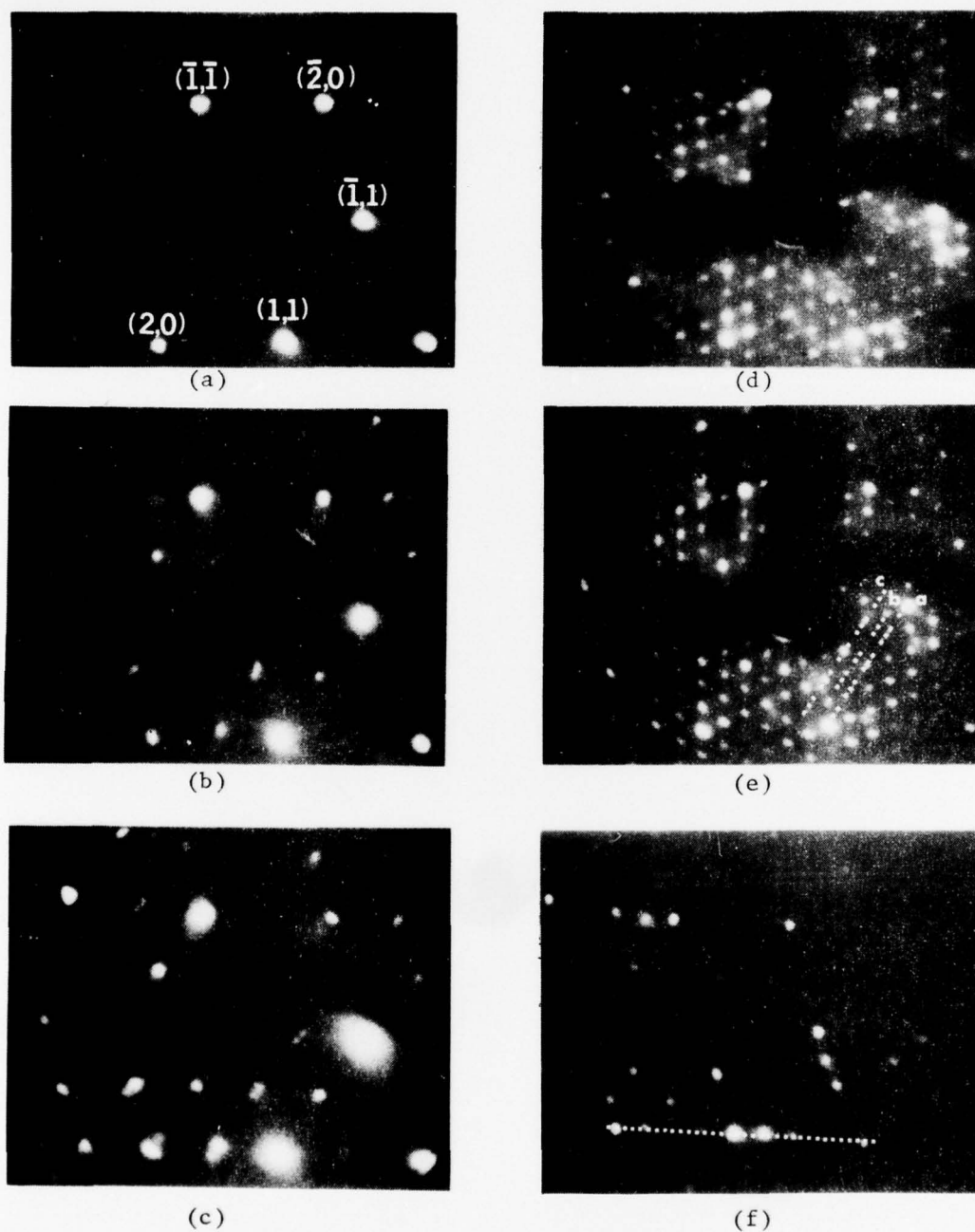
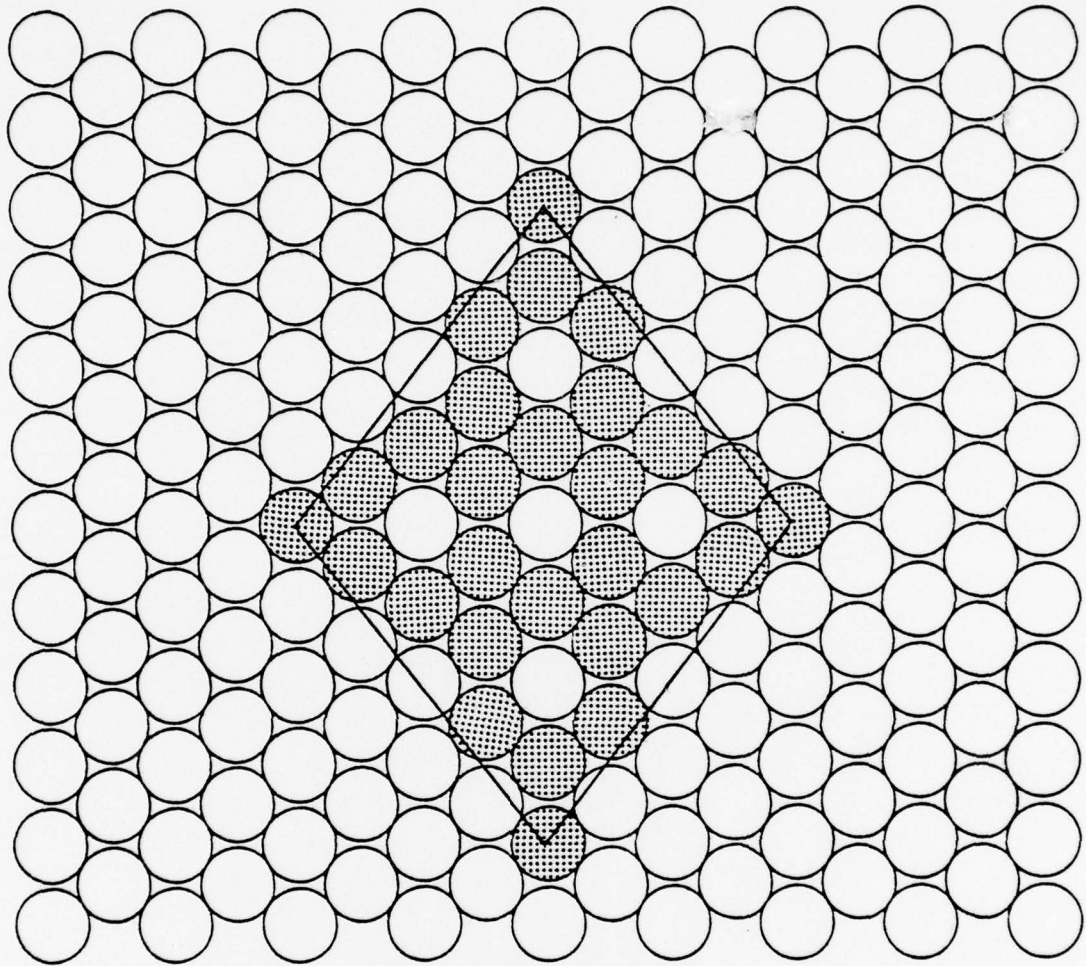
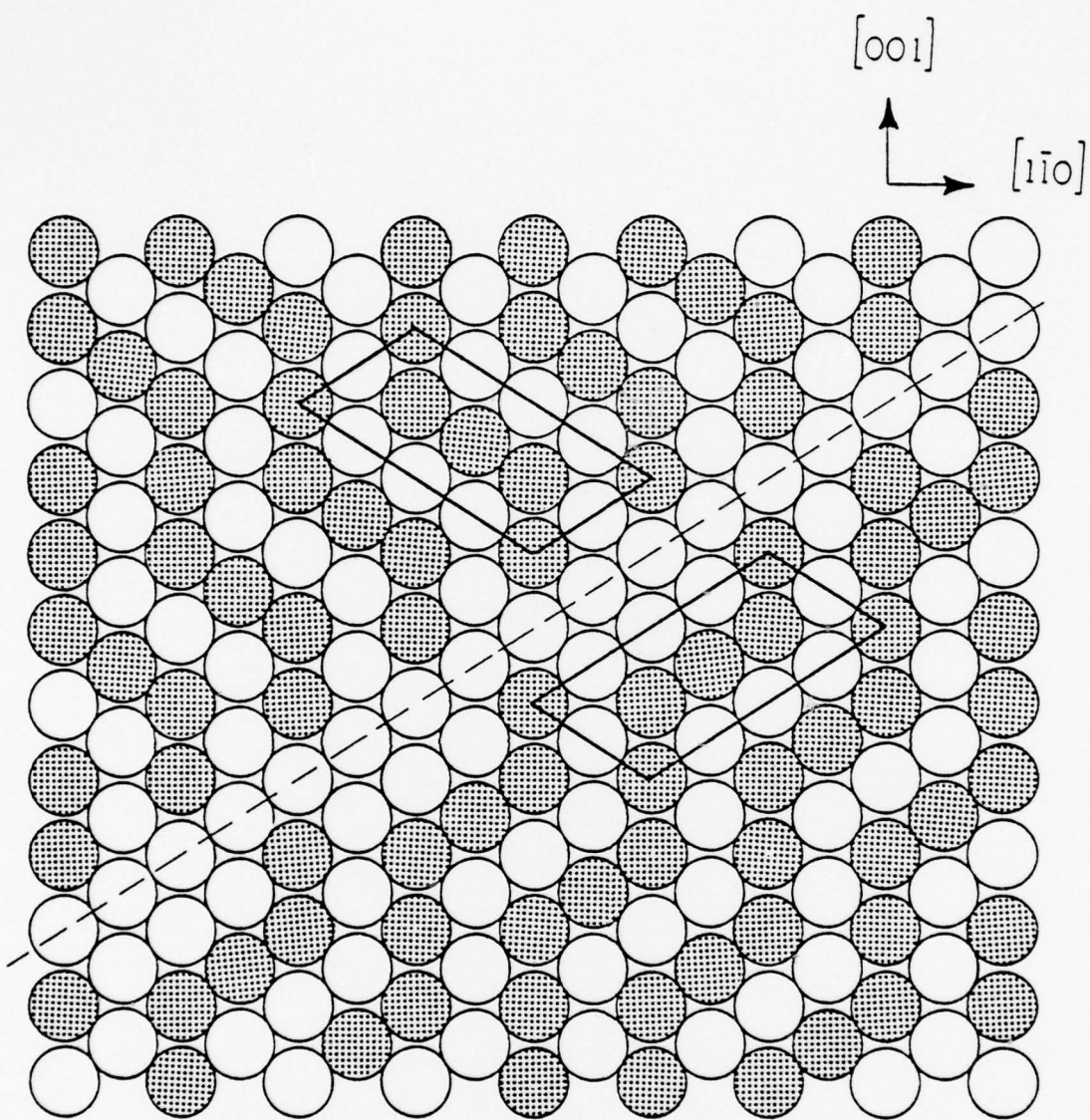


Figure 44. Changes in the LEED pattern of an initially clean tungsten (110) plane after deposition of an adlayer of  $\beta$  nitrogen, followed by increasing periods of electron irradiation. With the exception of Fig. 36d, the crystal was heated to 800°K for several seconds to fully develop the LEED pattern. Structure A is shown in d and e, along with the  $p(2 \times 4)$  in b and c. The surface concentrations in monolayers are a) clean, b)  $\approx 0.14$ , c)  $\approx 0.25$ , d)  $\approx 0.55$ , e)  $\approx 0.55$ , f) a  $(2 \times 4)$  pattern seen occasionally in place of d and e, with a surface coverage of  $\approx 0.55$ .



AP-863

Figure 45. A possible unit cell capable of producing structure A.



AP-963

Figure 46. Two rotated (2x4) domains capable of producing the LEED pattern of Fig. 44f.

The resultant intensity pattern is shown in Fig. 47, along the direction shown in Fig. 44f. We find that no splitting results and that the resultant LEED pattern is the sum of the LEED patterns from each domain.

We also calculate the LEED pattern for the surface structure illustrated in Fig. 45. The patterns along three directions in reciprocal space, labeled a, b and c in Fig. 44e, are calculated and shown in Figs. 48, 49 and 50, respectively. These calculations were performed for a two-dimensional grid consisting of over 700 adatoms. All of the LEED beams of Fig. 44e and Fig. 44f are accounted for. However, it should be noted that the computed intensities vary over two orders of magnitude, which surely is not the case in the experiments shown in Fig. 44e.

The relative intensities of the calculated LEED beams can be changed, while maintaining the same LEED pattern, by changing the arrangement within the unit cell of Fig. 45. Let us use the 4 atoms in the corner of the parallelogram in Fig. 45 as our new unit cell. A calculated LEED pattern similar to Figs. 48-50 is obtained, except that all LEED intensities are now identical. Our calculations only provide information on the positions of the LEED beams. To account for the intensities, a proper multiple scattering calculation is necessary. Table 3 provides a listing of the location of all LEED beams in both Structure A and the (2 x 4) pattern.

In Sec. IV2.B. we found the adsorption of  $\beta$  nitrogen at room temperature did not change the work function of the clean tungsten surface. To determine the effect of electron dissociated nitrogen on the clean tungsten work function we again use the retarding diode analyzer. Fig. 51 shows the characteristic I-V curves for a clean tungsten surface, for a surface saturated with nitrogen by electron stimulated dissociation, and after

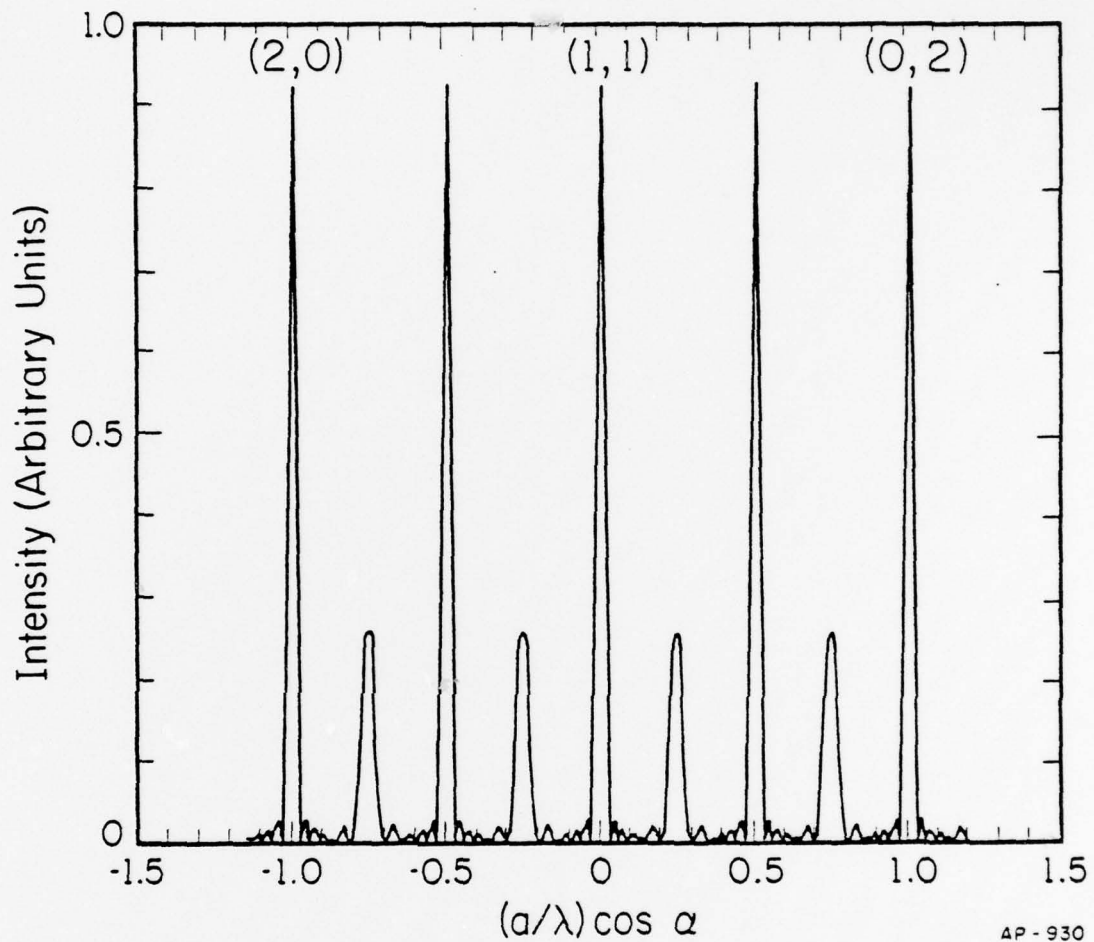


Figure 47. Calculated scattered intensity along the line of Fig. 44f.

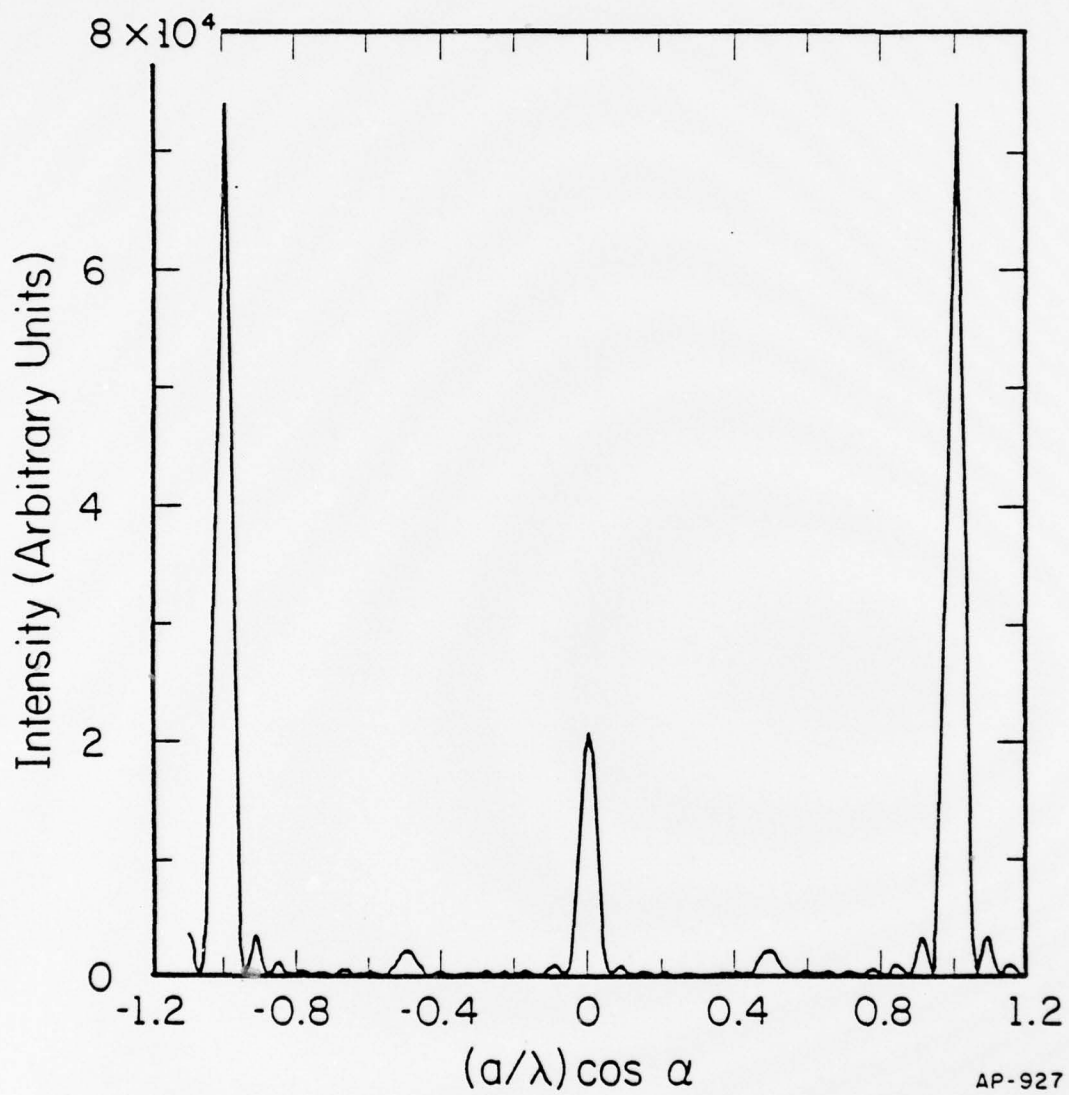
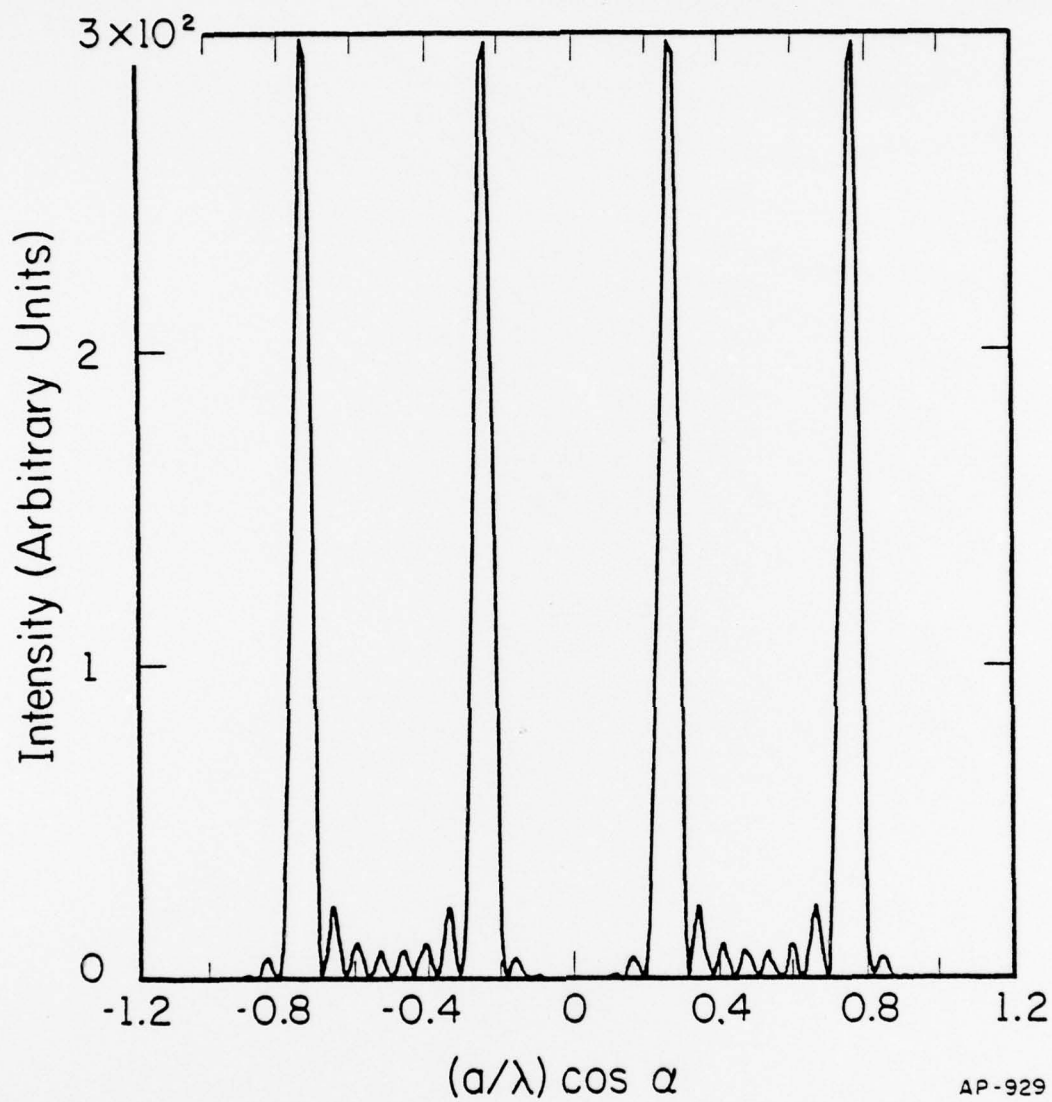


Figure 48. Calculated scattered intensity along line (a) of Fig. 44e.



AP-929

Figure 49. Calculated scattered intensity along line (b) of Fig. 44e.

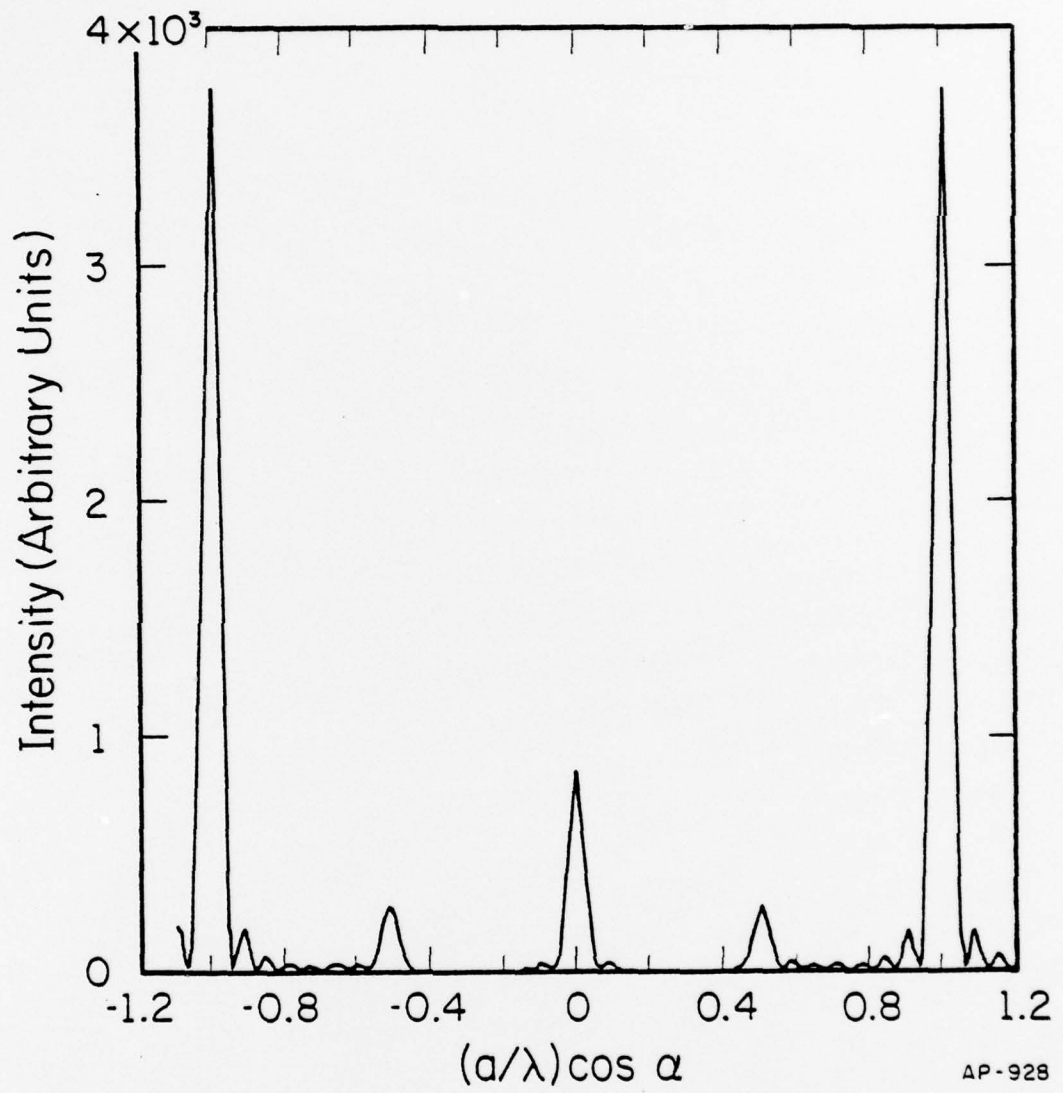
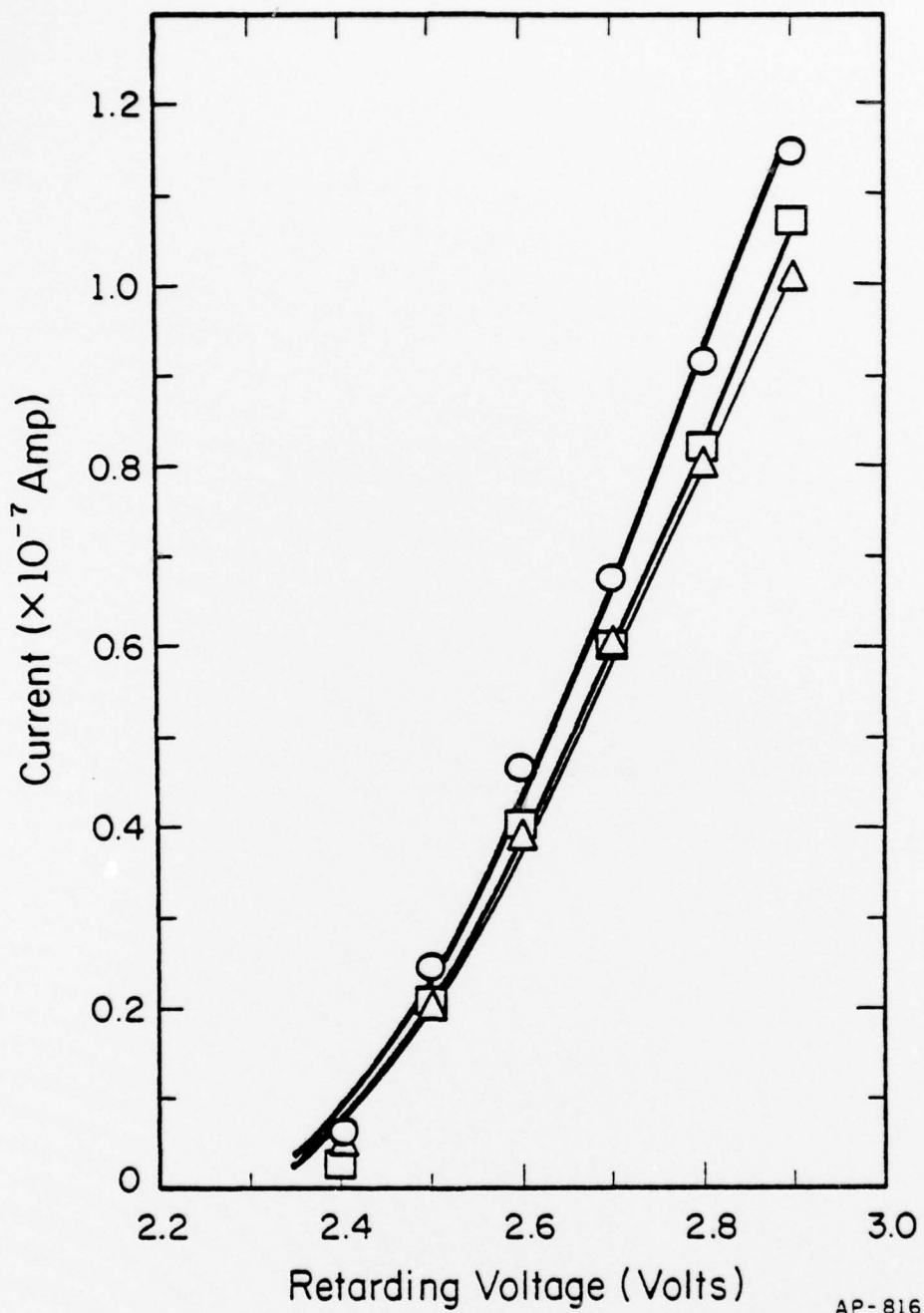


Figure 50. Calculated scattered intensity along line (c) of Fig. 44e.



AP-816

Figure 51. I-V curves for a) an initially clean tungsten (110) surface b) the (110) plane with a saturation coverage of atomic nitrogen  $\approx 0.55$  monolayer  $\square$ ; c) (b) flashed to  $800^\circ\text{K}$  for several seconds, structure A visible after the flash, 0.

Table 3

LEED Beam Location

Structure A

(2 x 4)

$$\left(\frac{1}{2}, \frac{j}{2}\right) \quad -2 \leq i \leq 2 \quad i = \text{integer}$$

$$-4 \leq j \leq 4 \quad j = \text{integer}$$

$$\left(\frac{1}{2}, \frac{j}{2}\right) \quad i = -1, 1$$

$$j = -1, 1$$

$$\left(\frac{2n+1}{4}, \frac{2m+1}{8}\right) \quad -2 \leq n \leq 1 \quad n = \text{integer}$$

$$-4 \leq m \leq 3 \quad m = \text{integer}$$

$$\left(\frac{2n+1}{4}, \frac{2m+1}{8}\right) \quad -2 \leq n \leq 1 \quad n = \text{integer}$$

$$-2 \leq m \leq 1 \quad m = \text{integer}$$

heating to  $800^{\circ}\text{K}$  for several seconds, also at saturation. There is no difference in the clean and nitrogen covered I-V curves and a slight shift after the crystal is heated. After heating, the clean tungsten LEED pattern changes to that of structure A. The change in work function that occurs is less than  $- .027$  eV, and in fact the shift revealed in these experiments is probably due to a change in the reflection coefficient after the nitrogen becomes ordered on the surface, rather than to a change in the work function. This appears to be the case since the various I-V curves are not parallel to one another, but instead seem to have a different slope, which is characteristic of a change in the reflection coefficient.

#### IV.3.E. Thermal Desorption of Electron Dissociated Nitrogen

Throughout the earlier sections we have tacitly assumed that nitrogen formed on the surface by electron bombardment is bound in the same state as nitrogen adsorbed at room temperature. However, on other crystal planes, for instance the (100) and on polycrystalline samples, this is not the case [37,39]. To verify that the nitrogen on the surface after electron irradiation is actually in the  $\beta$  state, we compare the desorption kinetics of  $\beta$  nitrogen, formed by adsorption at  $300^{\circ}\text{K}$ , as described in Sec. IV.2.C., to that of the electron irradiated nitrogen. To do this we create a large deposit of atomic nitrogen by irradiation, as shown in Fig. 42, and follow the desorption from the center of the deposit as a function of heating time and temperature, using Auger spectroscopy. The deposit is sufficiently large that the central portion is unaffected by diffusion from the edges of the deposit.

It is first necessary to determine the order of desorption,  $n$ . This can be done knowing the initial concentration and the time  $t_{\frac{1}{2}}$  needed to desorb one-half the initial surface concentration. The desorption process can be expressed in the form

$$\frac{dM}{dt} = k(M_0 - M)^n, \quad (44)$$

where  $k$  is a constant,  $M$  the surface coverage and  $n$  the order. Upon integration of Eq. (44) and substitution of  $M = M_0/2$ , we obtain for a first order process

$$t_{\frac{1}{2}} = \frac{\ln 2}{k}, \quad (45)$$

and for  $n \neq 1$

$$t_{\frac{1}{2}} = \frac{(2^{n-1} - 1)}{k(n-1)M_0^{n-1}}. \quad (46)$$

In general, the time required for one half the original concentration to desorb is given by

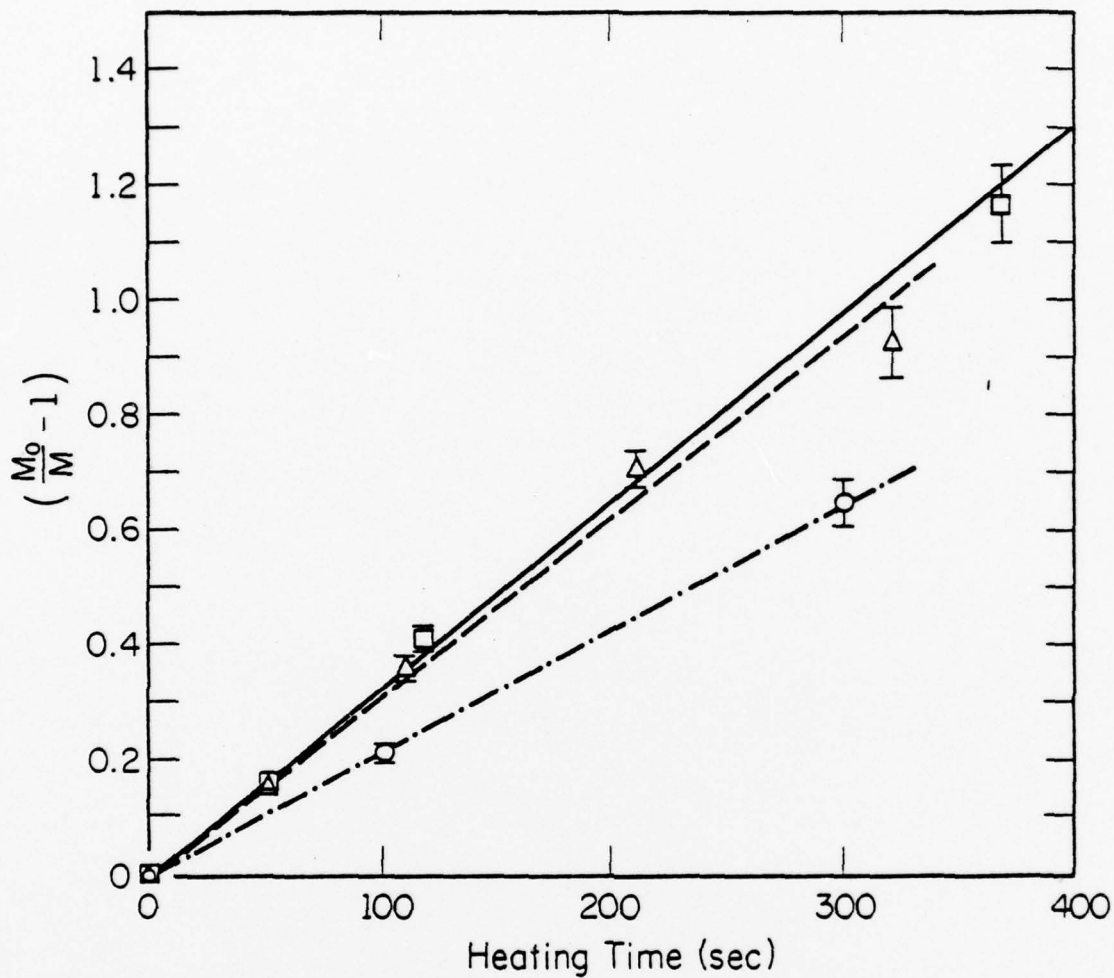
$$t_{\frac{1}{2}} = \frac{f(n,k)}{M_0^{n-1}}. \quad (47)$$

By applying Eq. (46) to two pairs of  $t_{\frac{1}{2}}$  and  $M(t)$  data points, an expression for the desorption order can be obtained, namely

$$n = 1 + \frac{\log t_{\frac{1}{2}}' - \log t_{\frac{1}{2}}}{\log M_0 - \log M_0'}, \quad (48)$$

where  $t_{\frac{1}{2}}'$  is the time required to reduce the surface concentration,  $M_0'$ , to one half its initial value at a fixed temperature. By depositing two different concentrations ( $M_0$  and  $M_0'$ ) and determining the time needed to remove one-half the initial concentration the order can be calculated. Figure 52 shows the results of 3 different experiments at a temperature of  $1072^\circ\text{K}$ , used to determine  $t_{\frac{1}{2}}'$ . Table 4 gives the values of the initial surface concentration (normalized as described earlier) and the time needed to reduce the surface concentration to  $\frac{1}{2}$  its initial value. Using Eq. (48) the desorption order is  $2.2 \pm .1$ .

The measurement suggests that desorption is indeed second order. The activation energy for desorption can now be found, by following the desorption process as a function of time and temperature. Figure 53 shows the concentration variation across the central portion of the square deposit, initially at saturation and then after heating for 300 seconds at  $1048^\circ\text{K}$  and 100 seconds at  $1095^\circ\text{K}$ . This is repeated a number of times at different temperatures and for different times. When plotted as  $\ln\left[\frac{1}{2}\left(\frac{M_0}{M} - 1\right)\right]$  vs.  $1/T$ , a straight line results. This is shown in the upper portion of Fig. 37. The slope of this line is proportional to the activation energy of desorption, the y intercept to  $C_0 v_2$ . We find the activation energy to be  $79.2 \pm 5.1$  kcal/mole and the pre-exponential constant to be  $4.63 \times 10^{13}$  molecules ( $\text{cm}^{-2} \text{sec}^{-1}$ ). Also plotted in Fig. 37 are the desorption results for nitrogen adsorbed at room temperature, regular  $\beta$  nitrogen. The two curves have similar slopes, but differeny y-intercepts. The difference in the intercepts is due in part to the differences in initial concentrations. The saturation coverage of electron dissociated nitrogen is 2.2 times that of nitrogen adsorbed at room temperature. A possible reason for the



AP-828

Figure 52. Plot used to determine  $t_{\frac{1}{2}}$ . The initial concentrations were, a)  $\approx 0.55$  monolayer  $\Delta$ , b)  $\approx 0.52$  monolayer  $\square$ , c)  $\approx 0.41$  monolayer  $\circ$ , with  $t_{\frac{1}{2}}$  equal to 316, 302, and 458 seconds respectively.

Table 4

Time Necessary to Desorb Half the Initial Concentration

$M/M_0$	$t_{1/2}$ (sec)
$1 \pm .07$	$316 \pm 16$
$0.95 \pm .07$	$302 \pm 22$
$0.74 \pm .14$	$458 \pm 14$

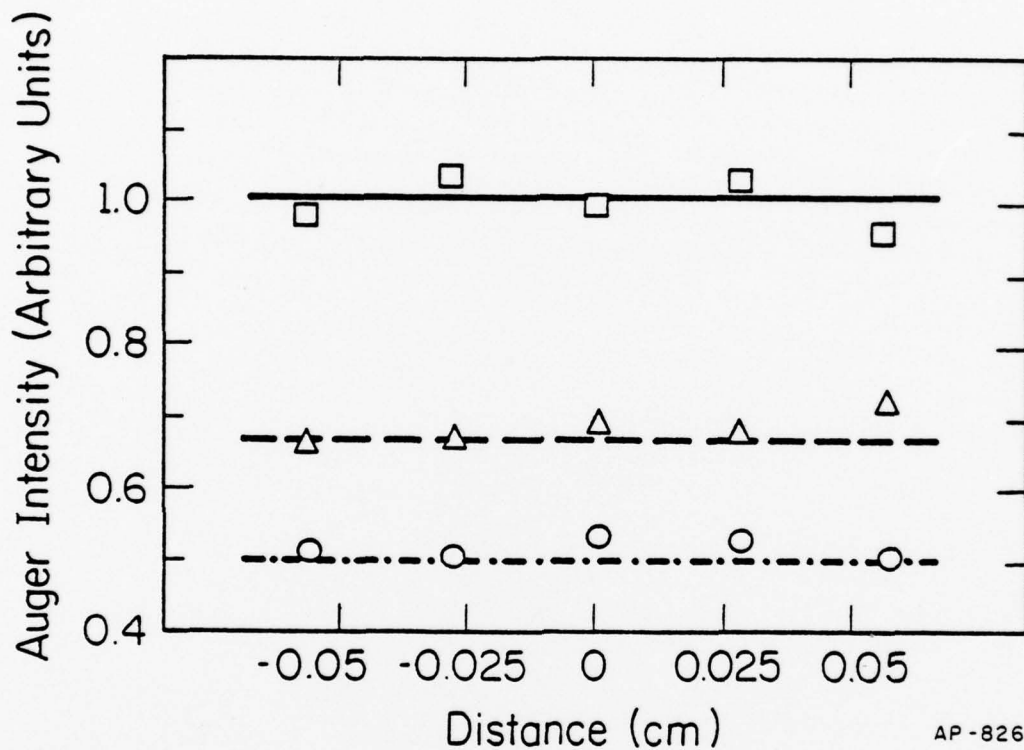


Figure 53. a) Variation in surface concentration of electron dissociated nitrogen across the crystal face  $\square$ . b) Variation in surface concentration after heating to 1048°K for 300 seconds  $\Delta$ . c) Variation in surface concentration after heating to 1095°K for 100 seconds  $\circ$ .

difference in saturation coverage between electron dissociated nitrogen and regular  $\beta$  nitrogen is that the adsorption process at room temperature becomes exceedingly slow for coverages  $> 0.25$  monolayer. Electron stimulated dissociation replaces the normal adsorption mechanism with a more efficient one and we obtain a higher surface concentration.

We have found that the nitrogen which is deposited on the surface by electron stimulated dissociation follows the same desorption kinetics as regular  $\beta$  nitrogen, with  $E_{\text{des}} = 79.2 \pm 5.1$  kcal/mole and  $C_0 v_2 = 4.63 \times 10^{13}$  ( $4.14 \times 10^{12} < C_0 v_2 < 5.19 \times 10^{14}$ ) molecules ( $\text{cm}^{-2} \text{sec}^{-1}$ ). The values of  $C_0 v_2$  for regular  $\beta$  nitrogen ( $2.28 \times 10^{12}$  molecules ( $\text{cm}^{-2} \text{sec}^{-1}$ )) and electron dissociated nitrogen differ by a factor of 9, when the difference in  $C_0$  is taken into account. However, the differences in  $C_0 v_2$  are well within the experimental errors associated with each measurement. From this and the fact that the I-V curves are essentially the same we conclude that the electron irradiated nitrogen is also bound in the  $\beta$  state.

#### IV.4. Surface Diffusion Studies

##### IV.4.A. Measurement of Diffusion Profiles

To study surface diffusion, a line source is used as the starting geometry, as it is both easy to create and to analyze. After the  $\gamma$  nitrogen is deposited, and the background pressure reduced to  $10^{-10}$  Torr, an electron beam is swept across the crystal face for 300 seconds, at an emission current of 100  $\mu\text{A}$ . The nondissociated  $\gamma$  nitrogen is removed by warming the crystal to room temperature. A secondary electron image of a line source, produced after 300 seconds of electron bombardment of the  $\gamma$

nitrogen, is shown in Fig. 40. For a concentration independent diffusion coefficient and a concentration gradient in the x direction, we know that

$$\frac{dC(x,t)}{dt} = D \frac{d^2C(x,t)}{dx^2}, \quad (49)$$

where D is the diffusion coefficient and C(x,t) the concentration after time t at a distance x from the origin.

For a line source of width 2h the concentration C(x,t) at a distance x perpendicular to the center of the initial deposit after time t is [43]

$$C(x,t) = \frac{C_0}{2} \left\{ \operatorname{erf} \left( \frac{h+x}{2\sqrt{Dt}} \right) + \operatorname{erf} \left( \frac{h-x}{2\sqrt{Dt}} \right) \right\}, \quad (50)$$

where  $C_0$  is the initial difference in concentration inside and outside the strip. However, since we are sampling a line of width 2h with a beam of diameter 2h, the Auger signal must be intergrated over the beam dimension. Assuming the beam is uniform and has a rectangular cross section, with dimensions b x 2h, the Auger signal, which is proportional to the number M(x,t) of atoms being sampled, is given by

$$\begin{aligned} \frac{M(x,t)}{M_0} &= \frac{x}{4h} \operatorname{erf} \left( -\frac{x}{2\sqrt{Dt}} \right) + \left( \frac{2h-x}{4h} \right) \operatorname{erf} \left( \frac{2h-x}{2\sqrt{Dt}} \right) \\ &+ \left( \frac{2h+x}{4h} \right) \operatorname{erf} \left( \frac{2h+x}{2\sqrt{Dt}} \right) - \left( \frac{x}{4h} \right) \operatorname{erf} \left( \frac{x}{2\sqrt{Dt}} \right) \\ &+ \frac{1}{2h} \sqrt{\frac{Dt}{\pi}} \left[ \operatorname{erf} \left( -\frac{2h+x}{2\sqrt{Dt}} \right)^2 + \operatorname{erf} \left( -\frac{2h-x}{2\sqrt{Dt}} \right)^2 - \exp \left( -\frac{x}{2\sqrt{Dt}} \right) - \exp \left( -\frac{x}{2\sqrt{Dt}} \right) \right], \end{aligned} \quad (51)$$

where  $M_0$  is the number of nitrogen atoms initially within an area b x 2h, and

$M(x,t)$  is the number of nitrogen atoms in an area, centered at  $x$ , of size  $b \times 2h$  at time  $t$ .

Thus for an initial deposit in which the concentration is a step function of the distance  $x$ , the Auger signal should actually appear triangular, as is illustrated in Fig. 54. When diffusion occurs, the base of the triangle increases as material diffuses away from the initial deposit at the origin, as shown in Fig. 55.

Once a localized deposit (a line) of nitrogen is formed by electron stimulated dissociation, scanning Auger spectroscopy is used to follow the diffusion process. This is shown schematically in the lower portion of Fig. 54. To follow the diffusion process, a number of Auger spectra are taken at discrete locations on the crystal surface, perpendicular to the line of nitrogen. The glancing incidence Auger gun, of Fig. 54, can position the electron beam anywhere on the crystal surface by the use of two sets of electrostatic deflection plates. Typically a 2 mm displacement in the beam position is caused by 5 volt change in plate potential. At each discrete surface position an Auger scan is taken within the energy range 370-390 V, corresponding to the  $K L_{2,3} L_{2,3}$  nitrogen transition. In this manner, an integrated concentration profile as a function of distance from the center of the line is obtained. The crystal is then resistively heated to a predetermined temperature in the range  $800 < T < 900^\circ K$ , for a fixed period of time (1000-3500 seconds depending upon the temperature). The time needed to reach the diffusion temperature is about 5 seconds, and amounts to .5% of the shortest diffusion interval. After the predetermined diffusion time has elapsed, the crystal heater is turned off and the crystal quickly cools to room temperature.

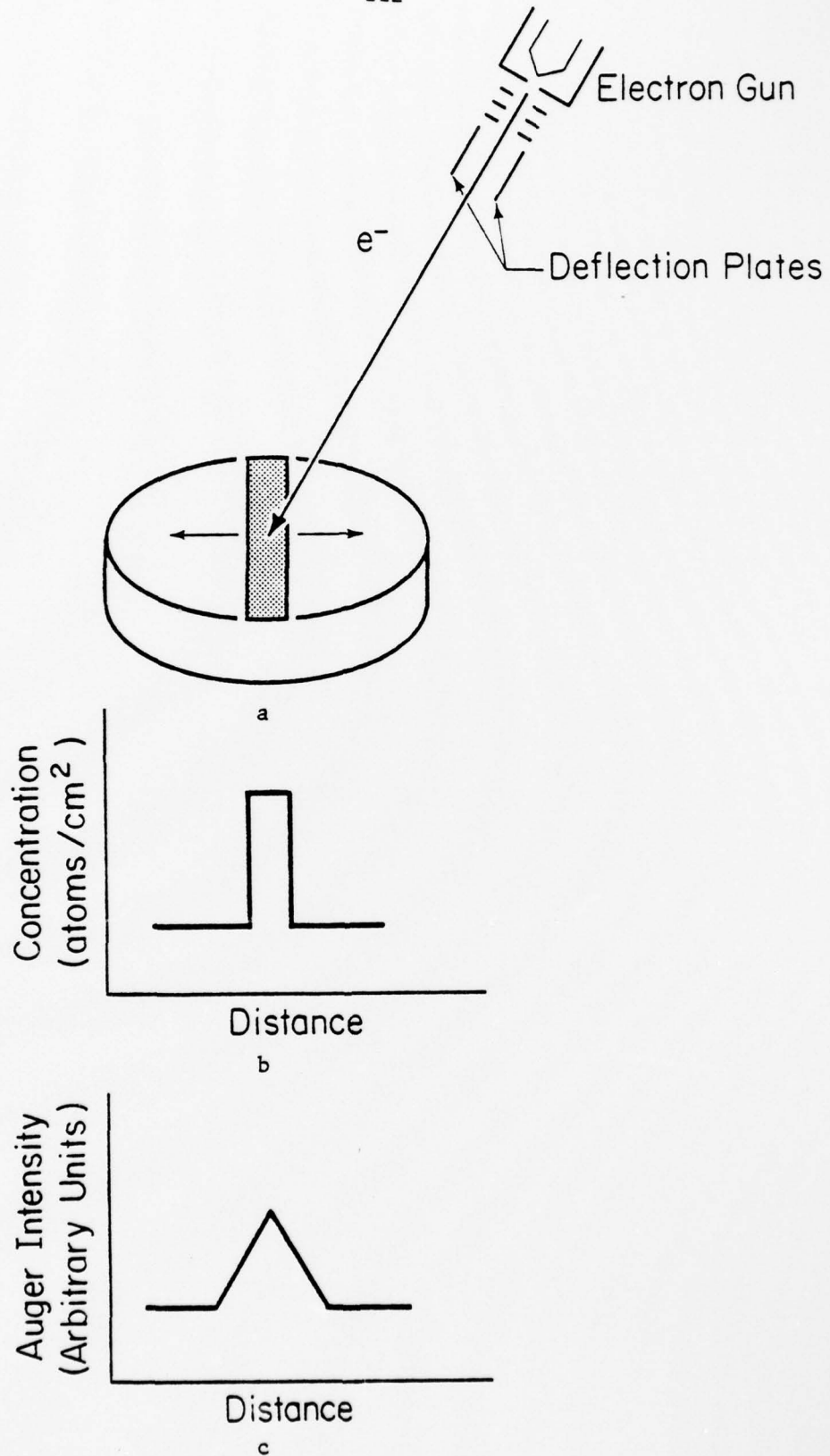


Figure 54. a) Schematic representation of a scanning Auger microscope.  
 b) Concentration profile perpendicular to a line source.  
 c) The observed Auger distribution.

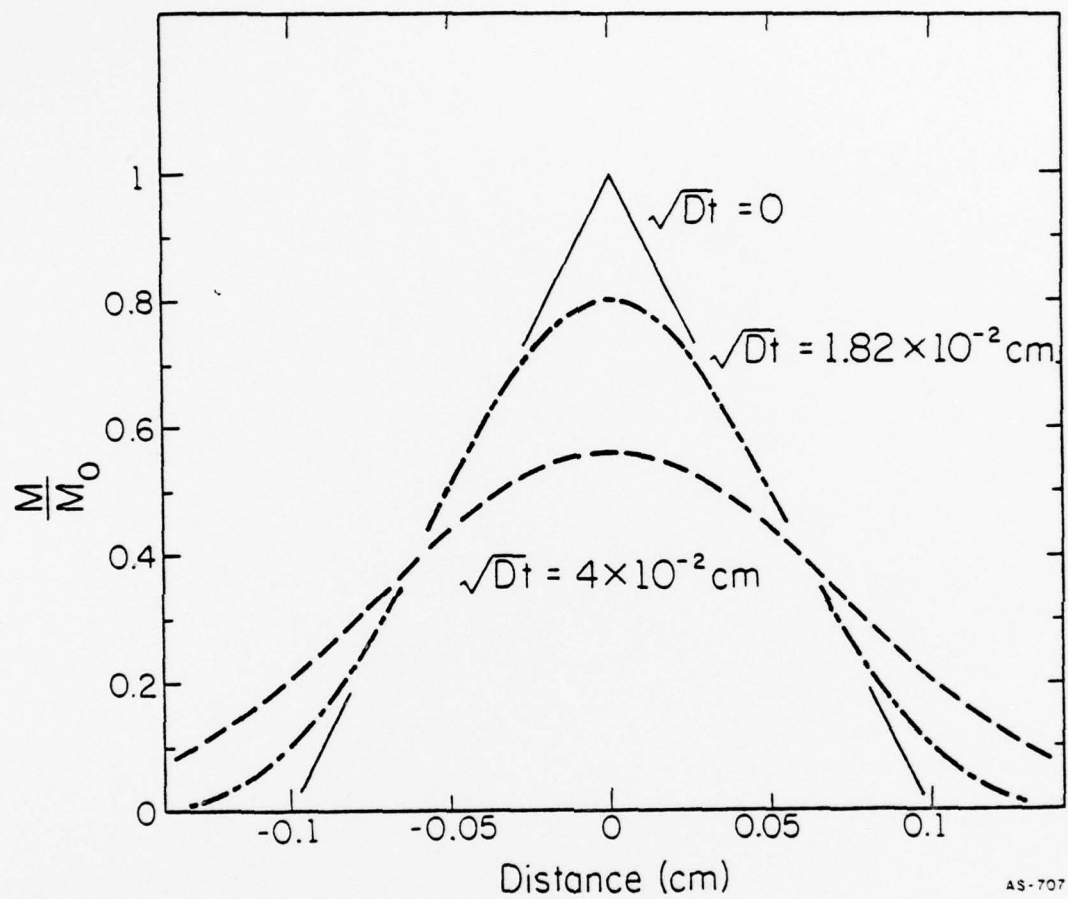


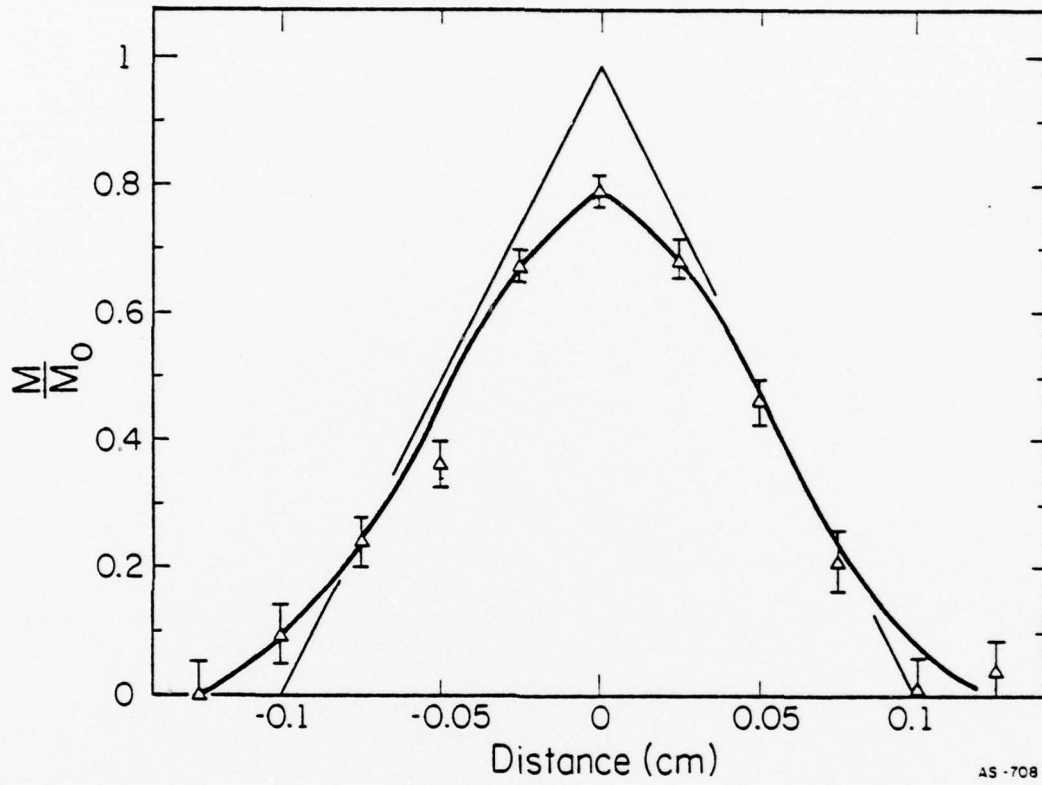
Figure 55. Expected variation in Auger intensity perpendicular to initial line source of atomic nitrogen.

The temperature drops to  $400^{\circ}\text{K}$  in about 20 seconds and within 15 minutes the crystal is at room temperature. At that moment another Auger scan is made perpendicular to the line to obtain a new concentration profile. The concentration distribution so obtained can then be analyzed to obtain the diffusion parameters.

After measuring a diffusion profile, the crystal is cleaned by flashing to a high temperature, a new deposit of chemisorbed nitrogen is formed by electron bombardment, and another diffusion sequence is initiated, but this time at a different annealing temperature. During all of the diffusion measurements the time and temperature of the diffusion sequence were chosen to insure that the loss of material through desorption was negligible.

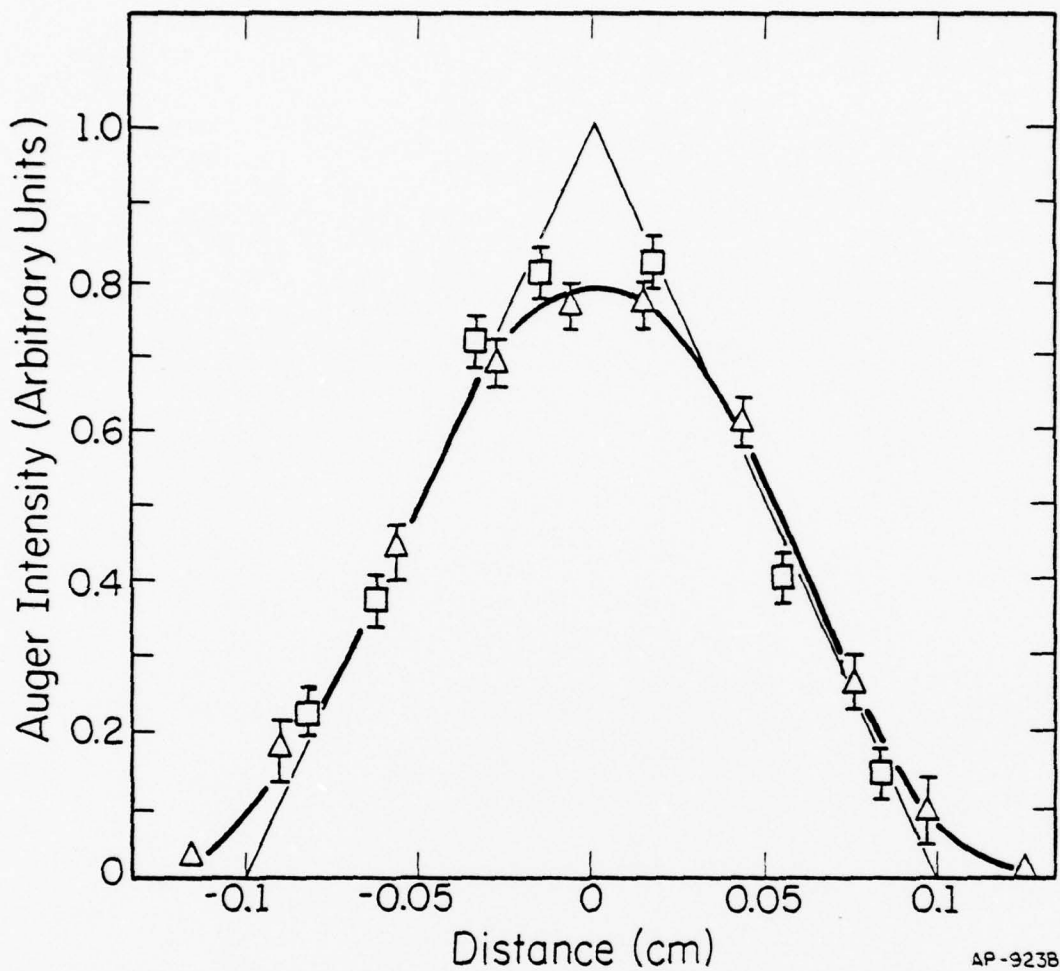
#### IV.4.B. Diffusion

To study the migration of nitrogen atoms over the tungsten surface we deposit a line of atomic nitrogen, as described in Section IV.3.A. Using Auger spectroscopy we are able to follow the broadening of the line as diffusion occurs. Figure 55 shows the concentration profiles expected after various diffusion intervals. The actual spatial variation observed at two different temperatures is shown in Figs. 56 and 57. Plotted in Fig. 56 is the concentration perpendicular to the initial line deposit before and after the crystal is heated to  $885^{\circ}\text{K}$  for 2000 seconds. Figure 57 shows the concentration variation across a line before and after heating to  $800^{\circ}\text{K}$  for 3500 seconds. By fitting the theoretical profile, Eq. (51), to the experimental profile we are able to obtain a value of the diffusion coefficient  $D$ . This procedure is repeated for a number



AS-708

Figure 56. Spatial variation in the Auger intensity perpendicular to a line of atomic nitrogen of width .1 cm for  $t = 0$  seconds and after heating for 2000 seconds at  $885^{\circ}\text{K}$   $\Delta$ .



AP-923B

Figure 57. Spatial variation in the Auger intensity perpendicular to a line of atomic nitrogen of width 0.1 cm for  $t = 0$  seconds —, and after heating for 3500 seconds at  $800^{\circ}\text{K}$   $\Delta$ .

of temperatures, spanning a range of 100°K.

Taking the diffusion coefficient to have the usual form

$$D = D_0 \exp \left[ - \frac{E_m^\ddagger}{RT} \right], \quad (52)$$

with  $E_m^\ddagger$  the activation energy of diffusion, and  $D_0$  a constant, a plot of  $\ln(D)$  vs.  $1/T$  should result in a straight line. Such an Arrhenius plot is given in Fig. 58. Also shown are the desorption results for the electron deposited  $\beta$  nitrogen. This is the first time desorption and diffusion measurements have been made on the same crystal. At a saturation coverage ( $\approx .5$  monolayer) of  $\beta$  nitrogen on the (110) plane of tungsten; we find the activation energy for diffusion  $E_m^\ddagger = 21 \pm 2.2$  kcal/mole, and  $D_0 = 4.66 \times 10^{-2}$  cm<sup>2</sup>/sec ( $1.25 \times 10^{-2} < D_0 < 1.7 \times 10^{-1}$  cm<sup>2</sup>/sec), and the desorption parameters to be  $E_{des} = 79.2$  kcal/mole and  $C_0 \nu_2 = 4.66 \times 10^{13}$  ( $4.14 \times 10^{13} < C_0 \nu_2 < 5.19 \times 10^{14}$ ) molecules (cm<sup>-2</sup> sec<sup>-1</sup>), as previously reported. The method by which we determine the errors in both the diffusion and desorption parameters is discussed in Appendix C.

To check the effect of concentration on the diffusion coefficient we repeated the experiments with an initial coverage only 3/4 of saturation. This reduced surface concentration is produced by exposing the cooled crystal to a saturation dose of  $\gamma$  nitrogen, followed by sweeping the electron beam across the crystal face for 100 seconds, at 100  $\mu$ A emission current, instead of the 300 second irradiation in the previous experiment. Since we started with a saturation concentration of  $\gamma$  nitrogen, the amount of  $\beta$  nitrogen adjacent to the line is  $\approx 0.17$  monolayer. We again plotted  $\ln(D)$  vs.  $1/T$  and the results are shown in Fig. 59, along with the saturation coverage results. In this case  $D_0 = 8.8 \times 10^{-2}$  cm<sup>2</sup>/sec and

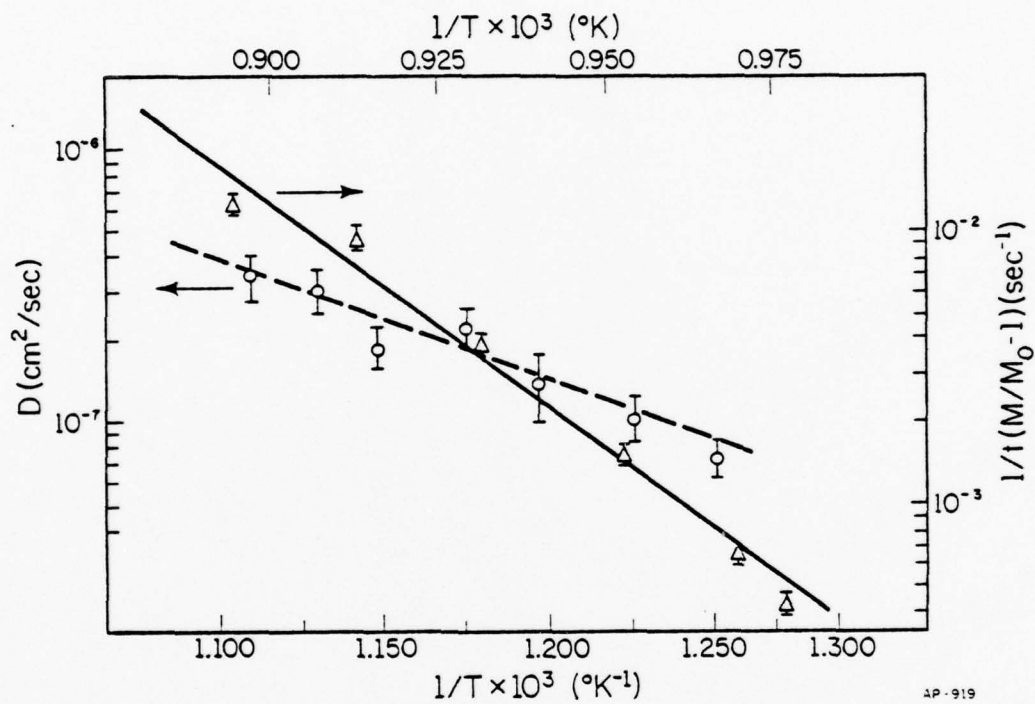


Figure 58. Temperature dependence of surface diffusion  $D$  and of desorption for  $\beta$  nitrogen  $\Delta$  on W(110). Diffusion parameters found are  $E_m = 21$  kcal/mole,  $D_0 = 4.66 \times 10^{-2}$  cm<sup>2</sup>/sec.

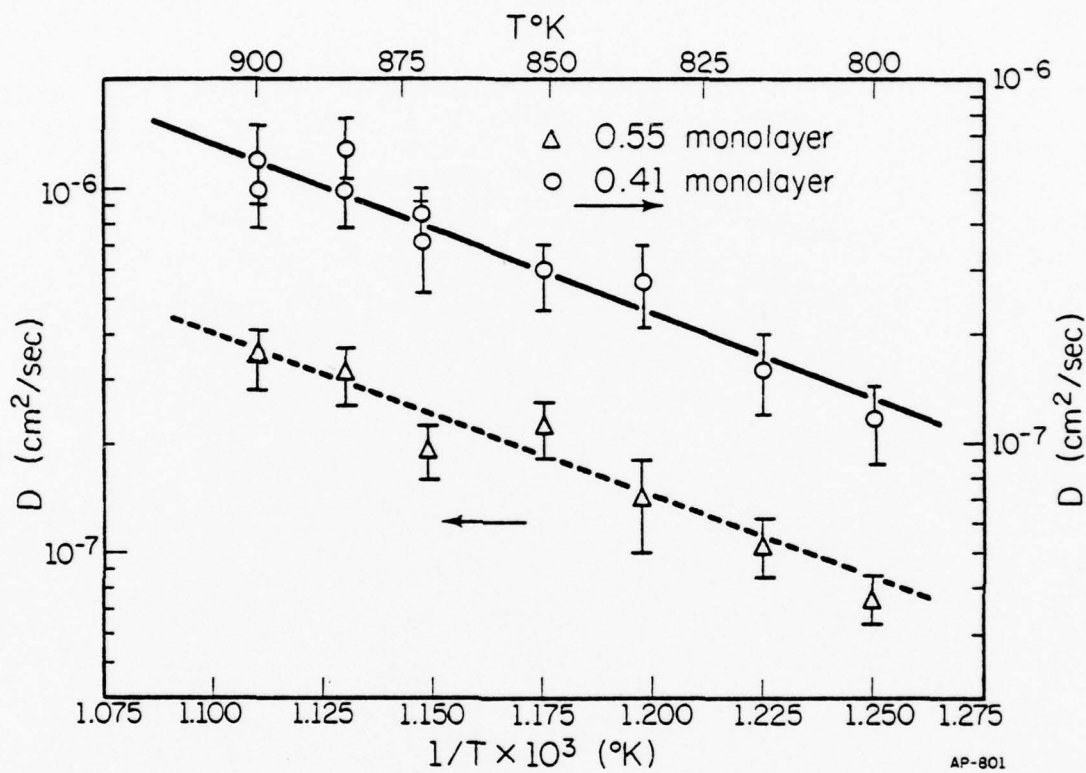


Figure 59. Plot of  $\ln(D)$  vs.  $1/T$  for electron dissociated nitrogen at  
 a) an initial surface coverage of 0.55 monolayer  $\Delta$ ,  
 b) an initial surface coverage of 0.41 monolayer  $\circ$ .  
 Abscissa at left for high concentration, at right for low concentration.

$E_m^\ddagger = 21.27 \pm 2.8$  kcal/mole. The differences in the two measurements are within the standard deviations of each of the activation energies and pre-exponentials. The diffusion measurements at 3/4 saturation were made with a different Auger gun, which may have resulted in a slight variation in the recorded Auger intensity. To check the effect of the new gun, we repeated some of the diffusion experiments at saturation coverages, and obtained results identical to those with the old gun. Table 5 lists the various values of D obtained for different heating schedules and initial concentrations. Although our range of concentrations spanned is small, it appears that diffusion is hardly affected by changes in the concentration of the nitrogen adlayer.

#### IV.4.C. Simultaneous Diffusion and Desorption

We have shown that electron bombarded nitrogen desorbs with the same kinetics as does  $\beta$  nitrogen. However, flash desorption only gives information about the surface species at the desorption temperatures, about  $1100^\circ\text{K}$  in this case. It could still be argued that at the lower temperatures at which diffusion occurs,  $900^\circ\text{K}$ , the electron deposited nitrogen is in still another binding state. It could be that only at  $1000^\circ\text{K}$ , just prior to evaporation, does it convert into  $\beta$  and desorb as such. We can eliminate this objection by examining the simultaneous desorption and diffusion of nitrogen from a line. This type of observation is bound to provide information about desorption and diffusion of nitrogen in the same state. Ideally, it is desirable to operate in a temperature and time regime where the mass loss from the initial deposit is roughly the same for both mechanisms.

Table 5

## Diffusion Parameters

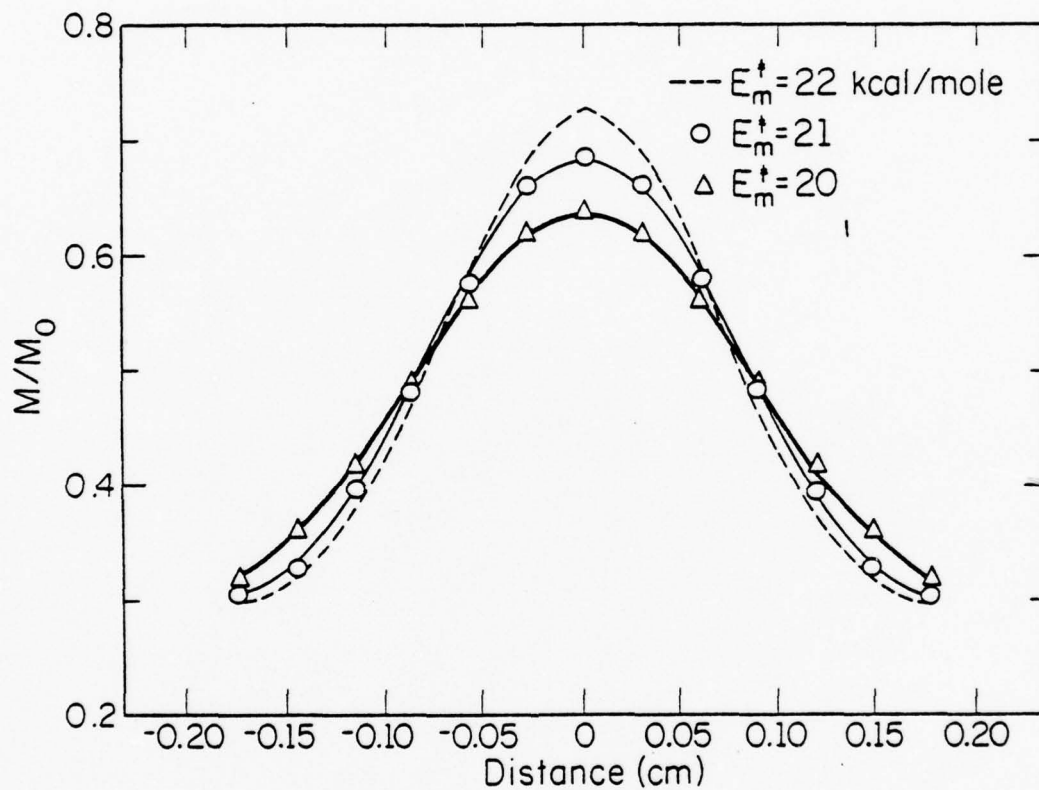
0.55 Monolayer Coverage		0.41 Monolayer Coverage	
Temperature ( $^{\circ}$ K)	D(cm <sup>2</sup> /sec)	Temperature ( $^{\circ}$ K)	D(cm <sup>2</sup> /sec)
800	$7.56 \times 10^{-8}$	800	$1.169 \times 10^{-7}$
815	$1.06 \times 10^{-7}$	815	$1.6 \times 10^{-7}$
835	$1.44 \times 10^{-7}$	835	$2.8 \times 10^{-7}$
850	$2.24 \times 10^{-7}$	850	$2.97 \times 10^{-7}$
870	$1.64 \times 10^{-7}$	870	$4.3 \times 10^{-7}$
885	$3.14 \times 10^{-7}$	870	$3.6 \times 10^{-7}$
900	$3.5 \times 10^{-7}$	885	$6.6 \times 10^{-7}$
		885	$5.08 \times 10^{-7}$
		900	$4.96 \times 10^{-7}$
		900	$6.1 \times 10^{-7}$

To do this, an appropriate time interval and temperature must first be decided for the experiment. The loss of material by diffusion and second-order desorption is given by

$$\frac{dC(x,t)}{dt} = D \frac{d^2C(x,t)}{dx^2} - kC^2(x,t) \quad , \quad (53)$$

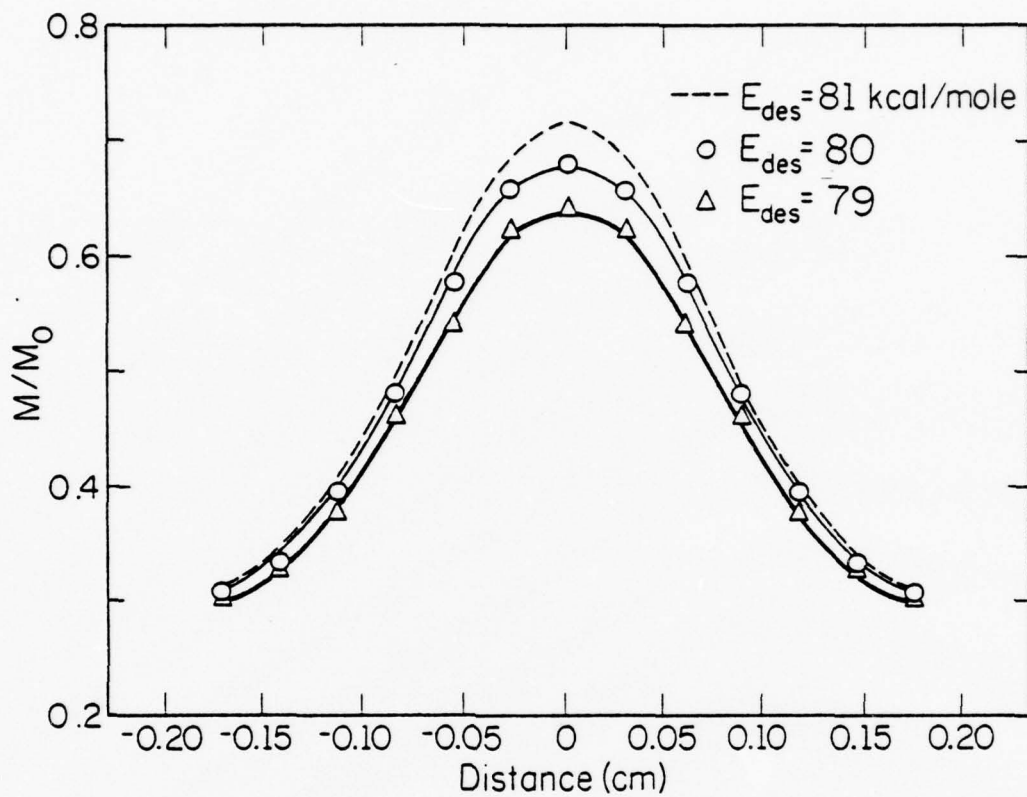
where  $k = \nu_2 \exp[E_{des}/RT]$  is the rate constant for evaporation and  $C(x,t)$  the surface concentration. This equation cannot be solved exactly; however, numerical answers can be obtained, using the program in Appendix B. The calculated concentration is then integrated over the beam dimension to obtain  $\frac{M(x,t)}{M_0}$ , which is proportional to the Auger signal. A number of different heating times and temperatures were tried and approximately equal mass losses occurred for  $t = 1000$  seconds and  $T = 1000^\circ\text{K}$ . For a heating time  $t = 1000$  seconds and temperature  $T = 1000^\circ\text{K}$ , we obtain the calculated desorption and diffusion curves shown in Figs. 60 and 61. These figures show the variation in Auger intensity for a 1 kcal/mole change in the activation energy of desorption. In this temperature and time range, differences in the activation energy for desorption and diffusion should be readily discerned. An increase of one kcal/mole in the diffusion energy causes a smaller decrease in the central section of the concentration gradient and a narrowing of the base. A similar increase in the desorption energy causes an increase in the overall concentration profile.

The result of an actual diffusion and desorption anneal at  $T = 1000^\circ\text{K}$  and  $t = 1000$  seconds is shown in Fig. 62. The best fit is obtained by using the diffusion parameters obtained earlier and increasing the desorption energy by 1.8 kcal/mole, well within the standard deviation of the desorption



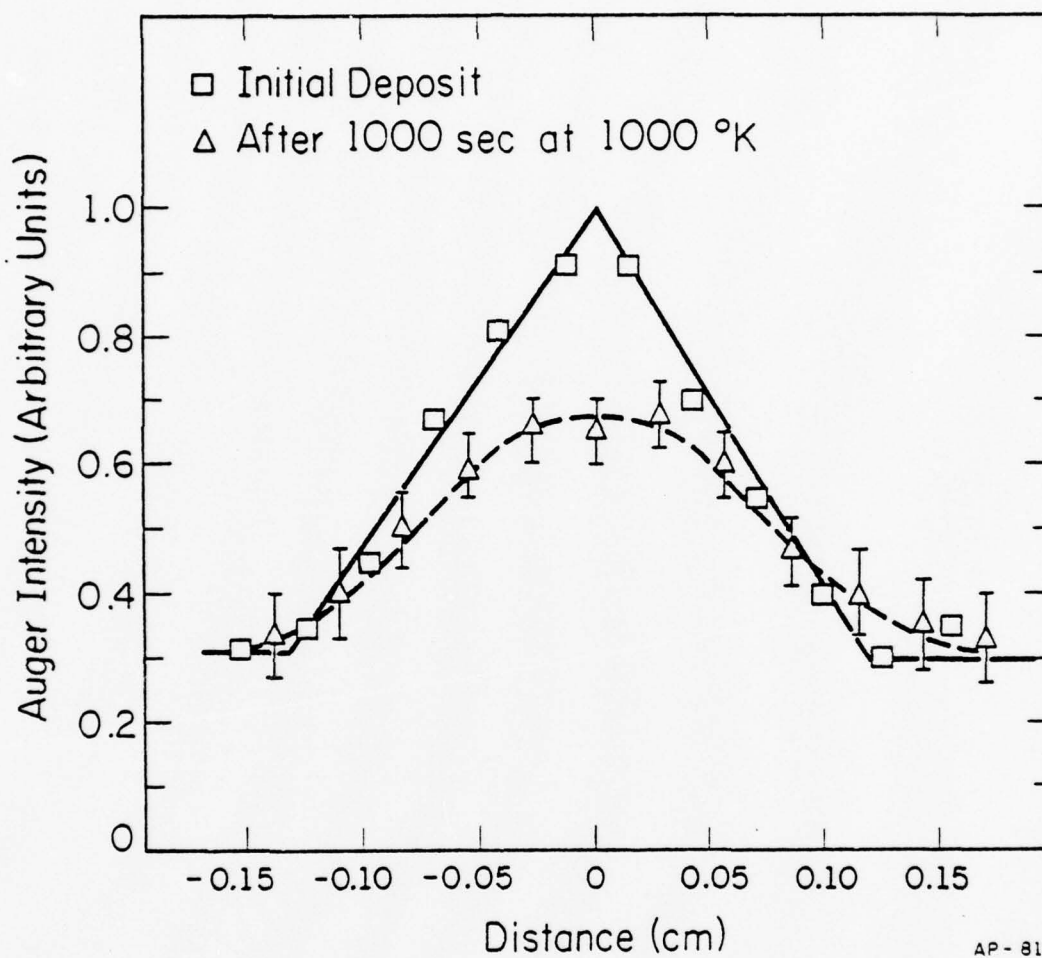
AP-820

Figure 60. Calculated changes in concentration profile, for a 1 kcal/mole change in the activation energy of diffusion when diffusion and desorption occur simultaneously.  $E_{des} = 79.2$  kcal/mole and  $C_{O_2}^v = 4.63 \times 10^{13}$  ( $\text{cm}^{-2} \text{sec}^{-1}$ ).



AP-821

Figure 61. Changes in the concentration profile, when diffusion and desorption occur simultaneously, resulting from a change of 1 kcal/mole in the activation energy of desorption;  $E_m^\ddagger = 21.0$  kcal/mole.



AP-819

Figure 62. Experimental concentration profile for simultaneous diffusion and desorption from a line source.

energy. The diffusion and desorption parameters can now be described by  $E_m^\ddagger = 21$  kcal/mole,  $D_0 = 4.66 \times 10^{-2}$  cm<sup>2</sup>/sec,  $E_{des} = 81$  kcal/mole and  $C_0^{\nu_2} = 4.63 \times 10^{13}$  atoms (cm<sup>-2</sup> sec<sup>-1</sup>). We now have diffusion and desorption occurring simultaneously and the activation energies are almost identical to what we obtained when we observed each event occurring separately.

#### IV.5. Discussion

Flash desorption and Auger spectroscopy indicate that some of the molecularly bound nitrogen undergoes a conversion to the more tightly bound  $\beta$  state. Whether this conversion occurs while the gas is on the surface at the lower temperature or as the result of heating to some higher temperature is unknown. The amount of  $\beta$  found in this manner is  $\approx 0.17$  monolayer. There is the possibility that lattice steps are responsible for this  $\gamma$  to  $\beta$  conversion. From our LEED measurements we know that the step density near the crystal edge is  $\approx 1$  step for every 30 surface atoms, i.e. the terraces are 30 atoms wide. Presumably the molecular  $\gamma$  nitrogen is free to migrate on the surface at 95°K. If on reaching a step, either by impact from the gas or by diffusion over the surface, it dissociates, then we would have two atoms bound tightly to the step, and no further dissociation could occur at that site. The maximum concentration in this case would then be .07 of a monolayer. We found almost twice this amount of atomic nitrogen after desorption of the  $\gamma$  nitrogen. For this model of dissociation to be correct every step atom must be capable of dissociating two molecules of nitrogen. Another possibility is that the step density is higher than 1 in 30.

If steps are necessary for the dissociation of molecular nitrogen on the (110) plane, then at room temperature the gas molecules may strike the surface and remain there for a short period of time, during which they can diffuse to a step and dissociate. If during their residence time they do not migrate to a step, they leave the surface as a molecule. This would explain the low sticking coefficient of nitrogen observed on the (110) plane at room temperature. Once a nitrogen atom is on a step, it effectively poisons the step to further dissociation and only by diffusion from the step can another molecule dissociate there. The relatively low surface coverage observed for nitrogen on the (110) plane at room temperature ( $9.2 \times 10^{13}$  molecules/cm<sup>2</sup>) [13] would then be the result of a diffusion limited dissociation process at the steps. By electron irradiation we are circumventing the normal step dissociation mechanism with another, more efficient mechanism.

As mentioned in Sec. IV.2.B and Sec. IV.3.D, the LEED pattern that develops after adsorption of nitrogen, both at room temperature and by electron bombardment, is enhanced by a slight thermal anneal. It is not necessary to heat the crystal to develop either the p(2 x 2) or structure A. These patterns were also observed after the crystal was allowed to remain at room temperature for 10-20 minutes. If the formation of the LEED pattern is a diffusion controlled process, an estimate of the root mean square displacement necessary to form the LEED pattern can be made. Initially, the nitrogen atoms are assumed to be arranged randomly on the surface and during the 10-20 minutes needed to develop a pattern they diffuse into equilibrium sites. In two dimensions the root mean square

displacement  $\langle r^2 \rangle$  of an atom is given by

$$\langle r^2 \rangle = \sqrt{4Dt} \quad (54)$$

By extrapolating the high temperature diffusion results to room temperature we obtain a value of  $D = 2 \times 10^{-17} \text{ cm}^2/\text{sec}$ . This gives a root mean square displacement of  $\approx 10$  atomic spacings. This is a somewhat larger displacement than might have been expected, considering that the size of the unit cell of the adsorbate, as determined by LEED measurements is only  $\approx 4-8$  atom spacings. However, the experimental error associated with  $D$  is sufficiently large that a root mean square displacement of 4 atoms spacings is within the experimental error of the measurements.

#### SUMMARY

We have developed a method of creating localized deposits of atomic nitrogen on the (110) plane of tungsten by means of electron stimulated dissociation. Not only are the nitrogen atoms bound in the  $\beta$  state, but with a surface concentration 2.2 times that which can normally be obtained by room temperature saturation of the (110) plane. The nitrogen which is deposited by electron irradiation is found to obey second-order desorption kinetics and to desorb with an activation energy of 79.2 kcal/mole. This result is in excellent agreement with the flash desorption measurements for nitrogen adsorbed at room temperature.

From our flash desorption studies we were able to estimate the activation energy and the frequency factor for desorption of  $\gamma$  nitrogen from the (110) plane of tungsten, which we found to be  $E_{\text{des}} = 5.4 \pm .76 \text{ kcal/mole}$  and  $\nu_1 = 10^{10} \text{ sec}^{-1}$ . Although the frequency factor is unusually low, when compared to that of  $\gamma$  nitrogen on the other planes of tungsten, it

does agree very well with the only other work which has been done on the (110) plane. We also found that there is always some  $\gamma$  to  $\beta$  nitrogen at room temperature is  $\approx 0.25$  monolayer.

Our LEED observations indicate that once the adsorbed nitrogen atoms equilibrate on the surface they form into islands. These islands have specific orientations and the borders are in the [100] direction. This is not unexpected, since island growth is perhaps the most common form of adsorption. We also found two different surface structure. One corresponds to a surface concentration of  $< 0.25$  monolayer which results in a  $p(2 \times 2)$  pattern. This pattern forms if the nearest neighbor sites around any one nitrogen atom are always empty. The other LEED pattern, structure A, was only visible for surface concentrations  $> 0.25$  monolayer. We also found, on occasion, a structure composed of rotated  $(2 \times 4)$  domains. Both structure A and the rotated  $(2 \times 4)$  pattern could only be achieved by electron stimulated dissociation.

The development of the LEED pattern also appears to be a thermally activated process. After the nitrogen is deposited on the surface at room temperature, there is no immediate change in the clean tungsten pattern. Only after the crystal is heated to  $800^\circ\text{K}$  for several seconds or permitted to remain at room temperature for 15-20 minutes does the new pattern appear.

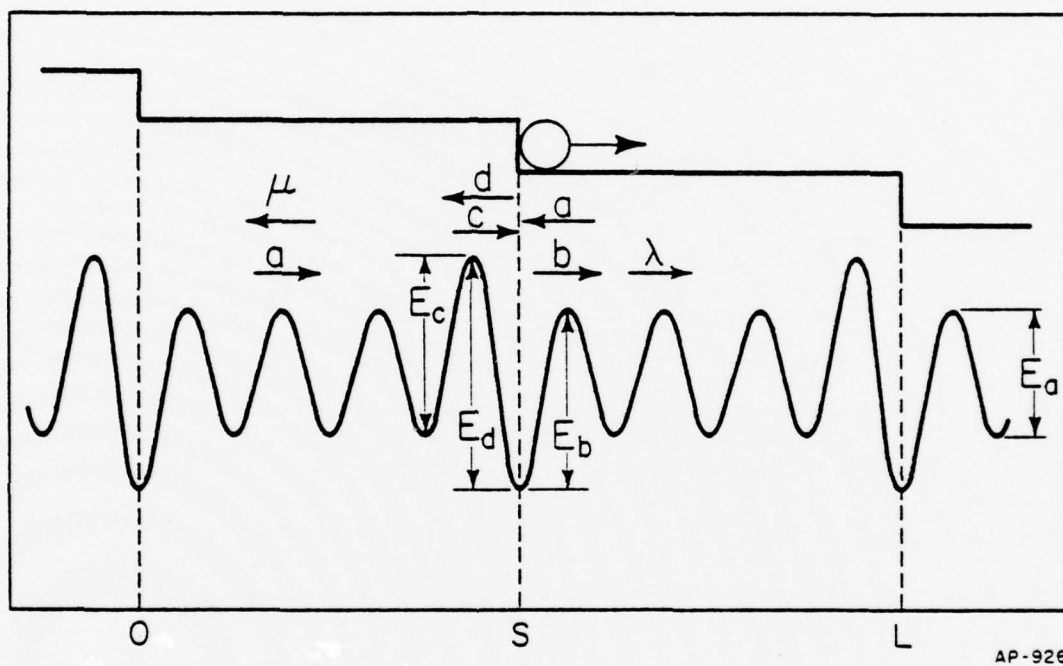
From the activation energy of desorption measured in our experiments we can deduce the binding energy of a nitrogen atom on the surface. The binding energy  $E_b$  is given by:

$$E_b = \frac{1}{2} (\chi' + E_{des}) \quad (55)$$

where  $\chi'$  is the dissociation energy of the molecule in free space. Using

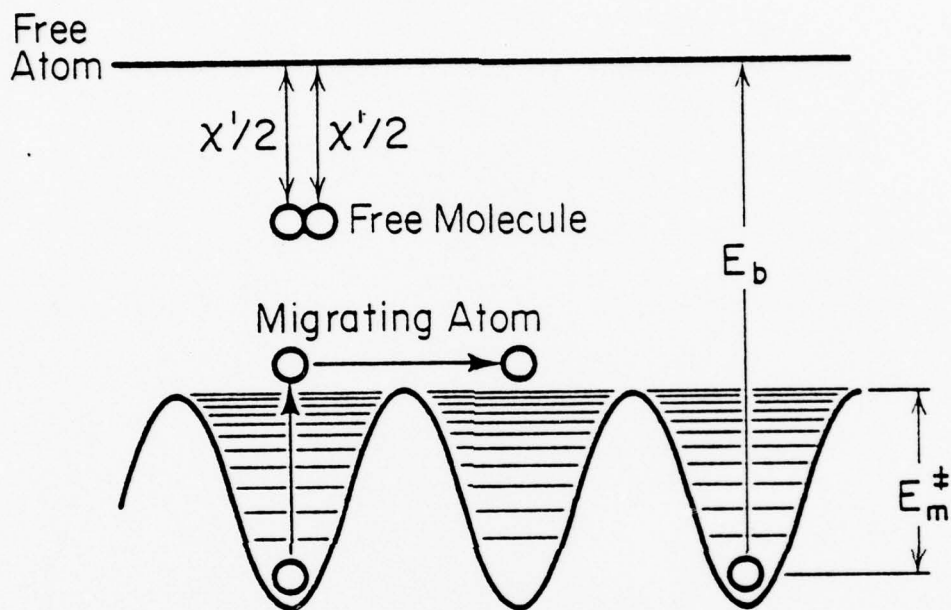
the desorption energy found earlier, we calculate the binding energy per atom to be 153 kcal/mole. The ratio of the binding energy to the activation energy for surface diffusion is 7.4 to 1. This is significantly higher than has been reported on rougher surfaces. From field emission measurements, a ratio of approximately 4.5 to 1 appears appropriate for nitrogen on the high index planes of tungsten around the (110) [4]. However, around the (111), diffusion occurred with the same activation energy as observed here on the (110). These comparisons are, at best, of qualitative significance; the early diffusion measurements were only semiquantitative, and direct observations of desorption from stepped surfaces are not available. It is of interest, however, that measurements of hydrogen diffusion over rough surfaces show much the same trend. Values of  $\approx 7$  have been reported for the binding energy to the diffusion barrier [3]. It does appear, therefore, that in diffusion over a smooth surface the activation barrier confronting an atom is, in fact, smaller in relation to the binding energy than on atomically rough surfaces.

The value of the prefactor  $D_0$  in the surface diffusion coefficient for nitrogen atoms on the tungsten (110) provides some information about the dynamics of atomic motion and whether surface steps are limiting the diffusion process. To see this we represent the surface as being composed of a series of terraces of width  $\frac{L}{2}$ , as shown in Fig. 63. For a surface atom located at an arbitrary position,  $i$ , the rate constant describing its motion to the right is  $\lambda_i$ . The atom can also move to the left, and this movement is assigned the rate constant  $\omega_i$ , as indicated in Fig. 63. The actual values of the rate constants depend on the location of the surface atom. Jumps on the flat terraces themselves all occur at



AP-926

Figure 63. Schematic drawing of a stepped surface with adatom. The step width is  $L/2$  and the associated rate constants of the adatom are  $a$ ,  $b$ ,  $c$ , and  $d$ .



AS-754

Figure 64. Energy diagram showing the activation energy of diffusion and desorption of an adatom on an ideal surface.

the same rate, independent of the exact position. This rate is denoted by  $a$ . At the edges, however, jump rates are different, and are assigned the values  $b$ ,  $c$ , and  $d$  shown in Fig. 63. The average time required for an atom to reach either of two end points, arbitrarily chosen as  $x = 0$  or  $x = L$ , starting at  $x = i$ , where  $0 < i < L$ , is given by [44]

$$\tau_i = A_i + B_i \left[ \frac{1 + \lambda_2 A_2}{\mu_1 + \lambda_1 (1 + B_2)} \right], \quad (56)$$

where

$$A_i = \sum_{m=i}^{L-1} \sum_{j=i}^m \frac{1}{\lambda_j} \prod_{k=j}^m \frac{\mu_k}{\lambda_k}, \quad (57)$$

and

$$B_i = \sum_{n=1}^{L-1} \prod_{k=1}^n \frac{\mu_k}{\lambda_k}. \quad (58)$$

Using the rate constants of Fig. 63, for an atom initially at point  $i$ , where  $L = 2s$  and  $i > s$ , we obtain,

$$\begin{aligned} A_i &= \frac{d}{cb} (s-1)(2s-i-1) + \frac{1}{b} (2s-i-1) \\ &+ \frac{1}{a} (i-1)(2s-i) + \frac{ad}{c^2 b} (s-1) + \frac{a}{bc} + \frac{b}{c}, \end{aligned} \quad (59)$$

or

$$A_i = \frac{1}{2a} (2s^2 - 6s + 4 - i^2 + i) + \left[ (s-1) \frac{d}{cb} + \frac{1}{b} \right] (s-1 + \frac{a}{c}) + \frac{2(s-1)}{c}. \quad (60)$$

Specifically,

$$A_2 = \frac{s^2 - 3s + 1}{a} + \left[ (s-1) \frac{d}{cb} + \frac{1}{b} \right] (s-1 + \frac{a}{c}) + \frac{2(s-1)}{a}. \quad (61)$$

A similar calculation shows that,

$$B_i = \frac{ad}{bc} \left( i-1 + \frac{a}{c} \right) \quad (62)$$

and

$$B_2 = \frac{ad}{bc} \left( 1 + \frac{a}{c} \right) .$$

Referring to Fig. 63, we see that,

$$E_d = E_b + E_c - E_a . \quad (63)$$

Assuming that the pre-exponential factors for all the rate expressions are identical, then,

$$ad = bc . \quad (64)$$

For an atom initially at  $i = s$ , it then follows that

$$B_s = \left( s-1 + \frac{a}{c} \right) , \quad (65)$$

and

$$A_s = \left[ \frac{1}{a} (s-1) + \frac{1}{b} \right] \left( s-1 + \frac{a}{c} \right) + \frac{s-1}{c} + \frac{s^2-3s+2}{2a} . \quad (66)$$

The transit time,  $\tau_s$  now follows from Eq. (56) as

$$\tau_s = \frac{1}{2a} \left( s-1 + \frac{a}{c} \right) \left( s-1 + \frac{a}{b} \right) . \quad (67)$$

To visualize the effects of a step which acts as a trap for a migrating atom, we assume that  $a = c$  and  $b = d$ ; the transit time is given by

$$\tau_s = \frac{s(a+(s-1)b)}{2ab} , \quad (68)$$

where  $a$  is the rate constant for motion on the terrace and  $b$  the rate constant for removal from the step edge. That Eq. (68) is reasonable is clear on examining a limiting case, which corresponds to diffusion over a flat plane, for which  $a = b$ . In this case Eq. (68) becomes

$$\tau_s' = \frac{s}{2b} . \quad (69)$$

and the mean square displacement of an atom in time  $t$  is given by,

$$\langle \overline{x^2} \rangle = \frac{t}{\tau_s'} (sl^2) = 2Dt , \quad (70)$$

or

$$D = al^2 , \quad (71)$$

which is just the result obtained for a random walk experiment.

For the case of interest where  $b \ll a$ , diffusion from the step edge being the limiting step, Eq. (68) becomes,

$$\tau_s'' = \frac{s}{2b} , \quad (72)$$

and

$$\frac{t}{R\tau_s''} (ls)^2 = 2Dt . \quad (73)$$

The diffusion coefficient is now given by

$$D = bl^2s = vl^2s \exp(-E_m^\ddagger/RT) , \quad (74)$$

where  $\nu$  is the frequency factor for jumps. The pre-exponential constant  $D_0$  is now  $\nu l^2 s$ . That is,  $D_0$  is larger, by a factor equal to the terrace width ( $s$ ), than when diffusion occurs over a flat surface. In our experiment we found the prefactor to be quite normal and of a magnitude expected for an atom moving over sinusoidal potential, as shown in Fig. 64,; and we therefore conclude that trapping at lattice steps does not play a dominant role. It would still be interesting to establish the possible contribution of steps more definitively, both by measurements of diffusion along and perpendicular to the step edges, and by artificially producing steps on the surface during the initial crystal preparation.

From the evidence available right now, in any event, it appears that nitrogen diffusion on the (110) plane of tungsten occurs in quite a simple fashion, over a rather smaller barrier than expected from studies on high index surfaces.

## APPENDIX A

## Electron Bombardment Formation of Surface Devices

Electron stimulated dissociation can be used in the fabrication of a number of novel surface devices, among which are a surface layer mass memory and a possible method of growing localized surface deposits. Although we have demonstrated the feasibility of depositing nitrogen on the (110) plane of tungsten, it may be possible to extend this technique to other, more practical systems.

A surface layer mass memory can be fabricated in much the same manner that we create the localized nitrogen deposits, Sec. IV.3.A. Now, however, instead of depositing a single dot, as in Fig. 41, we deposit a binary code. The technique by which this code is deposited is shown in Fig. A1 where a dot represents a "1" and a blank space represents a "0".

In this manner a surface memory can be developed. To read this device, any number of surface sensitive techniques can be used, such as Auger spectroscopy, secondary electron emission or electron loss spectroscopy, as illustrated in Fig. A2. An actual picture of such a device is shown in Fig. A3, which was taken by monitoring the secondary electron emission current. A crude estimate of the time necessary to write on this device can be made by using Eq. (42) and the value of the dissociation cross-section,  $Q_{\text{diss}}$ , found in Sec. IV.3.B., which is  $Q_{\text{diss}} = 3 \times 10^{-18} \text{ cm}^2$ . Assuming a surface concentration of 0.28 monolayer corresponds to a "1" and that the electron source is a field emission electron gun, capable of providing a beam current of  $10^{-8}$  -  $10^{-9}$  ampere within a beam diameter of

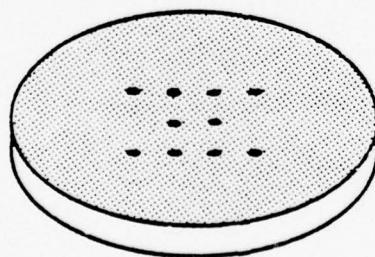
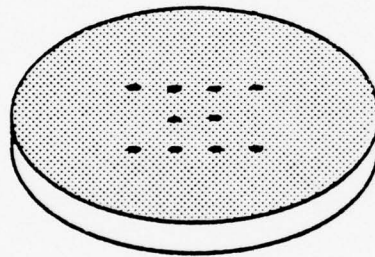
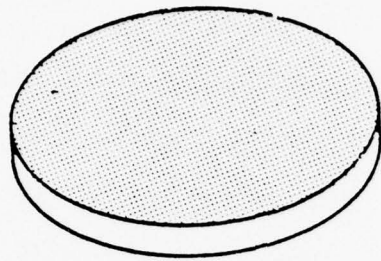


Figure A1. Writing procedure for the surface layer mass memory, a) the molecular gas is deposited on the surface, b) followed by local irradiation to deposit the binary code, c) warming the crystal to remove the non-dissociated molecules.

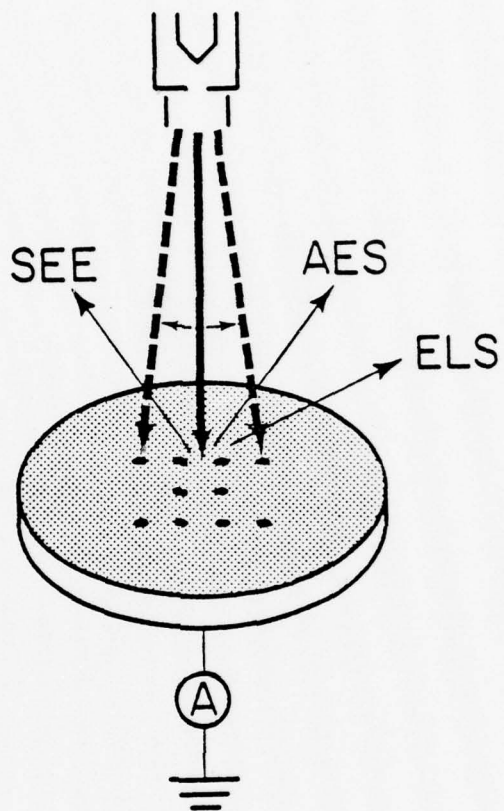


Figure A2. Possible techniques (Auger electron spectroscopy, electron loss spectroscopy and secondary electron emission), which may be used to read the surface layer mass memory.



Figure A3. Secondary electron emission photograph of the surface layer mass memory device with a binary code on the surface.

100 Å, the writing rate is  $\approx 10^5$  bits/sec. Although this is slow by current standards this technique does offer the possibility of achieving very high bit densities  $\approx 10^{12}$  bits/cm<sup>2</sup>, considerably higher than what is presently available.

In any event, the practicality of this device will depend upon the reading speed, which depends on the exact system used and the method of reading.

The second possible use of electron stimulated dissociation is in the growth of a material on a substrate, e.g., silicon on silicon. In this case a layer of silane (SiH<sub>4</sub>) would be continually deposited onto a silicon surface followed by local irradiation. Upon irradiation the silane dissociates leaving a silicon outcropping. By continually replacing the silane layer a local deposit is formed. Using very small diameter electron beams, deposits of small dimensions could be made. A process such as this could be used to fabricate surface gratings and integrated circuits of a size smaller than that which is currently possible.

APPENDIX B  
Computer Programs

This appendix is composed of four computer programs. The programs are all written in FORTRAN, and each has a brief description at the start.

## LEED.F4

Program LEED.F4 is used to calculate the interference function for the data listed in file GOOF1.DAT, along a characteristic line. That line is determined by setting AH ( $AH=(b/\lambda)\cos\beta$ ) equal to a fixed value and varying AH2 ( $AH2=(a/\lambda)\cos\alpha$ ) about the area of interest.

```

DIMENSION I(32,32),F(32,32)
      CALL IFILE(20,'GOOF1')
  90  READ(20,100) I
  100 FORMAT(32I)
  130 PI2=6.2831753071896
      CALL OFILE(20,'DEP1')
      N=240
      WRITE(20,11)N
  11  FORMAT(I)
      DO 12 JJ=1,N
      AJJ=JJ
      AH=AJJ*.01-1.15
      WRITE(20,13)AH
  13  FORMAT(F16.8)
  12  CONTINUE
      DO 270 JJ=1,N
      AJJ=JJ
  45  AH=AJJ*.01-1.15
  46  AH2=0.0
  140 SUM1=0.
  145 SUM2=0.
  150  DO 240 M=1,32
  160  DO 230 N=1,32
      AG=PI2*((N-16)*AH+(M-16)*AH2)
      F(M,N)=I(N,M)
      XX=F(M,N)
  190  A=(XX)*COS(AG)
  200  B=XX*SIN(AG)
  210  SUM1=SUM1+A
  220  SUM2=SUM2+B
  230  CONTINUE
  240  CONTINUE
  245  SUM=SUM1**2.+SUM2**2.
      IF(AJJ.GE.2) GO TO 1233
      WRITE(20,123)N
  123  FORMAT(G)
  1233  WRITE(20,124)SUM
  124  FORMAT(G)
  270  CONTINUE
  290  END

```

## LDIF.F4

This program calculates the variation of the Auger intensity across a line of width  $2H$  in accordance with Eq. (51), for a fixed value of  $Dt$ . This calculated intensity is then compared to the experimental obtained values of  $M(t)/M_0$  and  $Dt$  is changed until the best least squares fit is obtained, from which the diffusion coefficient  $D$  is obtained. The input variables are the Auger peak-to-peak height  $PPO(IK)$  and the position  $XXO(IK)2$ . The output ( $Dt$ ) is  $AMIN$ .

```

      DIMENSION A(25),B(30),ER(4),C(4)
      DIMENSION ST(1000),XX1(13),PPO(13)
      CALL IFILE(20,'LC851')
      MN=1000
      N=9
      DO 24 IK=1,N
      READ(20,22)XX1(IK)
22  FORMAT(F14.6)
      WRITE(5,22)XX1(IK)
24  CONTINUE
      DO 27 IK=1,N
      READ(20,23)PPO(IK)
23  FORMAT(F14.8)
      WRITE(5,23)PPO(IK)
27  CONTINUE
      SSDT=2.43E-2
      M=24
      A(1)=16443152242714E-13
      A(2)=-49760497548E-13
      A(3)= 0643570883797E-13
      A(4)= 0196418177368E-13
      A(5)=-0001244215694E-13
      A(6)=-0009101941905E-13
      A(7)=-0001796219835E-13
      A(8)= 0000139836786E-13
      A(9)=      164789417E-13
      A(10)=      39009267E-13
      A(11)=-      00893145E-13
      A(12)=-      03747896E-13
      A(13)=-      01298818E-13
      A(14)=-00136773E-13
      A(15)=      00077107E-13
      A(16)=      00046810E-13
      A(17)=      00011844E-13
      A(18)=-      0005E-13
      A(19)=-      1384E-13
      A(20)=-      0652E-13
      A(21)=      0145E-13
      A(22)=      0010E-13
      A(23)=      0024E-13

```

```

A(24)=          0011E-13
A(25)=          0002E-13
130 DO 4000 IDT=1,1000
      SQDT=SSDT
      SQDT=SQDT+(1E-6)*IDT
20   H=3.*.05/3.75
      DO 1000 IK=1,M
30   X1=(2.67/2.1)*(XX1(IK)+(15.E-3))
60   X1=X1-H
70   X2=X1+2.*H
      C(1)=(H-X2)/(2.*SQDT)
      C(2)=(H-X1)/(2.*SQDT)
      C(3)=(H+X2)/(2.*SQDT)
      C(4)=(H+X1)/(2.*SQDT)
      SQIPI=.56418958
      E=SQDT/(2.*H)
      IJ=0
80   IJ=IJ+1
90   W=C(IJ)
      X=ABS (W)
      IF (ABS (X)-.01) 1, 2, 2
1   XERR=2.0/(3.0*1.77245385)*X*(3.0-X**2)
      GO TO 6
2   Z=(X-1.0)/(X+1.0)
      DO 3 I=1,30
      B(I)=0.
3   CONTINUE
      DO 4 I=1,M
      M1=(M+1)-I
      B(M1)=2.0*Z*B(M1+1)-B(M1+2)+A(M1+1)
4   CONTINUE
      F=-B(2)+Z*B(1)+.5*A(1)
      XERR=1.0-(1.0/1.77245385)*(EXP(-(X**2)))*F
      IF (ABS (X)-.01) 6, 7, 7
6   CERR=1.0-XERR
      GO TO 5
7   CERR=(1.0/1.77245385)*(EXP(-(X**2)))*F
5   ERR=XERR
      JI=2
      IF(W)200,210,210
200  JI=1
210  ER(IJ)=ERR*(-1)**JI
      IF(IJ-4)80,150,150
150  AMTT=-C(1)*ER(1)+C(2)*ER(2)+C(3)*ER(3)-C(4)*
ER(4)
      TT=SQIPI*(EXP(-C(2)*C(2))+EXP(-C(3)*C(3))-E
XP(-C(1)*C(1)))
      TTT=SQIPI*(-EXP(-C(4)*C(4)))

```

```
      AMT=E*(AMTT+TT+TTT)
170   STA=((AMT-PPO(IK))**2.)/((-9.857E-2)*.75*PPO
(IK)+9.957E-2)**2.
      ST(IDT)=ST(IDT)+STA
      CHI2=ST(IDT)
1000  CONTINUE
77    INK=IDT-1
      IF(IDT.EQ.1) GO TO 4000
      AMINL=SQRT(ST(INK))
      IF(ST(IDT).LT.ST(INK))GO TO 100
      GO TO 3000
100   AMIN2=SQRT(ST(IDT))
      QQ=ink
4000  continue
3000  DDD=SSDT+(1E-6)*(QQ+1.)
      WRITE(5,560)AMIN2,DDD
560   FORMAT(7H AMIN2=,E16.8,10H SQRT(DT)=,E16.8)
5000  END
```

## POO.F4

This program is used to calculate the theoretical Auger intensity, in accordance with Eq. (53) when material is lost by both diffusion and desorption from a line source. The values of the activation energy of desorption, QDES, diffusion, QDIF and temperature (T5) are varied until the best fit is obtained.

```

DIMENSION C(0/5000),D(0/5000)
REAL L1,K,N2
Z=2**12
T=0
T1=0
  QDIF=21547.
  QDES=80000.
  T5=1000.
  D1=(4.66E-2)*EXP(-QDIF/(1.9872*T5))
  X2=1E-34/D1
  K=(4.6/39.6)*EXP(-QDES/(1.9872*T5))
  X1=SQRT(1E-34/K)
  C1=1.188E14
  C0=2.772E14
  C2=C1+C0
  S=5
  L1=.05625
  T0=1
  H1=6
  H2=3
  H=10
  T9=1000.
  CALL OFILE(20,'PO48')
  K1=2**H1
  K5=K1+1
  K2=2**S
  P=K2*3.1415926
  H3=(L1/K1)**2
  H4=T0/2**H2
  H5=1/H
  WRITE(20,10)
  WRITE(20,15),D1,K,S,H1
  WRITE(20,20)
  WRITE(20,25),C0,C1,H2,L1
  WRITE(20,26)
  WRITE(20,27),QDIF,QDES,T5
10  FORMAT(' D K S H1 ')
15  FORMAT(4G)
20  FORMAT(' C0 C1 H2 L1')
```

```

25     FORMAT(4G)
26     FORMAT(' QDIF QDES TEMP. ')
27     FORMAT(3G)
      DO 100 N=0,K1
      C(N)=C2
100    CONTINUE
      K9=K1*(1.+1./K2)
      DO 120 N=K1,K9
      C(N)=C1+C0*(1+COS((P*(N-K1))/K1))/2
120    CONTINUE
      DO 140 N=K9,Z
      C(N)=C1
      D(N)=0
140    CONTINUE
      WRITE(20,30)
30     FORMAT(' TIME C(0) C(L/4) C(L/2) C(L)
C(3L/2)')
500    D(0)=2*(C(1)-C(0))/H3
      DO 160 N=1,Z
      D(N)=(C(N+1)-2*C(N)+C(N-1))/H3
      IF ((C(N-8)-C(N)).GE.1E-6) GO TO 160
      IF(N.GE.K5) GO TO 532
      GO TO 160
532    J=N
      GO TO 541
160    CONTINUE
541    DO 180 N=J,Z
      C(N)=C(N-8)
180    CONTINUE
      DO 200 N=0,Z
      A5=C(N)*K
      IF(ABS(C(N)).LT.X1) GO TO 612
      IF(ABS(D(N)).LT.X2) GO TO 616
616    C(N)=C(N)+H4*(D1*D(N)-A5*C(N))
      GO TO 619
612    IF(ABS(D(N)).LT.X2) GO TO 619
      C(N)=C(N)+H4*D1*D(N)
      GO TO 619
      C(N)=C(N)-H4*A5*C(N)
619    IF(C(N-8)-C(N).GE.1E-6) GO TO 200
      IF(N.GE.K5) GO TO 622
      GO TO 200
622    J=N
      GO TO 631
200    CONTINUE
631    DO 220 N=J,Z
      C(N)=C(N-8)
220    CONTINUE
      T=T+H4

```

```
T1=T1+H4
IF(T1.LT.H5*T9) GO TO 500
WRITE(20,50),T,C(0),C(.5*K1/2.),C(K1/2.),C(K
1),C(3.*K1/2.)
50  FORMAT(6E12.6)
    T1=0
    IF(T.LT.T9) GO TO 500
    WRITE(20,60)
60  FORMAT(' X AREA')
    DO 260 I=1,30
    N1=(I-1)*K1/8.
    E=0.
    E2=0.
    E3=0.
    A1=0.
    A2=0.
    E4=0.
    DO 240 N=N1+1,N1+K1
    A=C(N)/(K1*2*(C0+C1))
    E=E+A
240  CONTINUE
    IF(N1.GT.K1-1) GO TO 870
    GO TO 920
870  DO 280 N=N1-K1,N1
    A=C(N)/(2*K1*(C0+C1))
    E2=E2+A
280  CONTINUE
    GO TO 1000
920  DO 300 N=0,N1
    A=C(N)/(2*K1*(C0+C1))
    E3=E3+A
300  CONTINUE
    DO 320 N=1,K1-N1
    A=C(N)/(2*K1*(C0+C1))
    E4=E4+A
320  CONTINUE
1000 A1=E+E2+E3+E4
    N2=N1*L1/(K1)
    WRITE(20,55),N2,A1
55  FORMAT(2G)
260  CONTINUE
    END
```

## FLADES.F4

THIS PROGRAM SEPERATES THE FLASH DESORPTION SPECTRUM INTO THE DESORPTION OF TWO FIRST ORDER DESORPTIONS. THE BEST ESTIMATE OF THE FIRST  $T_p$  IS PUT IN, THE OUTPUT IS  $E_1$  OF THAT PEAK. THE INPUT DATA IS  $N/N_p$  AND TEMP AT THE VALUES OF  $N/N_p$ . THE OUTPUT IS THE NORMALIZATION OF THE SECOND CURVE, ITS  $T_p$  (GIVEN  $ASTP_2$ ) AND  $E_2$ .

```

DIMENSION T(12),Y(12),YTHE(12),Y1THE(12),Y2THE(12),TE
MP1(12)
DIMENSION TEMP2(12),CHISQ(20000),Y1(12),Y2(12),CHISQO
(20000)
10 CALL IFILE(20,'DES2')
15 DO 27 I=1,9
20 READ(20,25) Y(I)
25 FORMAT(G)
27 CONTINUE
28 DO 37 I=1,9
30 READ(20,35) T(I)
35 FORMAT(G)
T(I)=T(I)+20.
37 CONTINUE
TP=172.
DO 44 I=1,5
WRITE(5,43) Y(I),T(I),TP
43 FORMAT(1H 'N/NP=',G,'TEMP=',G,'TP=',G)
44 CONTINUE
50 R=1.9872
80 E0=8475.
90 E00=7800.
110 DO 250 II=1,20
125 CHSQ=0.0
120 DO 210 I=1,5
130 E1=E0+50.*II
133 X=E1/(TP*R)
135 XX=E1/(T(I)*R)
140 TEMP1(I)=XX-X
150 YT=TEMP1(I)-1.+(EXP(-TEMP1(I)))*((T(I)/TP)**2.)
160 YTHE(I)=1./(EXP(YT))
170 CHI=(Y(I)-YTHE(I))**2.
180 CHSQ=CHI+CHSQ
190 IF(I.LE.4) GO TO 210
200 CHISQO(II)=CHSQ
210 CONTINUE
220 IF(II.EQ.1) GO TO 250
IA=II-1

```

```
230 IF(CHISQ(IA).GT.CHISQ(II)) GO TO 250
240 E11=E0+50.*(IA)
    ABC=CHISQ(IA)
    GO TO 260
250 CONTINUE
260 WRITE(5,270) E11,ABC
270 FORMAT(1H 'E1=',G,' CHISQ=',G)
    ICOUNT=0
290 T0=185.
    IJKA=0
    CHSQ=0.0
300 IJK=0
310 DO 570 JJ=1,40
320 DO 560 JJK=1,10
330 DO 550 JJN=1,20
    CHSQ=0.0
340 DO 490 J=3,9
350 TP2=T0+JJK
360 E2=E00+50.*JJ
370 X=E2/(R*T(J))
380 XX=E2/(R*TP2)
390 TEMP2(J)=X-XX
    XY=E11/(R*T(J))
    XXY=E11/(R*TP)
    TEMP1(J)=XY-XXY
400 Y1TH=TEMP1(J)-1.+(EXP(-TEMP1(J)))*((T(J)/TP)**2.)
    Y1THE(J)=1./(EXP(Y1TH))
410 Y2(J)=(Y(J)-(Y1THE(J)))
420 Y2TH=TEMP2(J)-1.+(EXP(-TEMP2(J)))*((T(J)/TP2)**2.)
430 Y2THE(J)=1./(EXP(Y2TH))
440 CHI=(Y2(J)-(Y2THE(J))*.38+JJN*.01)**2.
450 CHSQ=CHI+CHSQ
460 IF(J.LE.8) GO TO 490
470 IJK=IJK+1
480 CHISQ(IJK)=CHSQ
490 CONTINUE
500 IF(JJN.EQ.1) GO TO 550
    IIN=IJK-1
510 IF(CHISQ(IIN).GT.CHISQ(IJK)) GO TO 550
IF(IJKA.LT.1) GO TO 520
515 IF(CHISQ(IJKA).GT.CHISQ(IIN)) GO TO 520
GO TO 550
520 AJJN=((JJN-1)*.01+.38)
530 AJJK=JJK+T0
540 AJJ=JJ*50.+E00
    IJKA=IIN
GO TO 560
550 CONTINUE
```

```
560 CONTINUE
570 CONTINUE
580 WRITE(5,590)AJJN,AJJK,AJJ
590 FORMAT(1H 'NORM.CONST.=' ,G, 'TP2=' ,G, ' EP2=' ,G)
670 IJKA=0
680 IJK=0
INK=0
CHSQ=0.0
690 DO 1070 JJ=1,40
700 DO 1060 JJK=1,10
710 DO 1050 JJN=1,20
600 IJ=3+INK
IF(IJ.GT.9) GO TO 780
610 X=(AJJ/R)*(1./T(IJ))
XX=(AJJ/(R*AJJK))
TEMP2(IJ)=X-XX
620 Y2TH=TEMP2(IJ)-1.+(EXP(-TEMP2(IJ)))*((T(IJ)/AJJK)**2.)
630 Y2THE(IJ)=(1./(EXP(Y2TH)))*AJJN
640 WRITE(5,650) Y2THE(IJ),T(IJ)
650 FORMAT(1H 'N/NP=' ,G, ' TEMP=' ,G)
INK=INK+1
IF(IJ.EQ.9) GO TO 780
GO TO 600
780 CHSQ=0.0
790 DO 930 J=1,6+ICOUNT
800 TP1=TP+JJK-3.
810 E12=E11-1000.+25.*JJ
820 X=E12/(R*T(J))
830 XX=(E12/(R*TP1))
840 TEMP1(J)=X-XX
850 Y1TH=TEMP1(J)-1.+(EXP(-TEMP1(J)))*((T(J)/TP)**2.)
860 Y1THE(J)=1./EXP(Y1TH)
870 Y1(J)=(Y(J)-Y2THE(J))
880 CHI=(Y1(J)-(Y1THE(J))*.82+.01*JJN)**2.
890 CHSQ=CHI+CHSQ
900 IF(J.LE.5+ICOUNT) GO TO 930
910 IJK=IJK+1
920 CHISQ(IJK)=CHSQ
930 CONTINUE
940 IF(IJK.EQ.1) GO TO 1050
950 IIN=IJK-1
960 IF(CHISQ(IIN).GT.CHISQ(IJK)) GO TO 1050
970 IF(IJKA.LT.1)GO TO 1000
980 IF(CHISQ(IJKA).GT.CHISQ(IIN)) GO TO 1000
990 GO TO 1050
1000 AJJN=(JJN-1)*.01+.82
1010 AJJK=JJK+TP-3.
1020 AJJ=JJ*25.+E11-1000.
1030 IJKA=IIN
1040 GO TO 1060
```

```
1050 CONTINUE
1060 CONTINUE
1070 CONTINUE
1080 WRITE(5,1090)AJJN,AJJK,AJJ
1090 FORMAT(1H 'NORM.CONST 1=',G,'TP=',G,' EP1=',G)
1100 DO 1180 J=1,6+ICOUNT
1110 X=(AJJ/R)*(1./T(J))
1120 XX=(AJJ/(R*AJJK))
1130 TEMP1(J)=X-XX
1140 Y1TH=TEMP1(J)-1.+(EXP(-TEMP1(J)))*((T(J)/AJJK)**2.)
1150 Y1THE(J)=(1./(EXP(Y1TH)))*AJJN
1160 WRITE(5,1170)Y1THE(J),T(J)
1170 FORMAT(1H 'N/NP1=',G,' TEMP=',G)
1180 CONTINUE
ICUUNT=ICOUNT+1
IF(ICOUNT.EQ.3) GO TO 1190
E11=AJJ
GO TO 290
1190 END
```

## APPENDIX C

## Error Analysis

The error analysis of the various experimental parameters is straightforward. In our experiments we generally want to determine the quantity  $x = f(u, v, \dots)$  by measuring  $u, v, \dots$ . Although it may not be exact, we assume that the most probable value of  $x$  is given by [45],

$$\bar{x} = f(\bar{u}, \bar{v}, \dots) \quad . \quad (C.1)$$

The uncertainty in the resultant value of  $x$  can be found by considering the spread in  $x$  resulting from combining the individual measurements  $u_i, v_i, \dots$  into individual results  $y_i$ ,

$$x_i = f(u_i, v_i, \dots) \quad . \quad (C.2)$$

The variance of  $x$ ,  $\sigma_x^2$ , is given by,

$$\sigma_x^2 = \lim_{N \rightarrow \infty} \frac{1}{N} \sum_{i=1}^N (x_i - \bar{x})^2 \quad . \quad (C.3)$$

The deviation  $x_i - \bar{x}$  can now be expressed in terms of the deviations  $u_i - \bar{u}, v_i - \bar{v}, \dots$ , or,

$$x_i - \bar{x} \approx (u_i - \bar{u}) \frac{dx}{du} + (v_i - \bar{v}) \frac{dx}{dv} + \dots \quad . \quad (C.4)$$

Combining Eqs. (C.3) and (C.4) yields

$$\begin{aligned}
\sigma_x^2 &\approx \lim_{N \rightarrow \infty} \frac{1}{N} \sum_i^N \left[ (u_i - \bar{u}) \left( \frac{dx}{du} \right) + (v_i - \bar{v}) \left( \frac{dx}{dv} \right) + \dots \right]^2 \\
&\approx \lim_{N \rightarrow \infty} \frac{1}{N} \sum_i^N \left[ (u_i - \bar{u})^2 \left( \frac{dx}{du} \right)^2 + (v_i - \bar{v})^2 \left( \frac{dx}{dv} \right)^2 \right. \\
&\quad \left. + 2(u_i - \bar{u})(v_i - \bar{v}) \left( \frac{dx}{du} \right) \left( \frac{dx}{dv} \right) + \dots \right] \quad (C.5)
\end{aligned}$$

Notice that  $\sigma_u^2 = \lim_{N \rightarrow \infty} \frac{1}{N} \sum_i^N (u_i - \bar{u})^2$  and  $\sigma_v^2 = \lim_{N \rightarrow \infty} \frac{1}{N} \sum_i^N (v_i - \bar{v})^2$ ; similarly

$\sigma_{uv}^2 = \lim_{N \rightarrow \infty} \frac{1}{N} \sum_i^N [(u_i - \bar{u})(v_i - \bar{v})]$ . Equation (C.5) can now be written as

$$\sigma_x^2 \approx \sigma_u^2 \left( \frac{dx}{du} \right)^2 + \sigma_v^2 \left( \frac{dx}{dv} \right)^2 + 2\sigma_{uv}^2 \left( \frac{dx}{du} \right) \left( \frac{dx}{dv} \right) + \dots \quad (C.6)$$

If the fluctuations of  $u$ ,  $v$ , ... are uncorrelated, Eq. (C.6) reduces to

$$\sigma_x^2 \approx \sigma_u^2 \left( \frac{dx}{du} \right)^2 + \sigma_v^2 \left( \frac{dx}{dv} \right)^2 + \dots, \quad (C.7)$$

or written more generally,

$$\sigma_{a_j}^2 = \sum_i \left[ \sigma_i^2 \left( \frac{da_j}{dy_i} \right)^2 \right] \quad (C.8)$$

In order to be able to use Eq. (C.8) to estimate the standard deviations of the diffusion and desorption parameters, we need to know the variance of each measurement  $\sigma_i^2$ . When using Auger spectroscopy to study the diffusion and desorption of nitrogen,  $\sigma_i^2$  is the variance of the nitrogen Auger peak.

The value of  $\sigma_i$  is determined by first depositing a predetermined amount of electron dissociated nitrogen on the surface. A number of Auger scans are then taken in the region of nitrogen  $KL_{2,3}L_{2,3}$  transition. From the variation in the peak to peak height of the nitrogen Auger transition, a value of  $\sigma_i$  is obtained. We found that  $\sigma_i^2$  can be described by  $\sigma_i^2 = -7.39 \times 10^{-2} \text{ PPO}(\text{IK}) + 9.957 \times 10^{-2}$  where  $\text{PPO}(\text{IK})$  is the peak to peak height of the normalized nitrogen Auger transition.

As an example, consider the estimation of the standard deviation of the diffusion coefficient  $D$  of the electron dissociated nitrogen after heating for 3500 seconds at  $800^\circ\text{K}$ . The computer program `LDIF.F4` is run with the appropriate values of `XX1` (position) and `PPO` (Auger peak height). A value of  $D = 7.55 \times 10^{-8} \text{ cm}^2/\text{sec}$  is obtained. One of the values of `PPO` is now changed by a small amount ( $\sim 1\%$ ) and another value of  $D$  is calculated. This procedure is repeated for all the data points. We now have values of  $\frac{dD_i}{d(\text{PPO})_i}$ , and Eq. (C.8) becomes

$$\sigma_D^2 = \sum_i \sigma_i^2 \frac{dD}{d(\text{PPO})_i},$$

from which the standard deviation of  $D$  can be obtained.

Once the values of  $\sigma_{D_j}^2$  are obtained for various temperatures they are plotted as  $\ln(D)$  vs.  $1/T$  using the program `LEASTB.BAS`. This program computes the best least squares fit to the data with a weighting function  $w_i$  given by [46],

$$w_i = \frac{D^2}{\sigma_D^2}. \quad (\text{C.9})$$

An identical procedure is followed for the calculation of the errors associated with the desorption parameters.

## REFERENCES

1. R. Gomer, R. Wortman and R. Lundy, *J. Chem. Phys.* 26, 1147 (1957)
2. R. Wortman, R. Gomer and R. Lundy, *J. Chem. Phys.* 27, 1099 (1957)
3. R. Gomer, Field Emission and Field Ionization (Harvard University Press, Cambridge, 1961) p. 113
4. G. Ehrlich and F. G. Hudda, *J. Chem. Phys.* 36, 3233 (1962)
5. R. Butz and H. Wagner, *Surf. Sci.* 63, 448 (1977)
6. M. G. Wells and D. A. King, *J. Phys. C:Solid State Phys.* 7, 4053 (1974)
7. A. P. Janssen, *Surf. Sci.* 52, 230 (1975)
8. G. Ehrlich, *J. Chem. Phys.* 34, 29 (1961)
9. D. L. Adams and L. H. Germer, *Surf. Sci.* 27, 21 (1971)
10. G. Ehrlich, *J. Chem. Phys.* 36, 1171 (1962)
11. B. D. Braford and R. R. Rye, *J. Chem. Phys.* 60, 1046 (1974)
12. L. J. Rigby, *Can. J. Phys.* 43, 1020 (1965)
13. P. W. Tamm and L. D. Schmidt, *Surf. Sci.* 26, 286 (1971)
14. T. A. Delchar and G. Ehrlich, *J. Chem. Phys.* 42, 2686 (1964)
15. R. M. Stern, abstract, Division of Colloid and Surface Chemistry, in the 150th meeting Am. Chem. Soc. (Atlantic City, New Jersey, 1965)
16. G. J. Dooley III and T. W. Haas, *J. Vac. Sci. Technol.* 7S, 90 (1970)
17. R. Liu, Ph.D. thesis
18. G. Ehrlich, *Advan. Catalysis* 14, 255 (1963)
19. D. R. Sandstrom and S. P. Withrow, *J. Vac. Sci. Technol.* 14, 748 (1977)
20. C. C. Chang, *Surf. Sci.* 25, 53 (1971)
21. L. A. Harris, *J. Appl. Phys.* 39, 1428 (1968)

22. J. C. Tracy in Electron Emission Spectroscopy edited by W. Dekeyser et.al. (D. Reidel Publishing Co., Dordrecht, Holland, 1973) p. 295
23. L. A. Harris, J. Appl. Phys. 39, 1419 (1968)
24. N. J. Taylor, Rev. Sci. Instr. 40, 792 (1969)
25. K. R. Spangenberg, Vacuum Tubes (McGraw Hill Co., New York, 1948) p. 298
26. R. D. Heidenreich, Fundamentals of Transmission Electron Microscopy (John Wiley and Sons Inc., New York 1964) p. 104
27. G. Ertl and J. Koppers, Surf. Sci. 21, 64 (1970)
28. P. J. Estrup and E. G. McRay, Surf. Sci. 25, 1 (1971)
29. W. P. Ellis and R. L. Schwoebel, Surf. Sci. 11, 82 (1968)
30. M. Henzler, Surf. Sci. 19, 159 (1970)
31. R. V. Culver and F. C. Tompkins, Advan. Catalysis, 11, 68 (1959)
32. A. G. Knapp, Surf. Sci. 34, 289 (1973)
33. I. Langmuir and K. H. Kingdon, Phys. Rev. 34, 129 (1929)
34. H. Skelton, Phys. Rev. 107, 1553 (1957)
35. P. A. Redhead, Vacuum 12, 203 (1962)
36. G. Ehrlich, J. Appl. Phys. 32, 4 (1961)
37. J. T. Yates, R. Klein, T. E. Madey, Surf. Sci. 58, 469 (1976)
38. J. T. Yates and T. E. Madey, The Structure and Chemistry of Solid Surfaces, Ed. G. A. Somorjai (Wiley, New York, 1969) p. 59-1
39. H. F. Winters and D. E. Horne, Surf. Sci. 24, 587 (1971)
40. W. Plummer, J. W. Gadzuk and R. D. Young, Solid State Commun. 1, 487 (1969)
41. W. Ermrich, Nuovo Cimento Suppl. [1] 5, 582 (1967)
42. A. A. Frost and R. G. Pearson, Kinetics and Mechanism (John Wiley and Sons Inc., New York, 1953) p. 40

43. J. Crank, The Mathematics of Diffusion (Clarendon Press, Oxford 1956)
44. D. A. Reed and G. Ehrlich, J. Chem. Phys. 64, 4616 (1976)
45. P. R. Bevington, Data Reduction and Error Analysis for the Physical Sciences (McGraw-Hill, New York 1969) p. 154
46. M. Vesely, Computer Curve Fitting of Polynomials, Coordinated Science Laboratory Report R-595, University of Illinois (1972)

## VITA

Anthony Polak was born in Czechoslovakia on October 25, 1948. He graduated from Herricks High School in New Hyde Park, New York in June, 1966. He then attended Stevens Institute of Technology, majoring in physics. In June, 1970 he received a Bachelor of Science degree with high honors. In June, 1970 he began graduate work in the Department of Metallurgy, at the University of Illinois, as an Allied Chemical Fellowship recipient. The following year after completing the M.S. Degree in Metallurgy, he began work under Professor Gert Ehrlich. He is the author of one publication,

"Surface Diffusion of Gas Chemisorbed on a Single Crystal Plane:  
N on W(110)," A. Polak and G. Ehrlich, J. Vac. Sci. Technol.,  
14, 407 (1977)